A NOVEL PNEUMATIC STEPPING MOTOR

Atef E. F. Fahim

A THESIS

in the

FACULTY OF ENGINEERING

Presented in Partial Fulfillment of the
Requirement for the Degree of
Master of Engineering at
Concordia University
Montreal, Quebec, Canada

June, 1977

ABSTRACT

A NOVEL PNEUMATIC STEPPING MOTOR

Atef E. F. Fahim

A novel pneumatic stepping motor is presented in this thesis. The concept of operation, and the different possible variations in its construction are discussed. A detailed study of the pertinent geometric parameters of the motor together with the effect of these parameters on the performance characteristics is conducted. Static and dynamic analyses of a prototype motor system are presented. The results of the theoretical analysis are compared with experimental data obtained from the prototype system. In view of the good correlation between the theoretical and experimental results, the dynamic model derived in the thesis adequately describes the prototype system behaviour.

A simple graphical design procedure, based on the analysis of the prototype system, is also given.

ACKNOWLEDGEMENT

The author acknowledges the guidance of his supervisor Dr. R.M.H. Cheng. The helpful suggestions of Mr. N. Suresh are acknowledged. The assistance of Mr. J. Elliott during the experimental stage is appreciated. Special thanks, for the typing work involved, are due to Miss L. Mikhail.

The facilities provided by the Fluid Control Centre of Concordia University to carry out this work are also acknowledged.

This project was sponsored by the National Research Council of Canada under Negotiated Grant D-30.

TABLE OF CONTENTS

LIST OF FIGURES

LIST OF TABLES

NOMENCLATURE

α	step angle
α_s	driving profile angle ($\alpha_s = \alpha + \varepsilon$)
$\beta_1, \beta_2, \beta_3$	dimensional constants
ε	offset angle
ε_m	minimum offset angle
η	backlash angle
θ	angular displacement ($\theta = \theta_1$)
$\theta_1, \theta_2, \theta_3, \theta_4$	displacement angles of the motor, the beginning and end of the torque transducer shaft, and the load respectively
λ	angle of the straight line part of the profile
Λ_1 through Λ_{21}	nondimensional constants
μ_1	coefficient of friction between cam and actuator
μ_2	coefficient of friction between actuator and guide
μ_3	output shaft seal friction
μ_4	load friction
ξ	complementary angle of the angle of attack
Ξ	stall torque function
Σ	torque-pressure ratio
τ	nondimensional time
τ_f	upper limit on integration

τ_V	opening time of value
ϕ	angle of attack
ϕ_0	initial angle of attack
ψ_1	friction angle between actuator and cam
Ω_L	natural frequency of load
Ω_M	natural frequency of motor
a_V	instantaneous valve equivalent area
A_C, A_D, A_L, A_V	areas of cylinder, entrance to cylinder, connector, and maximum equivalent area of valve respectively.
A_{CL}	maximum area of cylinder to be housed in a cam
c_C, c_J, c_L	loss factors at, entrance to cylinder, entrance to rotary junction, and line respectively
C_C, C_J, C_L, C_V	capacitances of volumes of cylinder, rotary junction, connector and valve respectively
f_{CS}, f_{CD}	constant force accounting for the piston seal friction and the constant part of the return spring force, at beginning of motion, and while moving
F	net force acting on the piston
F_B	force on friction brake
F_S	force on piston corresponding to supply pressure.

H	piston height plus half the separator plate thickness
J_L, J_M	inertias of load, and motor respectively
k	ratio of specific heats of a perfect gas
K, K_1, K_2	friction brake factors
K_E	torsional stiffness of the load and torque transducer combined
K_L, K_M, K_T	torsional stiffnesses of the load, the motor and the torque transducer shafts respectively
K_S	cylinder return spring constant
m_C, m_J, m_L, m_V	mass of air occupying the cylinder, the rotary junction, the connector and the valve volume respectively
N_t	number of teeth on the motor cam
P_a, P_b, P_c, P_d	instantaneous pressures at junctions a, b, c, and d respectively
P_{ij}	pressure ratio between the two junctions i and j ($P_{ij} = P_i/P_j$) where i and j are general for s, a, b, c and d
P_C	instantaneous gage pressure inside the cylinder
P_s	supply pressure
P_{atm}	atmospheric pressure
r	instantaneous radius of cam profile

R	universal gas constant
R_a	addendum radius of the cam
R_d	dedendum radius of the cam
R_t	actuator tip radius
R_{ad}	cam tooth depth
R_{GL}	largest radius of a cylinder that can be housed in a cam
R_C, R_J, R_L, R_V	resistances of the cylinder entrance, the rotary junction entrance, the connector and the valve respectively
S	actuator (piston rod) guide height
t	time
t_a, t_b, t_c, t_d	instantaneous temperatures at junctions a, b, c, and d respectively
t_{ij}	temperature ratio between the two junctions i and j ($t_{ij} = t_i/t_j$) where i and j are general for s, a, b, c and d
t_s	supply temperature
T_M	static torque developed by the motor
T_T	torque measured by the torque transducer
T_{FB}	friction torque of the brake
T_{FM}	friction torque of the motor output shaft seals
T_{st}	stall torque of the motor
$T_{st(0)}$	stall torque of the motor at the beginning of the step

V_V, V_L, V_J	volumes of the valve, the connector, and the rotary junction, respectively
$V_{C(0)}$	cylinder dead volume
V_t	total volume of the pneumatic system at beginning of step ($V_T=V_V+V_L+V_J+V_{C(0)}$)
W_{ij}	air mass flow rate between the two junctions i and j where i and j are general for o, s, a, b, c, and d
$W_{(sa)max}$	maximum air flow rate through the valve at the maximum equivalent area
x	piston displacement

Throughout this thesis, asterisked symbols indicate nondimensionalized quantities.

CHAPTER I

INTRODUCTION

In the field of automation and control, stepping motors are widely used for the purpose of indexing or positioning. A stepping motor may be described as a stepwise rotational prime-mover which is actuated by means of a digital or pulse input signal. In other words, the output shaft of a stepping motor undergoes a rotational displacement through a fixed angle, for each input pulse fed into it.

Although the operations performed by stepping motors can also be achieved by using analog systems consisting of continuous-running motors with feedback regulation for the "start-stop" action, the use of stepping motors does prove to be advantageous in many applications. A general comparison of the characteristics of the above two basic systems, which can be used for indexing or positioning, is given in Table I.1. The only outstanding advantage of the analog system lies in its very wide frequency response range. However, in applications where such a feature is not required, the stepping-motor systems provide a better solution mainly due to their lower quiescent power drain and due to their inherent stability within the design load conditions. Furthermore, with the increasing use of digital control systems in automation, the stepping motor offers the possibility of eliminating or minimizing the digital

to analog interface circuitry which would be required in the analog systems.

As a result of these advantages, stepping motor drives are replacing analog or continuous rotation drives on an increasing scale in most indexing and/or positioning operations.

Stepping motors may be classified into electrical or fluid operated categories according to the nature of the basic actuating force. In either case, mechanical motion through shafts, linkages and similar mechanical members is essentially involved.

Commercially available stepping motors are mostly electrical. These may be further subdivided into two broad classes: electric stepping motors and electrohydraulic stepping motors. The former category in which the actuating electromagnetic force directly creates shaft rotation, is mainly used in high-speed low-torque applications. For example, "Slo-Syn M Series stepping motors" have the torque speed characteristic shown in Fig. I.1, with a maximum speed of 20,000 steps per second and a very low torque, and a torque of the order of 25 oz-in at low speeds [1].

For high torque, low-to-medium speed requirements, electrohydraulic stepping motors are used, wherein the output torque of the basic electric stepping motor is amplified using a hydraulic amplification system. Figure I.2

TABLE I.1. COMPARISON BETWEEN STEPPING MOTOR AND ANALOG FEEDBACK SYSTEMS

CHARACTERISTICS	ANALOG FEEDBACK SYSTEMS	STEPPING MOTOR SYSTEM
Nature of device	Analog voltage input (other inputs through D/A convertors), rate output	Pulse rate input, involving uniform or random pulses (analog signals through A/D convertors), stepping rate output
Operational effect	Integration	Finite summation
Angle or distance of output member travel	Proportional to time integral of analog input	Exactly determined by number of input pulses
Velocity and positional feedback	Essential	Not required - may be used for self-stepping or hold-gating
Linearity	Linearity dependent on feedback	Stepping linearity does not require feedback
Stability (as position servo)	With position feedback loop, depends on rate damping (non dissipative), dissipative damping, and/or load networks	Not ordinarily a problem when operated open-cycle as a position control; when operated closed-cycle, stability is a function of step-to-signal frequency ratio
Error	With position feedback loop, depends on feedback transducer resolution and linearity, noise, stability, etc	Depends on accuracy of individual stepping mechanism within limits of designed stepping rate
Resolution	Governed mainly by feedback transducer resolution assuming high loop gain	Depends on built-in step size
Frequency response	Zero to high frequency response	Relatively low frequency response
Torque	Requires torque multiplication through reduction gear train almost universally	Directly available at output shaft of stepping device in most cases
Digital programming capability	May be adapted with D/A input device and data encoder on output shaft	Can be commanded directly by digital controller
Two-mode operation (slewing or inching)	Readily adapted	Readily adapted - many steppers will slew as well as step

shows torque speed characteristics of three of these motors. The curve for the Fujitsu motor operating at 1000 psi shows that the motor can attain a maximum speed of 3200 rpm with a torque output of 60 lb-in, and has a maximum torque of 205 lb-in at low speeds [2].

Electrohydraulic stepping motors can be used for high torque, low speed requirements which arise in many industrial automation situations such as indexing tables. However, mainly because of the hydraulic components and the power pack required, the cost involved in such a system would be essentially high.

A survey of alternative stepping motor drives was indicative that the above requirements of high torque and low speed could be met by a pneumatic drive. Several of such drives have been developed over the last few years, the more significant of which will be discussed later. In this thesis, the design of a pneumatic stepping motor in which a moderately high torque, low speed output can be achieved at a reasonable cost will be presented. The design also provides very high positional accuracy due to the use of a detent action in the motor mechanism.

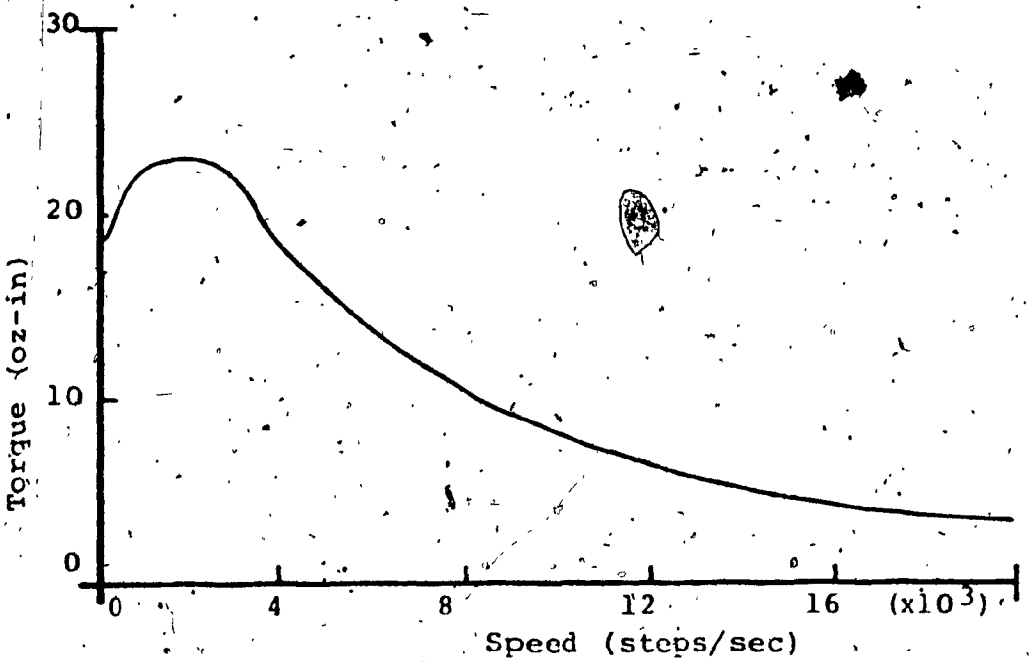

Fig. I.1: Typical Characteristics of Electric Stepping Motors (Slo-Syn M Series).

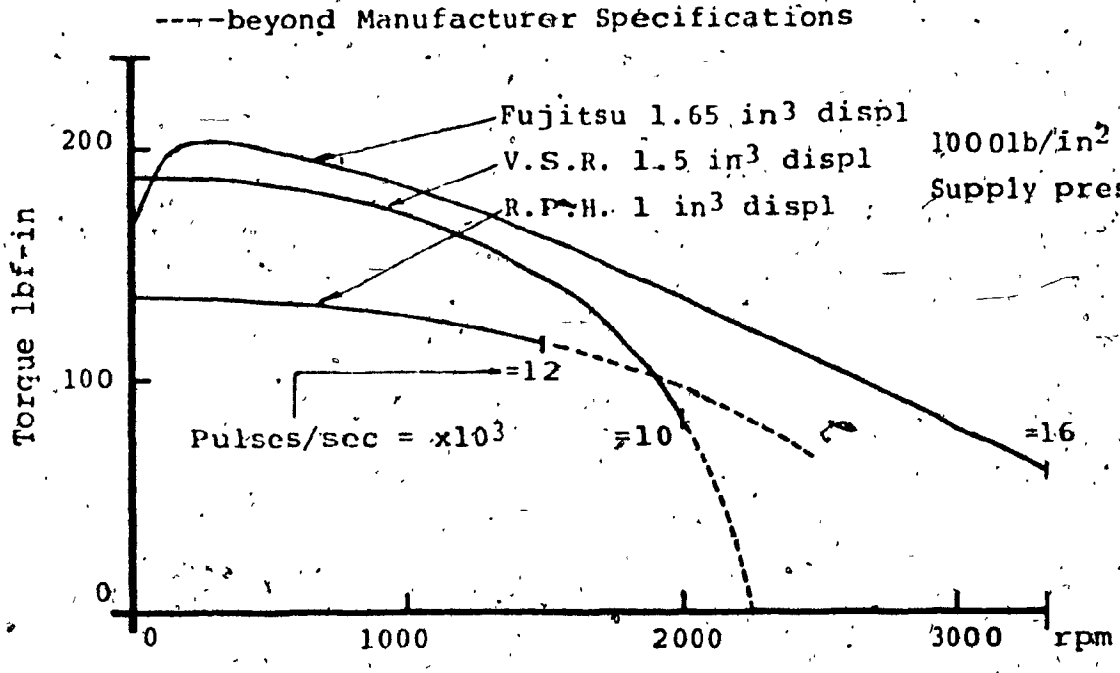

Fig. I.2: Typical Characteristics of Three Electrohydraulic Stepping Motors.

CHAPTER II

SURVEY

Although pneumatic stepping motors are not yet available as commercial units, a number of experimental prototypes have been built. The results of a literature survey on such motors are given in Table II.1, together with the relevant reference sources. Two of the motors in the above table, namely the "Howland's Motor" [4] and the "Carlnas's Rotellmotor" [10], have performance characteristics close to those of the motor described in the present work. A schematic diagram of "Howland's Motor" [4] is shown in Fig. II.1. The motor consists of two gears: a gimbal supported driving gear, carrying 181 teeth, which is free to nutate but not to rotate, and an output gear having 180 teeth which is free to rotate but not to nutate. By unequal pressurization of eight bellows attached to its periphery, the driving gear is made to tilt and contact the output gear. By a sequential pressurization of the eight bellows, the contacting point between the gears travels around the circumference of the output gear. Thus, for every complete revolution of the driving gear, the output gear advances by 2°. It follows that since eight bellows are used, the output shaft can be indexed by increments of 0.25°.

Carlnas's Rotellmotor operates on a somewhat similar principle to Howland's Motor. In his motor, Carlnas

TABLE II.1. A SUMMARY OF THE MORE SIGNIFICANT DEVELOPMENTS IN PNEUMATIC STEPPING MOTORS

Reference	Operational Concept	Performance				Remarks
		Operating pressure psig	Stall Torque lbf-in	Maximum Speed step/sec	Resolution	
Martin[3]	Ratchet & pawl with detent wheel	11	12	35	1°	Design not compact due to mechanism used.
Howland [4] Griffin and Cooley [5]	Gimbal-supported nutating driving gear of 181 teeth in mesh with an output gear of 180 teeth, actuated by 8 bellows driven by fluidic logic	70	70	173	0.25°	complex design due to large number of actuators, requires highly complex fluidic logic circuits to drive the motor
Nomoto and Shimada [6]	Utilizing impact force of an air jet	-	-	-	-	no data available
	Utilizing the reaction to an air jet	20	0.134	10	20°	very low available torque
Blaiklock[7]	Improvements on Howland's motor	2	-	40	2.4°	complex design due to use of more bearings than the Howland's motor.
Hunter and Thompson[8]	Symmetrical cam with 3 sets of actuators	-	-	-	-	no data available
Warren [9]	Driven by jet acting on a pelton wheel-like rotor, and likewise stopped by another jet	-	-	-	-	no data available
Carlnas[10]	Flexible spline as stator actuated by 8 bags in mesh with a rigid gear having more teeth than the flexible spline	73	26.7	250	0.278°	delicate design requires highly complex fluidic logic circuits to drive the motor

TABLE II.1. A SUMMARY OF THE MORE SIGNIFICANT DEVELOPMENTS IN PNEUMATIC STEEPING MOTORS (CONTINUED)

Reference	Operational Concept	Performance				Remarks
		Operating pressure psig	Stall Torque lbf-in	Maximum Speed step/sec	Résolu-tion	
Dat, Fabre and Yalcin [11]	Wankel engine-line arrangement with special porting.	14.5	$1x10^{-4}$	10	180°	poor performance characteristics, and poor resolution accuracy
	Eccentric rotor with vanes forming two chambers operates on pressure differential across chambers	-	-	-	-	no data available
Cheng and Fahim [12] & [13]	Asymmetric internal gear like cam with two collinear actuators	100	50	21	12°	simple design, simple control circuits, high torque and good accuracy

utilizes a driving flexible spline, actuated by eight elastic bags as shown in Fig. II.2, which meshes with an output rigid spline. The flexible spline is prevented from rotation and when the elastic bags are depressurized, the spline has a circular shape with a diameter slightly less than that of the rigid spline. By an appropriate pressurization of diametrically opposed bags, the flexible spline is forced to assume an elliptic shape which makes contact with the rigid spline as shown in Fig. II.2. By proper sequencing of the pressure signals, the point of contact between the two splines travels around the periphery. Since only the rigid spline is allowed to rotate, and since it has 162 teeth as compared to 160 on the flexible spline, it follows that for composite sequencing of the pressure signal (more than one pair of diametrically opposed bags pressurized at the same time) the rigid spline can be indexed in increments of 0.278°.

Both the "Howland's" and the "Carlnas's" motors are built along the lines of electric stepping motors with actuators (i.e. 'poles') located along the periphery of the stator. In such a case, the finer the resolution required, the larger would be the number of actuators, thereby resulting in a highly complicated design. Furthermore, this would require highly sophisticated control circuitry for obtaining the desired energizing sequence.

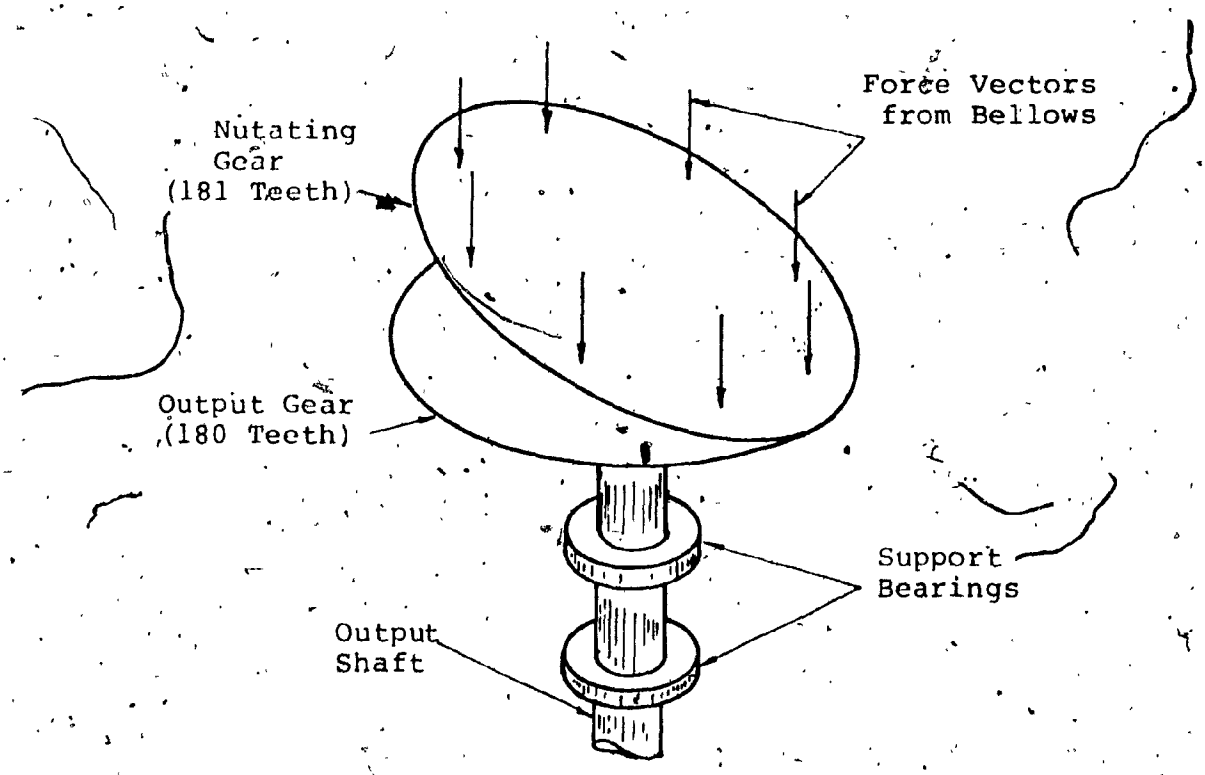

Fig. II.1: Schematic Diagram of Howland's Motor [4].

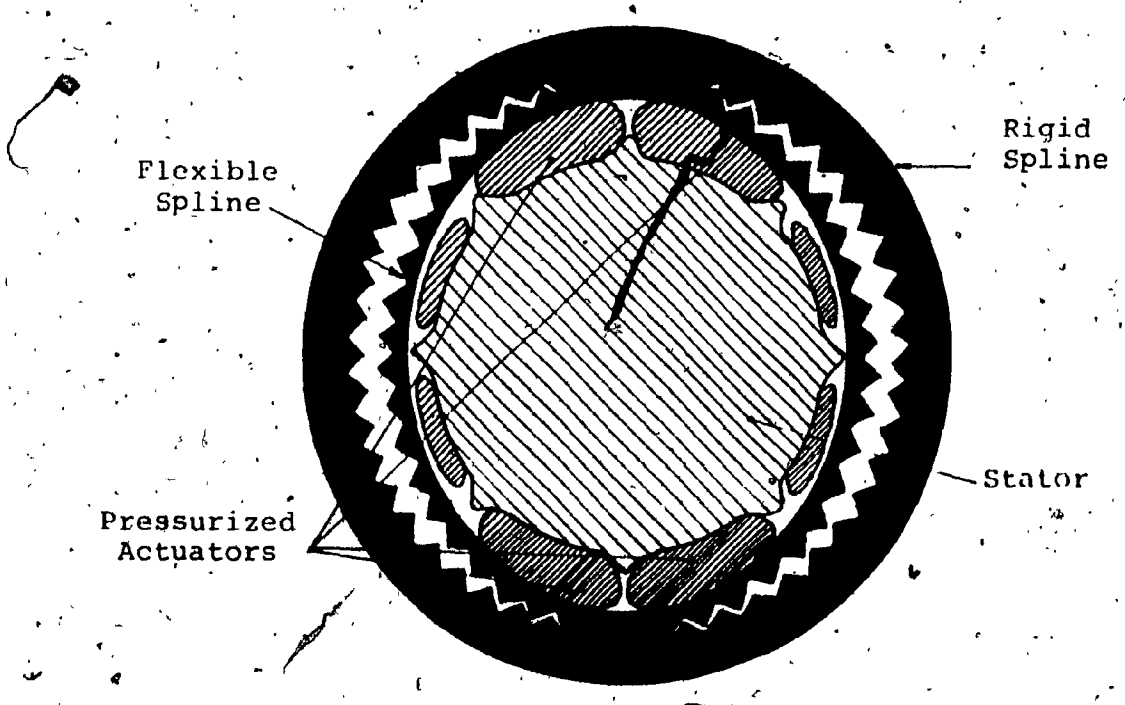

Fig. II.2: Schematic Diagram of Carlnas's Rotellmotor [10].

In the proposed approach however, only two single acting actuators (or one double acting equivalent) are used, thus resulting in a simple design of the motor and associated circuitry. The required resolution can be selected by appropriate cam design.

CHAPTER III

CONCEPT AND CONSTRUCTION OF THE PROPOSED STEPPING MOTOR

III.1 Principle of Operation

The concept which underlies the operation of the proposed stepping motor makes use of a cam and actuator arrangement. The cam is similar to an internal gear, with alternately placed "driving profiles" and "idle faces" of specific geometrical shapes forming the flanks of the teeth. The actuator is the piston rod end of a pneumatic cylinder.

Figure III.1 shows the cam and actuator arrangement schematically. A double-acting diaphragm cylinder (C) with a through-piston rod (B) is housed in the central space provided by the cam (A). The cylinder housing remains fixed while the cam is allowed to rotate. The design of the cam, as shown in Fig. III.1, is such that the trailing extremity (a) of a driving profile (ab) is diametrically opposite to the leading extremity (c) of another driving profile (cd), plus an offset (ε). Referring to Fig. III.1 again, when air pressure is applied to cylinder (C) to force the piston rod (B) to travel downwards, the end of the rod engages with the driving profile (cd) causing relative rotation between the cylinder and the cam. As the cylinder is fixed, the cam will be forced to rotate in a clockwise direction. Once the lower point (d) is reached by the rod end, the cam is locked

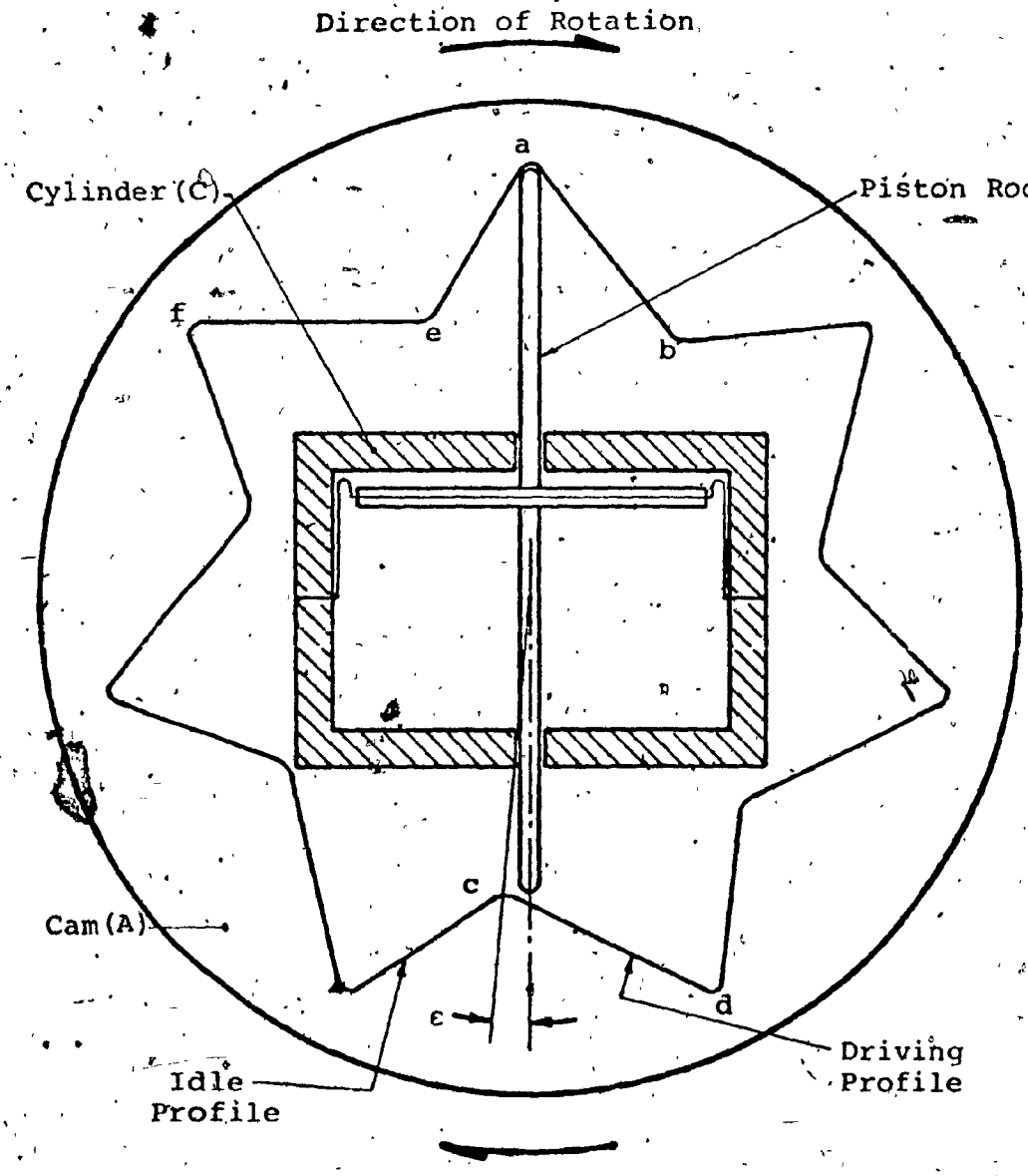

Fig. III.1: Schematic Diagram of the Cam and Actuator Arrangement.

firmly in position as long as the pressure in the upper chamber of the cylinder is maintained. Similarly, upon reversal of the stroke of the cylinder, the driving profile (ef) adjacent to profile (ab) is engaged by the rod, thereby causing cam rotation in the clockwise direction again.

The design of the cam as shown in Fig. III.1 is asymmetric (i.e. having an odd number of teeth such that any given tooth peak is diametrically opposed to a valley) with an offset to the left, which results in a clockwise direction of rotation. However, a counter-clockwise rotation can be achieved by a mirror image of this cam design.

III.2 Different Possible Configurations

The schematic arrangement of the cam and actuator shown in Fig. III.1, and described in the previous section, is one out of the four possible operational configurations given in Table III.1. The discussed configuration, designated as configuration [A] in Table III.1, has been chosen to illustrate the principle of operation because of its simplicity. Referring to Table III.1, configuration [B] differs from configuration [A] in that the former employs two single-acting spring return cylinders, instead of one double-acting cylinder. Configurations [A] and [B] become equivalent to configurations [C] and [D] respectively, if the cam is fixed while the cylinder housing is allowed to rotate.

In general, a fixed cylinder-rotating cam configuration

results in a higher inertia motor, due to the flywheel effect of the cam disc and its mounting. Two different designs are possible for each of the two such configurations given in Table III.1. The first design, shown in Fig. III.2, results in a high inertia motor having a cumbersomely large rotating housing (A), and requiring additional gearing (B) in order to provide an output. The second design, consisting of the housing cantilevered on a one-sided bearing arrangement (Fig. III.3), results in a relatively lower inertia motor in which output gearing is not needed. However, in the latter design, the possibility of alignment problems is increased. Furthermore, since only a single bearing point is used, a specially designed high-stress bearing will be required.

TABLE III.1. DIFFERENT MOTOR CONFIGURATIONS

Configuration	Cylinder	Cam	No. of Cylinders and Type
[A]	Fixed	Free to rotate	1 double-acting cylinder
[B]	Fixed	Free to rotate	2 single-acting spring return cylinders
[C]	Free to rotate	Fixed	1 double-acting cylinder
[D]	Free to rotate	Fixed	2 single-acting spring return cylinders

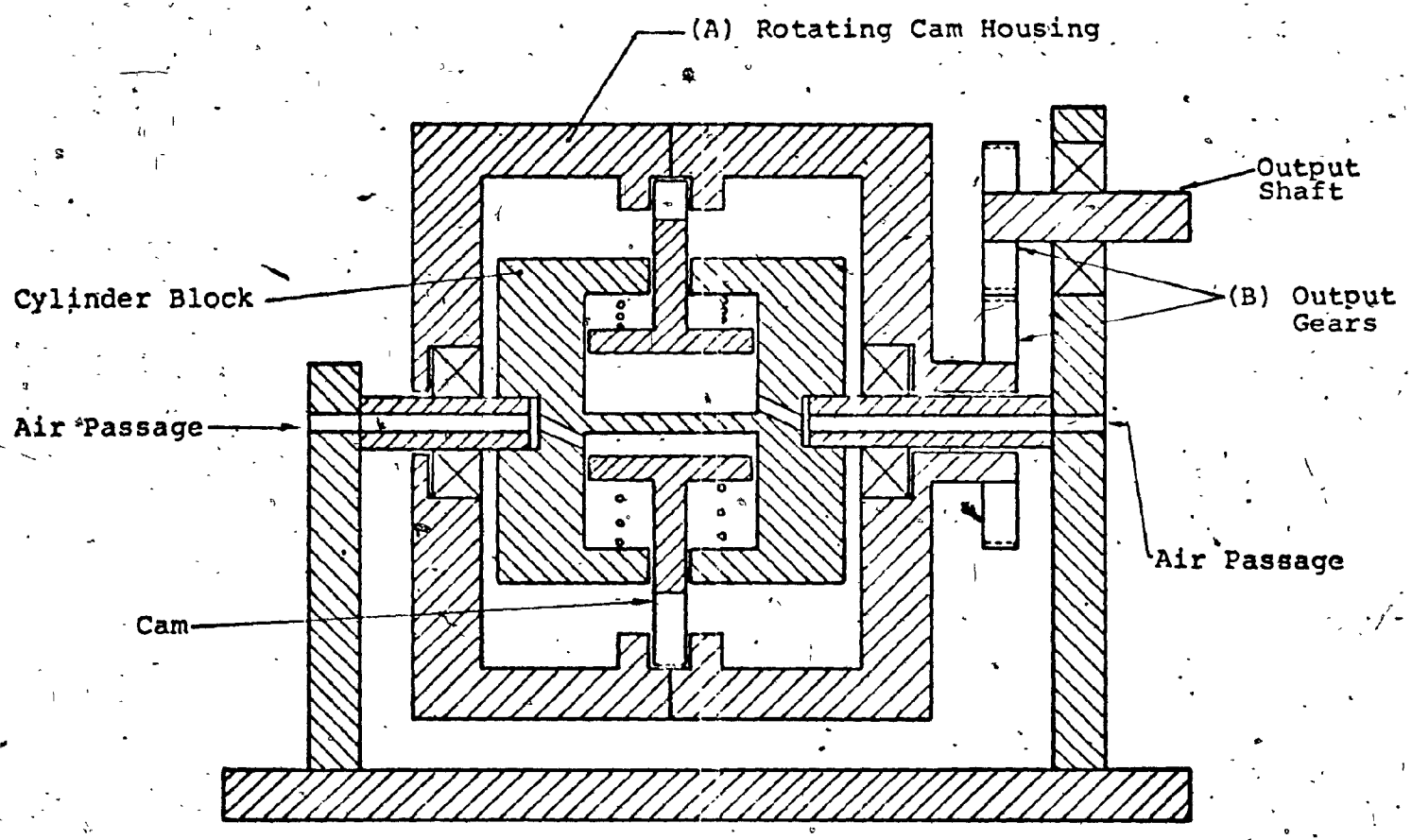

Fig. III.2: Schematic of Motor Design Configuration [B] with Full Rotary Housing.

Alternatively, a very low inertia motor can be obtained using a fixed-cam rotating-cylinder configuration. The disadvantage of this design lies in the complex inlet and exhaust pressure porting arrangements required. The inlet and exhaust ports have to be incoporated within the rotating output shaft, thereby necessitating some kind of rotary seals. For a given motor size, a relatively higher output torque can be obtained by the use of a single, double-acting cylinder rather than two single-acting, spring-return cylinders, mainly due to the reduced height of the total piston arrangement. However, a number of constraints on the output waveform of the motor and on the cam design are introduced by the use of a double-acting cylinder arrangement. The output waveform of the motor would have a rigid format due to the fact that one step cannot be started before the previous one has ended, and a certain period of time has elapsed. This time period allows for the exhaust of the chamber that was previously in operation. Furthermore, a requirement that the idle face of the cam must have a particular profile dependent upon the corresponding driving profile, is introduced due to the fact that the through-piston rod length is constant and that one end of the piston rod must clear an idle face while the other end is being engaged with the driving profile.

The above two constraints, which are undesirable from the point of view of operational flexibility and ease of

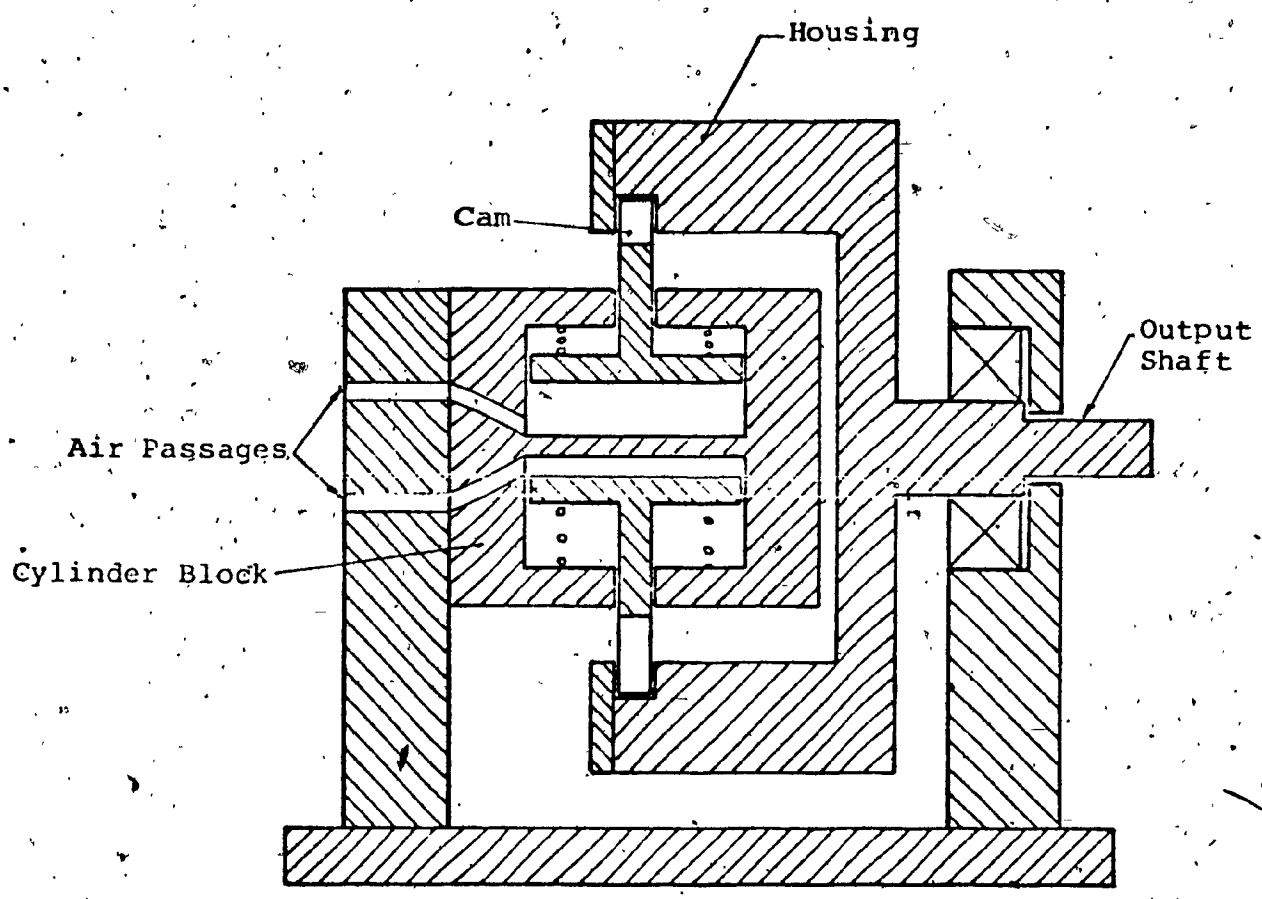

Fig. III.3: Schematic of Motor Configuration [B] with Cantilevered Housing.

manufacturing, respectively, can both be eliminated by the use of two single-acting, spring-return cylinders. Though such an arrangement would result in a lower torque output for a given cam size, it would permit the shaping of the output torque waveform by input pressure control. In this arrangement, a simple idle face profile for the cam is sufficient, thereby simplifying production.

III.3 Description of the Prototype Motor

The prototype motor was constructed according to configuration [D]. The low motor inertia and the simple design and machinability of the cam, resulting from the use of this configuration, dominated over the attendant disadvantage of the need for complex pressure porting.

An assembly drawing of the prototype is shown in Fig. III.4. As shown in the figure, the cylinder housing is comprised of two similar halves, each half carrying a part of the output shaft as well as containing a cylinder bored within. Upon assembly, the two cylinders are axially aligned together with their axis perpendicular to the axis of the output shaft. The cylinders are sealed from each other by a separating plate carrying a nylon gasket on each side. To simplify the porting design, single-acting, spring return type cylinders were chosen, thereby requiring only one port per cylinder. The porting to each cylinder is provided within the cylinder housing itself, and passes through the interior

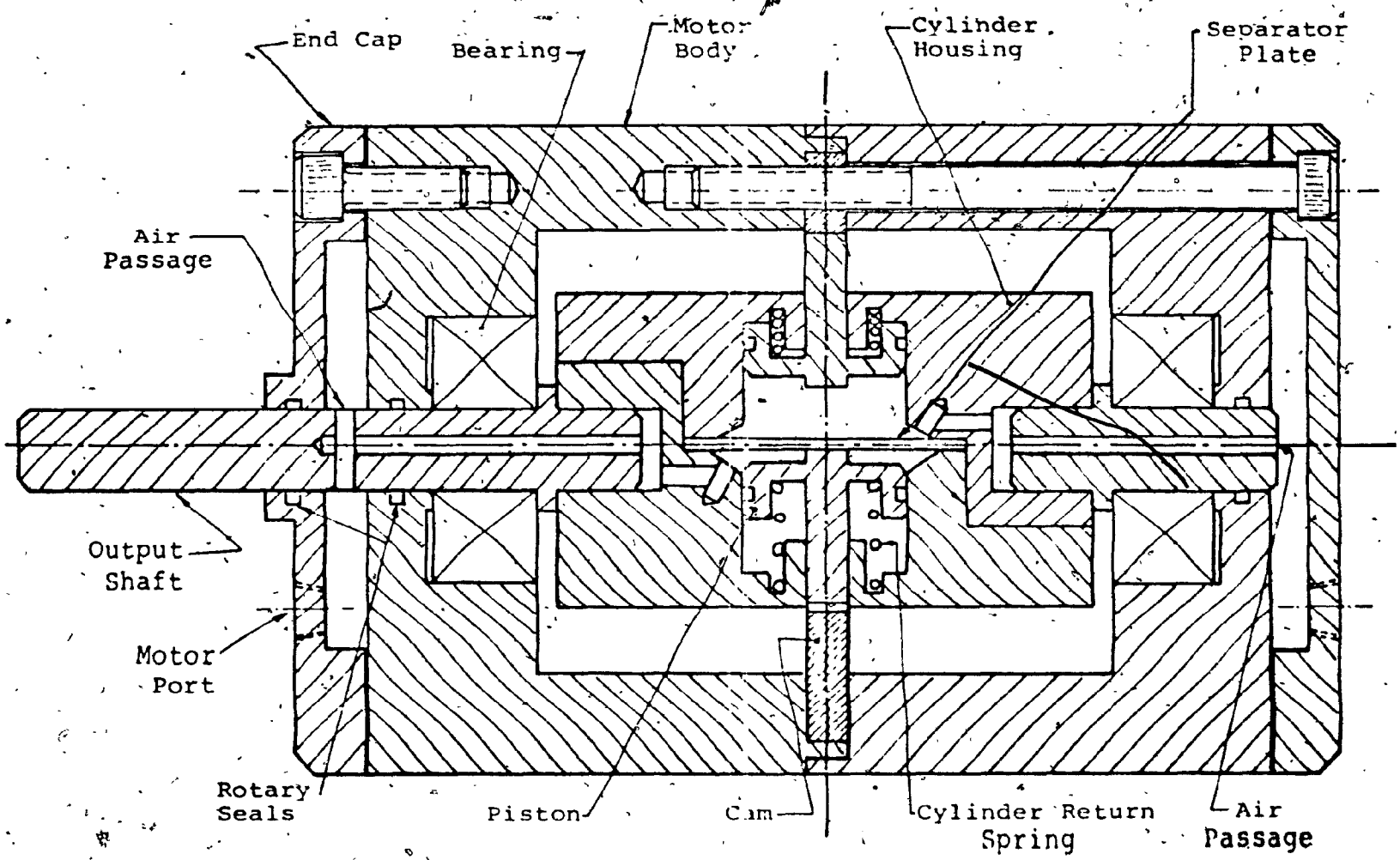

Fig. III.4: Assembly Drawing of the Prototype Motor.

of the output shaft, as shown in Fig. III.4., Ordinary steel was chosen as material for both the cylinder housing and the output shaft.

The piston and piston rod form an integrated component, machined from high carbon tool steel, with the piston carrying a groove to accommodate an O-ring seal. The cylinder housing and shaft assembly are carried on two bearings mounted in the motor body as shown in Fig. III.4.

The necessary rotary pressure connection is created by (a) the two chambers formed between the end caps and the motor body, (b) the associated O-rings, and (c) the path drilled within the output shaft.

Straight line profiles were used for the "driving profiles" and "idle faces" of the cam, for the sake of simplicity in machining. High carbon tool steel was used for the cam.

The motor body also consists of two similar machined aluminum parts, which mate together through a centering tongue and groove arrangement, thereby clamping the cam in between.

The complete set of design drawings and photographs of the components are given in Appendix A.

III.4 Description of the System Used in the Analysis

The main features of the motor described in this work are: (a) high torque, low speed; (b) very high accuracy of resolution; and (c) positive locking of the output shaft after each step. These features render the motor useful in precision positioning where high speeds are not required (e.g. indexing) and in metering applications (e.g. driving peristatic pumps) where high resolution accuracy is a prime feature [see Appendix I]. Thus the nature of the loads most likely to be driven by such a motor can be inertial (e.g. indexing discs or tables), resistive (e.g. peristatic pumps) or a combination of both.

The prototype system used in the analysis is built such that the inertia and friction of the load on the motor can be varied to simulate different loading conditions.

Figures III.5a and III.5b show the schematic diagram and a photograph respectively of the test system. The system is composed of five main units: a signal generator (A), the control valves (B), the motor (C), a torque transducer (D), and the loading arrangement (E).

The signal generator consists of a variable frequency fluidic oscillator which produces two complementary square wave signal outputs.

Since wall-attachment type fluidic logic is used in the signal generator, the output pressure level is too low for

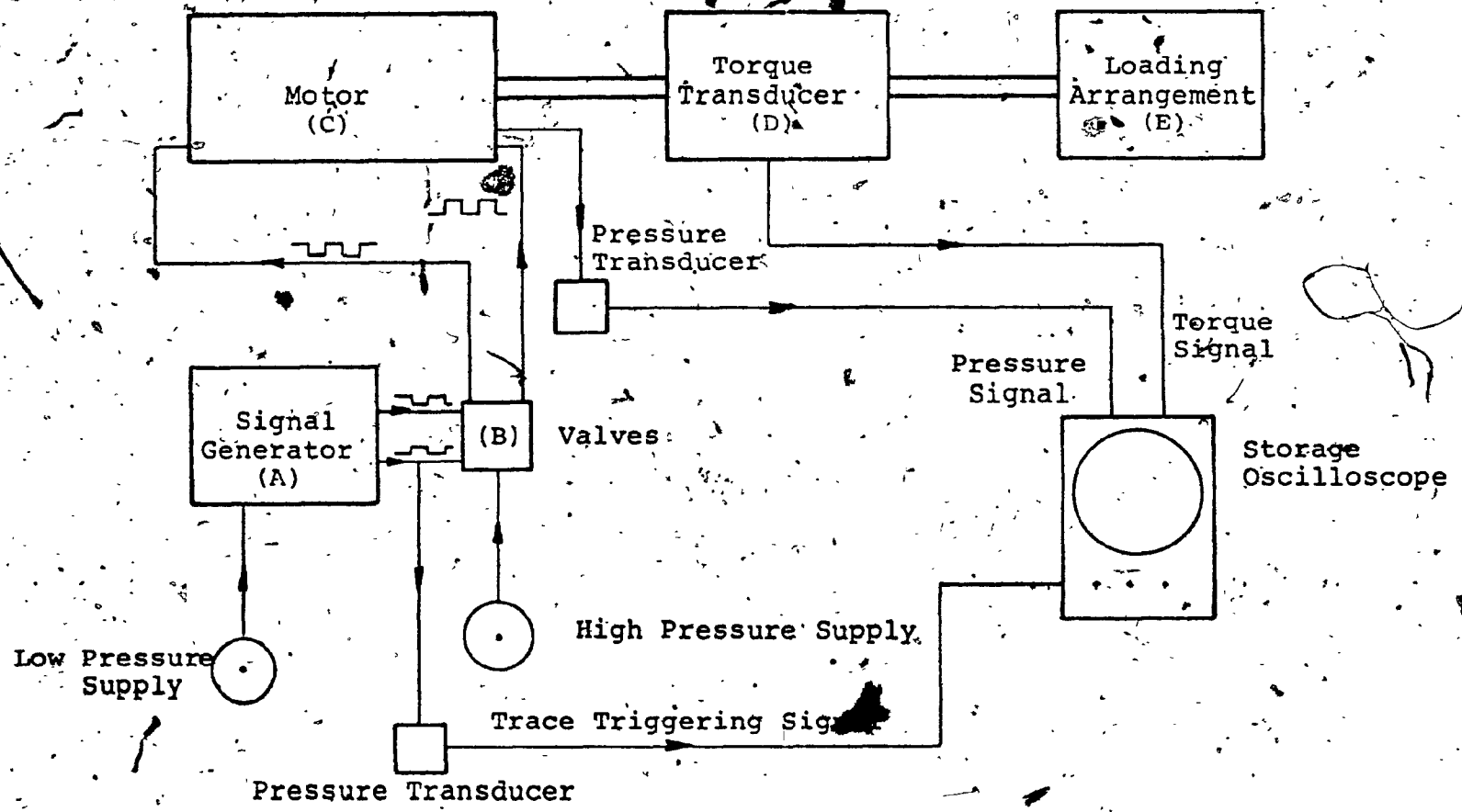

Fig. III.5a: Schematic Diagram of the System Used in the Analysis.

motor actuation. Hence, two parallel-connected, three way valves are used as power amplifiers for each generator output. The output of each power amplifier is connected to a motor port. The motor has already been described in Section III.3. The motor shaft drives the torque transducer shaft, which in turn drives the loading arrangement. The loading system is composed of a flywheel disc providing the inertia load, and a block type brake acting on the periphery of the flywheel, creating a frictional torque opposing motion. The flywheel has provisions for adding more discs to it to increase the load inertia. The force acting on the friction brake results from deadweights attached to the brake arm as shown in Fig. III.5b. Thus, the frictional torque can be varied by adding or removing the deadweights.

The input and output of the system are measured and recorded for analysis using the torque transducer (D), two pressure transducers, and a storage oscilloscope.

One of the pressure transducers monitors the signal from the fluidic oscillator to indicate the beginning of each step and simultaneously triggers the oscilloscope trace. The other is mounted on the motor body and monitors the pressure inside one of the motor chambers under an end cap. The torque transducer, mounted in between the motor output shaft and the input shaft of the load, measures the dynamic torque by measuring the twisting strain in the transducer shaft.

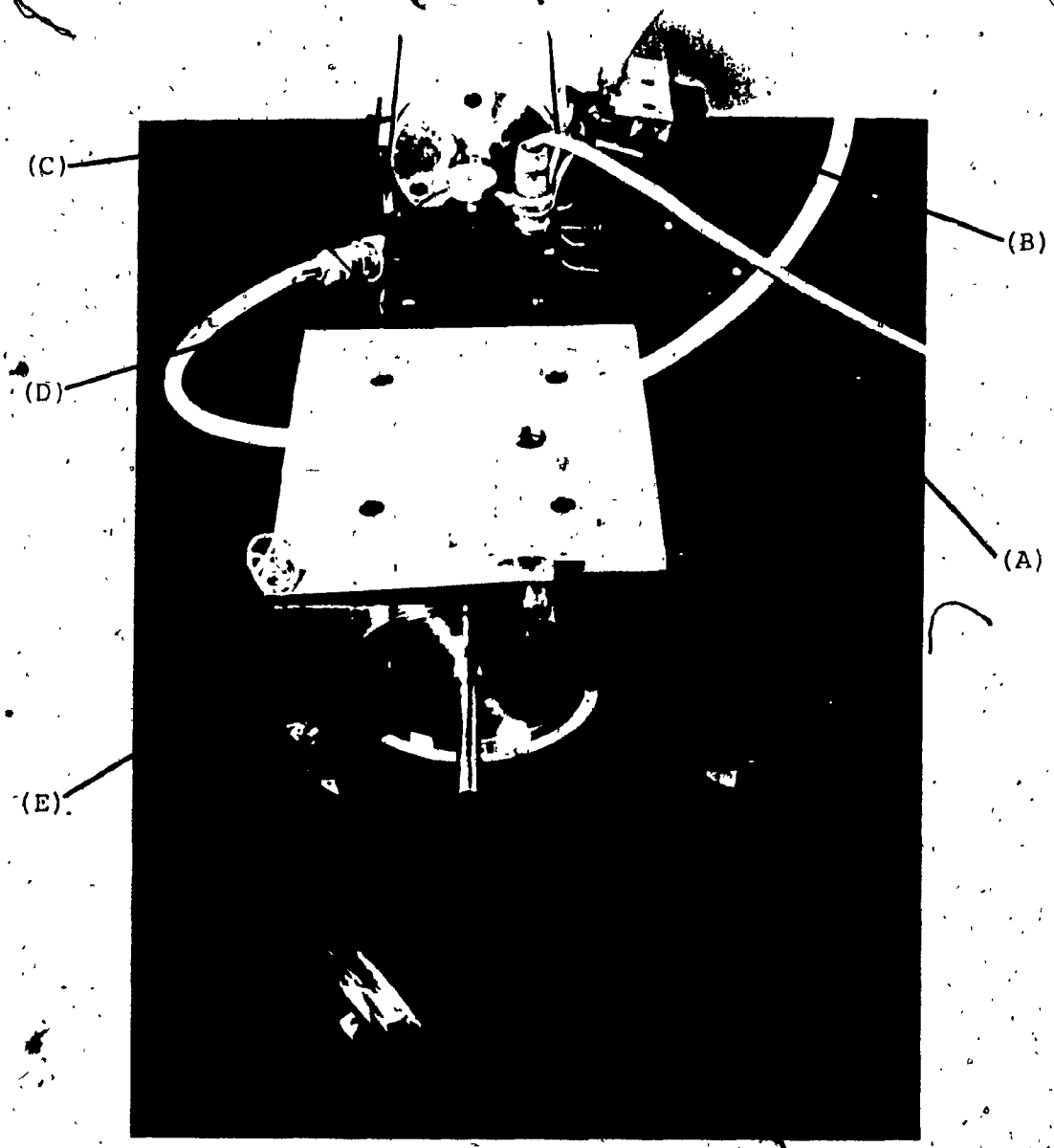

A = Signal Generator
B = Valves
C = Motor
D = Torque Transducer
E = Loading Arrangement

Fig. III.5b: Photograph of the System Used in the Analysis.

CHAPTER IV

THEORETICAL ANALYSIS OF THE STEPPING MOTOR

IV.1 Basic Geometric Parameters

Since the operational concept of the motor utilizes a cam-actuator mechanism, the geometry of both the cam and the actuator influence the operational characteristics and performance of the motor. Figure IV.1 shows a schematic diagram of the motor according to configuration [D]. Referring to Fig. IV.1, the "driving profile" of the cam is defined by the following geometric parameters: the step angle α, the offset angle ε, the addendum and dedendum radii R_a and R_d respectively, and the profile curve itself with its corresponding angle of attack ϕ. The actuator geometry is defined by the tip radius R_t. The following is an analysis and discussion of these parameters and their effect on the performance of the motor.

IV.1.a Step Angle (or Angle of Resolution α)

The cam is asymmetric in design [Section (III.1)]. This asymmetry results in the use of only an odd number of teeth on the cam. The number of teeth is thus given by:

$$N_t = 2n + 1 \qquad \text{(IV.1)}$$

where n is an integer greater than zero. Each tooth on the cam is covered in two steps. This results in $2.(N_t)$ steps per revolution of the output shaft. Hence the step angle or

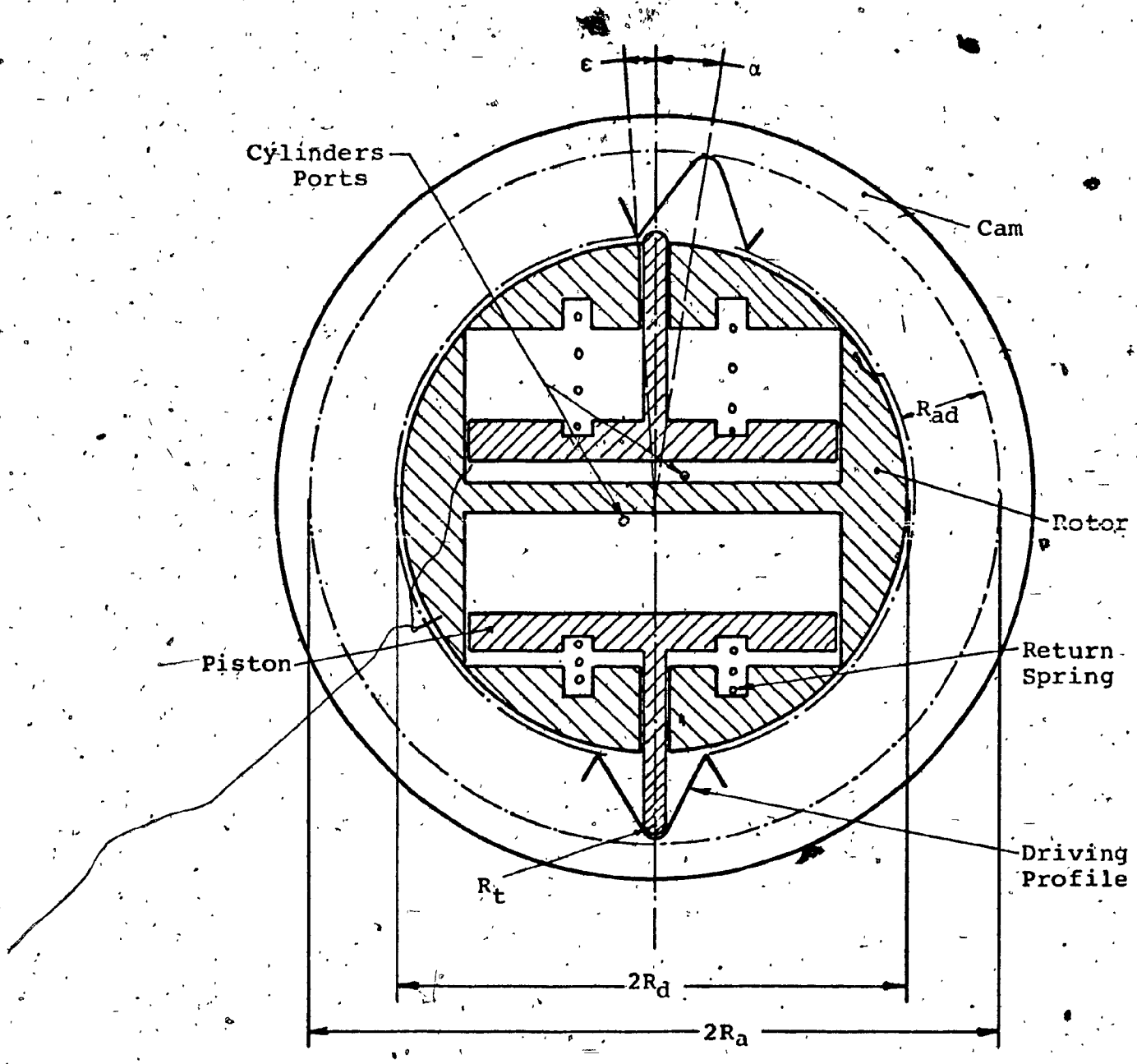

Fig. IV.1: Schematic Diagram of the Motor According to Configuration [D].

angle of resolution α is calculated as follows:

$$\alpha = \frac{2\pi}{2N_t}$$

$$= \frac{\pi}{N_t}, \qquad \text{(IV.2)}$$

From a practical point of view, reasonable values of n may be chosen between n = 3 resulting in $\alpha = 25.714°$ and n = 12 resulting in $\alpha = 7.200°$. The use of a value of n less than 3 or greater than 12 would result in impractical designs.

IV.1.b Offset Angle ε

The importance of the offset angle ε to the operation of the motor can be realized by considering Fig. III.1 and visualizing a zero offset (i.e. $\varepsilon = 0$). In such a case, the piston rod (B) would hit the leading extremity (c) of the driving profile (cd) during its downward motion, thereby jamming the motor. Thus, offsetting the leading extremity (c) of the driving profile ensures continuous operation of the motor. Referring to Fig. IV.2, the value of the minimum offset angle ε_m required to ensure smooth operation of the motor is dependent upon the piston rod (actuator) tip radius R_t, the dedendum radius of the cam R_d and the initial angle of attack ϕ_0. Thus, the minimum offset angle can be expressed as

$$\varepsilon_m = \sin^{-1} \frac{X}{R_p}$$

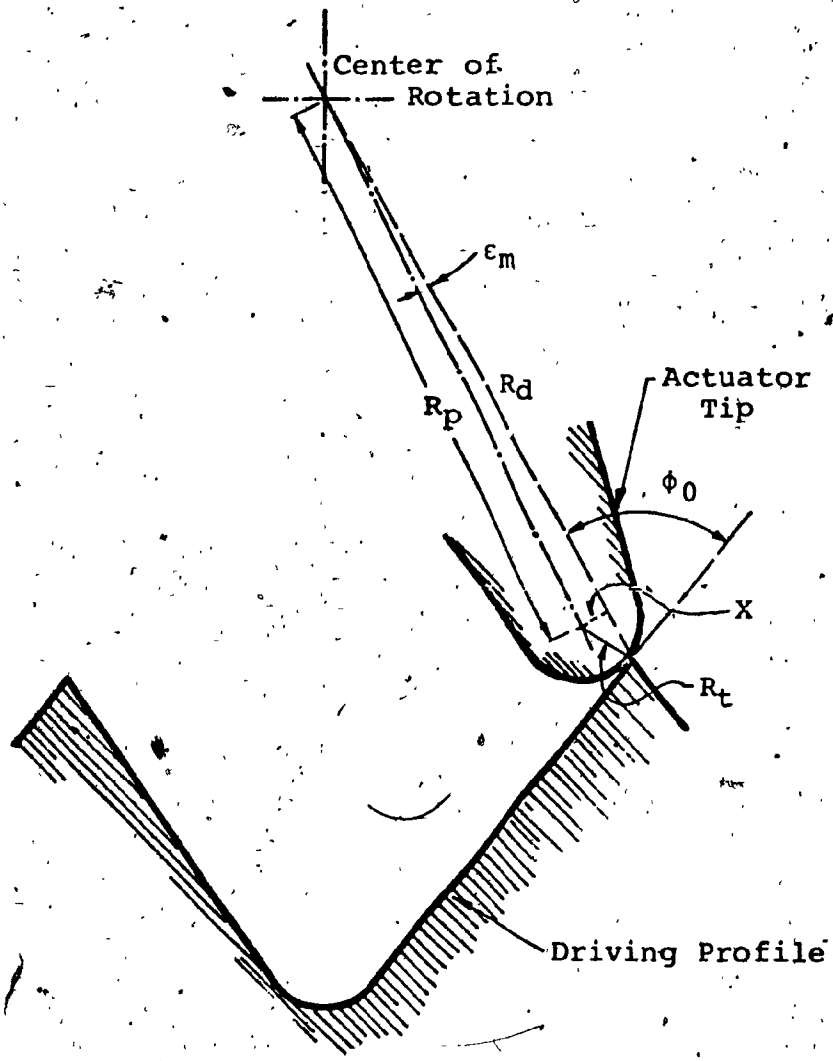

Fig. IV.2: Minimum Offset Angle of the Driving Profile.

where

$$X = R_t \sin(\pi/2 - \phi_0)$$

and

$$R_p = [R_t^2 + R_d^2 - 2R_tR_d \cos(\pi/2 - \phi_0)]^{\frac{1}{2}}$$

Thus, $$\varepsilon_m = \sin^{-1} \frac{R_t^* \cos\phi_0}{[R_t^{*2} + 1 - 2R_t^* \sin\phi_0]^{\frac{1}{2}}} \qquad \text{(IV.3a)}$$

where R_t^* is the nondimensionalized piston rod tip radius defined as $R_t^* = \frac{R_t}{R_d}$.

Though Equation IV.3a gives the minimum offset angle, it does not consider the error resulting from machining tolerances. The maximum error in the offset angle results when the cumulative tolerances are such that R_t^* is a maximum and ϕ_0 is a minimum. For normal machining tolerances used in production (± 0.001" and ± 0.1°), a value of the offset angle $\varepsilon = (\varepsilon_m + 0.5°)$ is sufficient to ensure trouble-free operation. However, in general, the offset angle can be expressed as

$$\varepsilon \geq \varepsilon_m \qquad \text{(IV.3b)}$$

with the upper limit governed by the particular design.

Figure IV.3, which is a plot of Eq. IV.3, shows that the minimum offset angle ε_m increases with an increase in R_t^*, but decreases as the initial angle of attack ϕ_0 is increased.

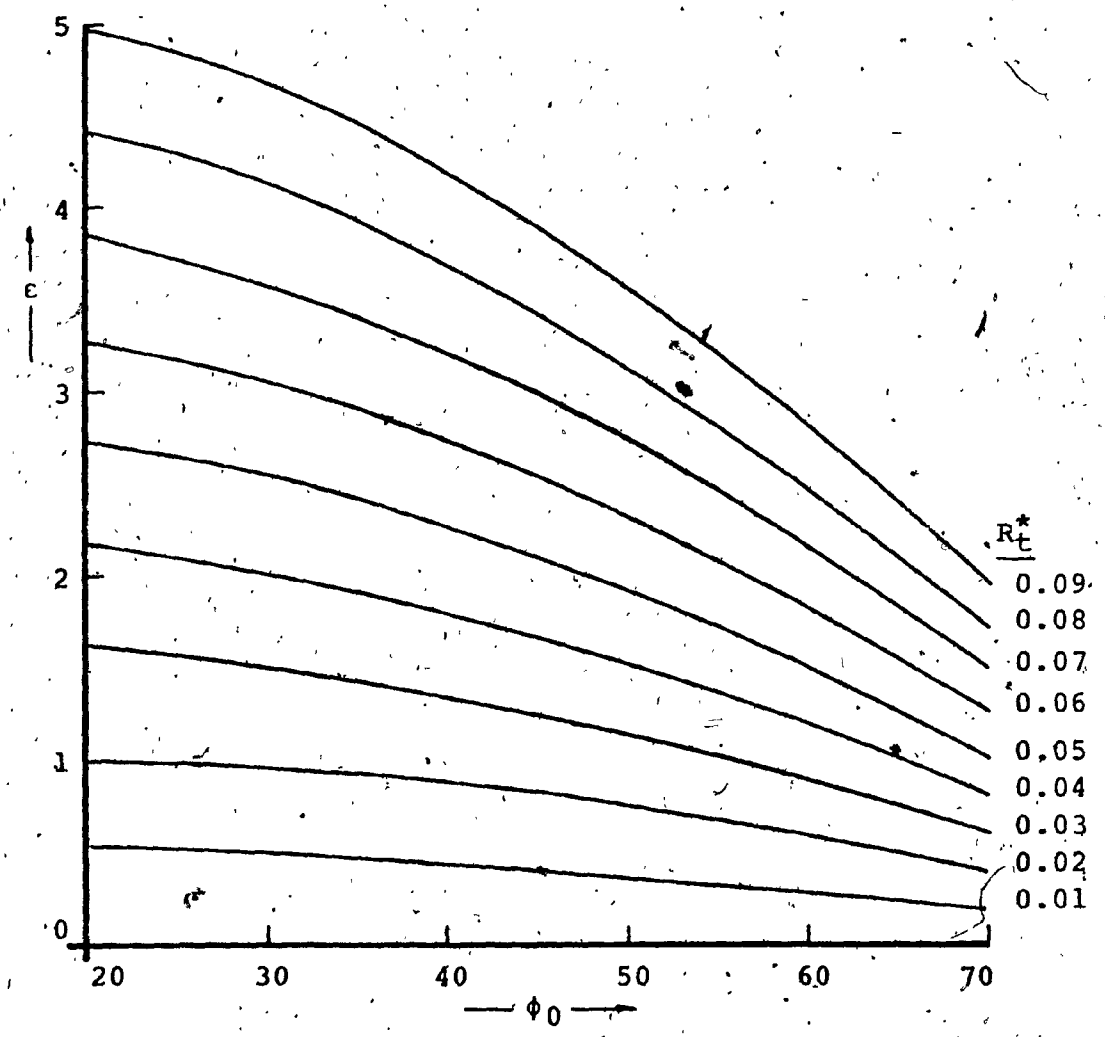

Fig. IV.3: Minimum Offset Angle Versus Initial Angle of Attack.

IV.1.c Dedendum and Addendum Radii (R_d, R_a)

Since the cam is likened to an internal gear, the terms dedendum and addendum radii pertaining to gear geometry are used here to describe the inner radius and the outer radius of the cam respectively. The value of the dedendum radius R_d determines the largest diameter cylinder that can be housed within the space provided by the cam. The depth of the cam tooth R_{ad} given by

$$R_{ad} = R_a - R_d$$

determines the minimum stroke required of the cylinder. Referring to Fig. IV.4, the radius R_{CL} of the largest cylinder that can be used with particular values of R_d, R_a and H [where H is the height of the piston plus half the thickness of the separator plate] can be calculated as follows:

$$R_{CL} = [R_d^2 - (R_a - R_d + H)^2]^{\frac{1}{2}} \qquad \text{(IV.4a)}$$

Expanding and nondimensionalizing Eq. IV.4a becomes:

$$R^*_{CL} = [-R^{*2}_a - H^{*2} - 2R^*_aH^* + 2H^* + 2R^*_a]^{\frac{1}{2}}$$

where R^*_{CL} and R^*_a are the nondimensionalized radii of the cylinder and addendum circle given by $R^*_{CL} = R_{CL}/R_d$ and $R^*_a = R_a/R_d$ respectively. H^* is the nondimensionalized height of the piston and half the separator plate given as $H^* = H/R_d$.

Further simplification of the above equation yields

$$R^*_{CL} = [2(R^*_a + H^*) - (R^*_a + H^*)^2]^{\frac{1}{2}}$$

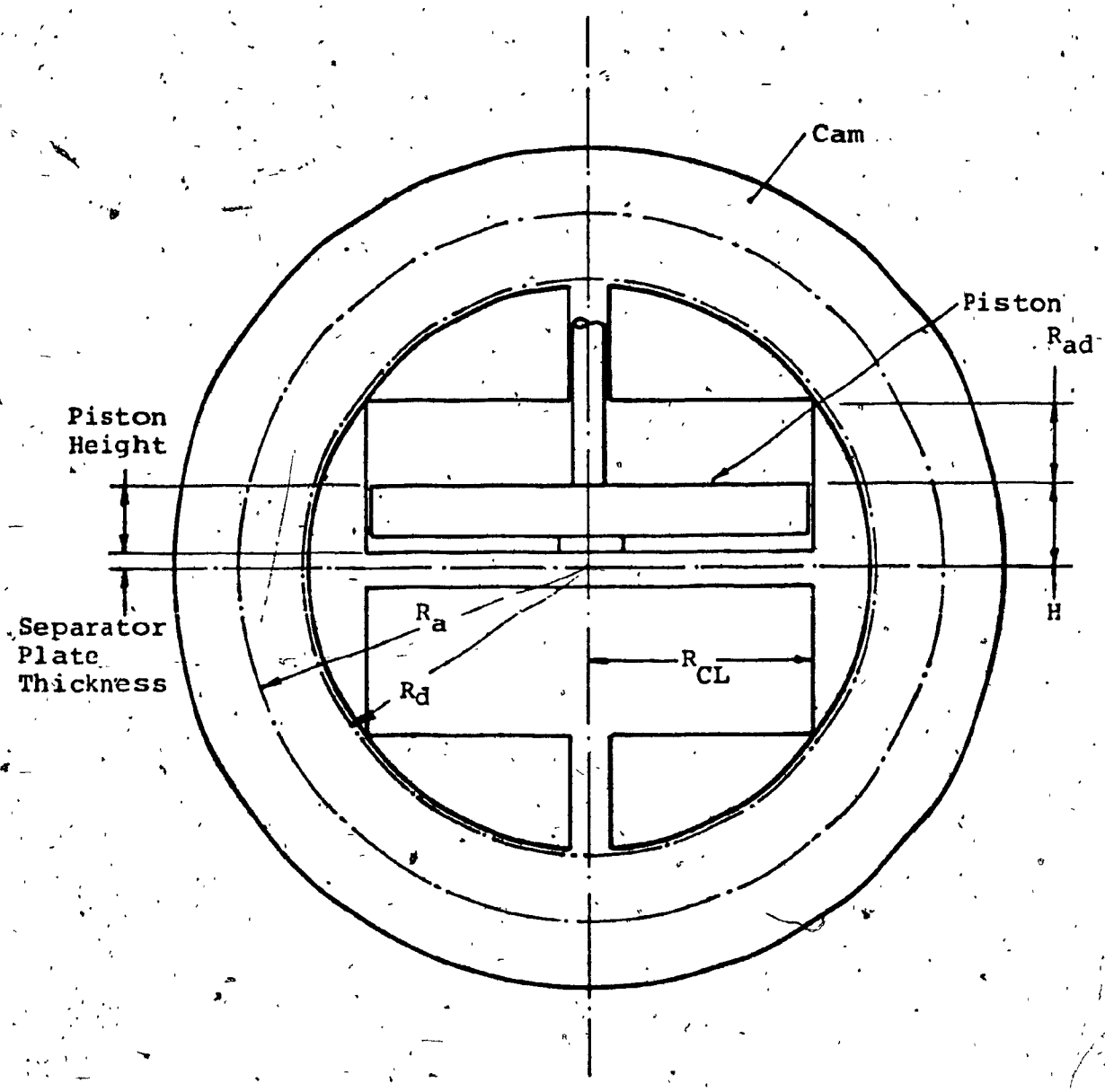

Fig. IV.4: Geometric Relation of the Motor Rotor With Respect to the Cam Geometry.

Thus, the nondimensional area A^*_{CL} of the largest cylinder that can be housed within a particular cam, may be calculated from the following equation:

$$A^*_{CL} = \frac{\text{area of cylinder } (\pi R^2_{CL})}{\text{cam area based on dedendum radius } (\pi R_d{}^2)}$$

$$= (R^*_a + H^*)(2 - R^*_a - H^*) \qquad \text{(IV.4b)}$$

A plot of this relation is shown in Fig. IV.5. The maximum area of a cylinder that can be housed in the space provided by the cam can be determined from this graph once the value of H^* is decided upon. The figure also shows that with the increase of both H^* and R^*_a, the maximum area of the cylinder that can be used decreases.

IV.1.d Profile Curve and Angle of Attack

The instantaneous radius r of the cam actuator as a function of the angle θ during the stepping action gives the equation of the profile curve in polar coordinates with reference to the axis of rotation. Thus, in general

$$r = f(\theta) \qquad \text{(IV.5)}$$

is the equation of the profile curve. This instantaneous radius r is the arm of the torque acting on the cam. The angle of attack ϕ, defined as the angle between the tangent to the profile curve and the instantaneous radius to the curve at any point, is the angle by which the piston force acts on the cam. Referring to Fig. IV.6, the angle of

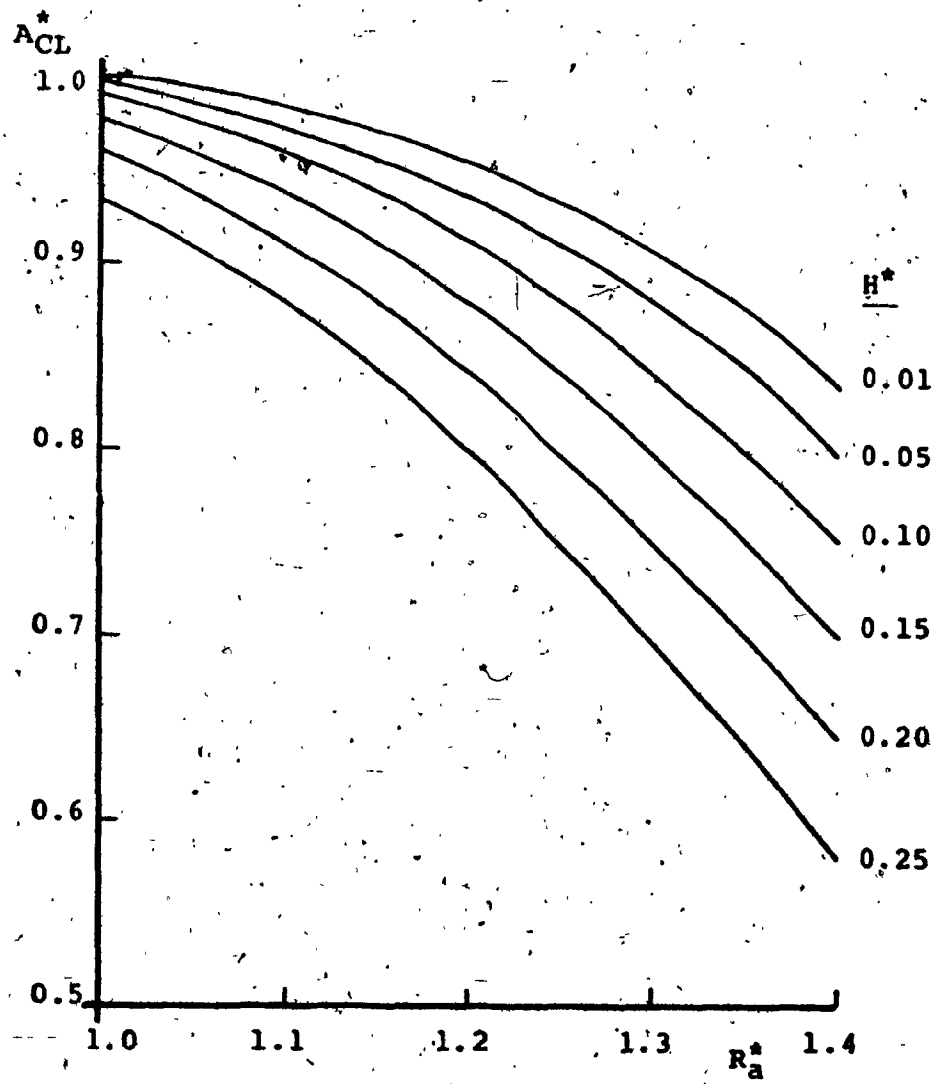

Fig. IV.5: Maximum Usable Cylinder Area as a Function of the Cam Radius.

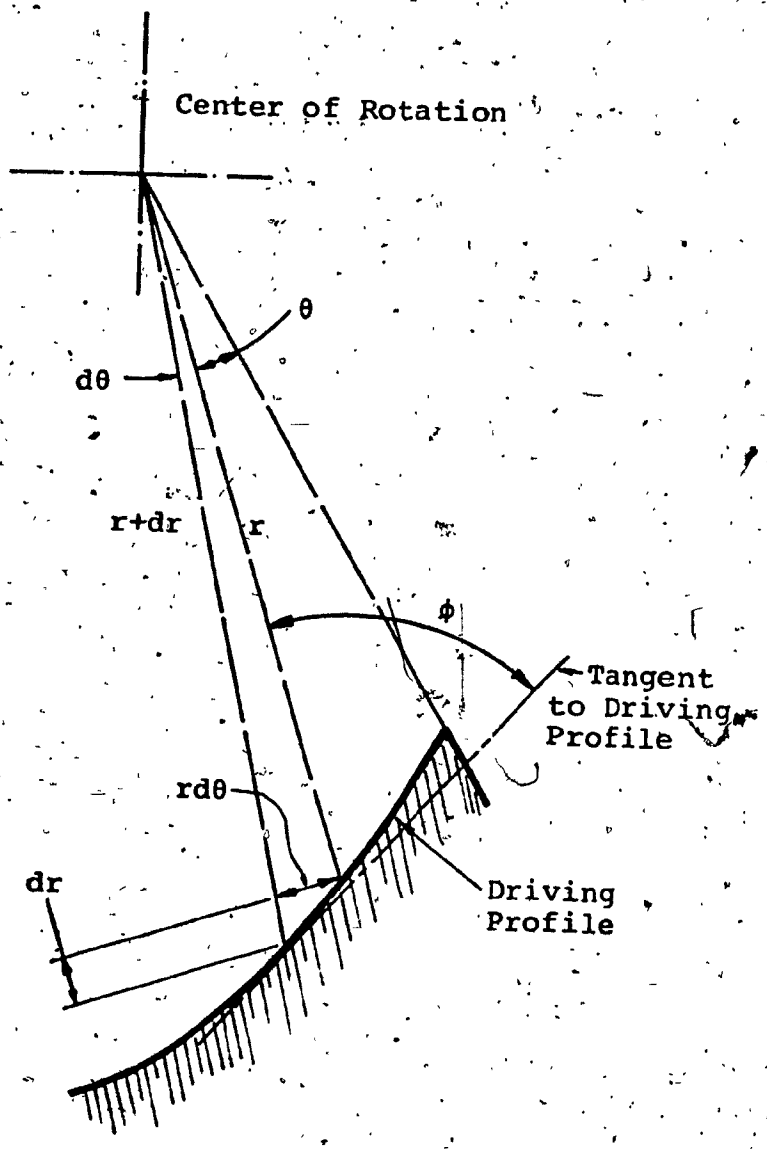

Fig. IV.6: Angle of Attack in Relation to the Cam Profile.

attack is given by:

$$\cot \phi = \frac{dr}{rd\theta}$$

$$\phi = \cot^{-1} \left[\frac{dr}{d\theta}/r\right] \qquad \text{(IV.6a)}$$

which can also be written as

$$\phi = \cot^{-1} \left[\frac{f'(\theta)}{f(\theta)}\right] \qquad \text{(IV.6b)}$$

Although numerous curves can be used for the driving profile, a straight line ending with a circular curve as shown in Fig. IV.7 is used in the prototype because of simplicity and ease of machinability. The equation for this type of profile curve is given in nondimensional form in Appendix B by:

$$\left.\begin{aligned} r^* &= \frac{a \tan\xi}{\tan\xi \cos\theta - \sin\theta} && 0° < \theta \leq \lambda \\ r^* &= R_t^* \cos\delta + (R_a^* - R_t^*) \cos(\alpha_s - \theta) && \lambda \leq \theta \leq \alpha_s \end{aligned}\right\} \qquad \text{(IV.7)}$$

where $\xi = \pi - \phi_0$

IV.2 Static Torque Developed by Motor

When the motor cylinder is pressurized, the net force F on the piston due to the cylinder pressure p_C acting on the cylinder area A_C, results in a static torque T_M which tends to tilt the cylinder housing. The torque developed by a given pressure is mainly a function of the cam geometry, although it is also influenced by the coefficients of friction μ_1 and μ_2 between the cam and actuator, and between

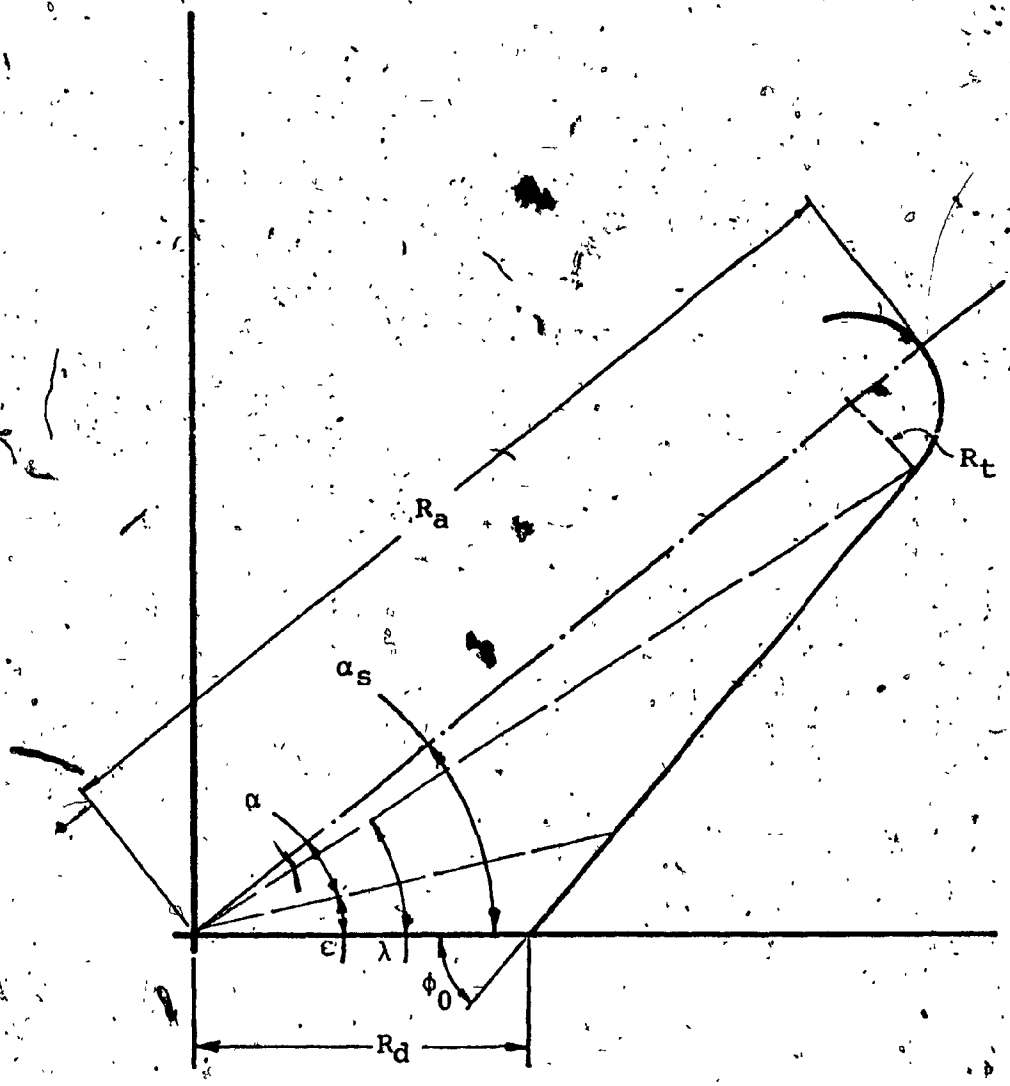

Fig. IV.7: Driving Profile Used for the Cam of the Prototype Motor.

the actuator and its guide, respectively. These frictional coefficients are in turn determined by the choice of materials of the contacting members.

Figure IV.8 shows the free body diagrams of the piston (Fig. IV.8a) and the cylinder (Fig. IV.8b), respectively. A static balance of the forces on the two components of Fig. IV.8 results in the following set of equations.

Static force and torque balance of the piston (Fig. IV.8a):

$$R_1 - R_2 + \mu_1 N \sin\phi - N \cos\phi = 0 \qquad \text{(IV.8a)}$$

$$F - N \sin\phi - \mu_1 N \cos\phi - \mu_2 (R_1 + R_2) = 0 \qquad \text{(IV.8b)}$$

$$R_1 \ell_1 + \mu_1 N r \sin\phi - R_2 \ell_2 - N r \cos\phi = 0 \qquad \text{(IV.8c)}$$

where F is the net force acting on the actuator and is given by:

$$F = p_C A_C - K_S r - f_{CS} \geq 0 \qquad \text{(IV.9)}$$

where K_S is the spring constant of the cylinder return spring and f_{CS} is a constant force accounting for the piston seal friction at the beginning of motion and the constant part of the return spring force. (f_{CS} = initial spring force + piston seal friction force - $K_S R_d$).

This force is limited to positive values, since a negative F allows the actuator to disengage from the cam surface, a condition that does not occur during stepping.

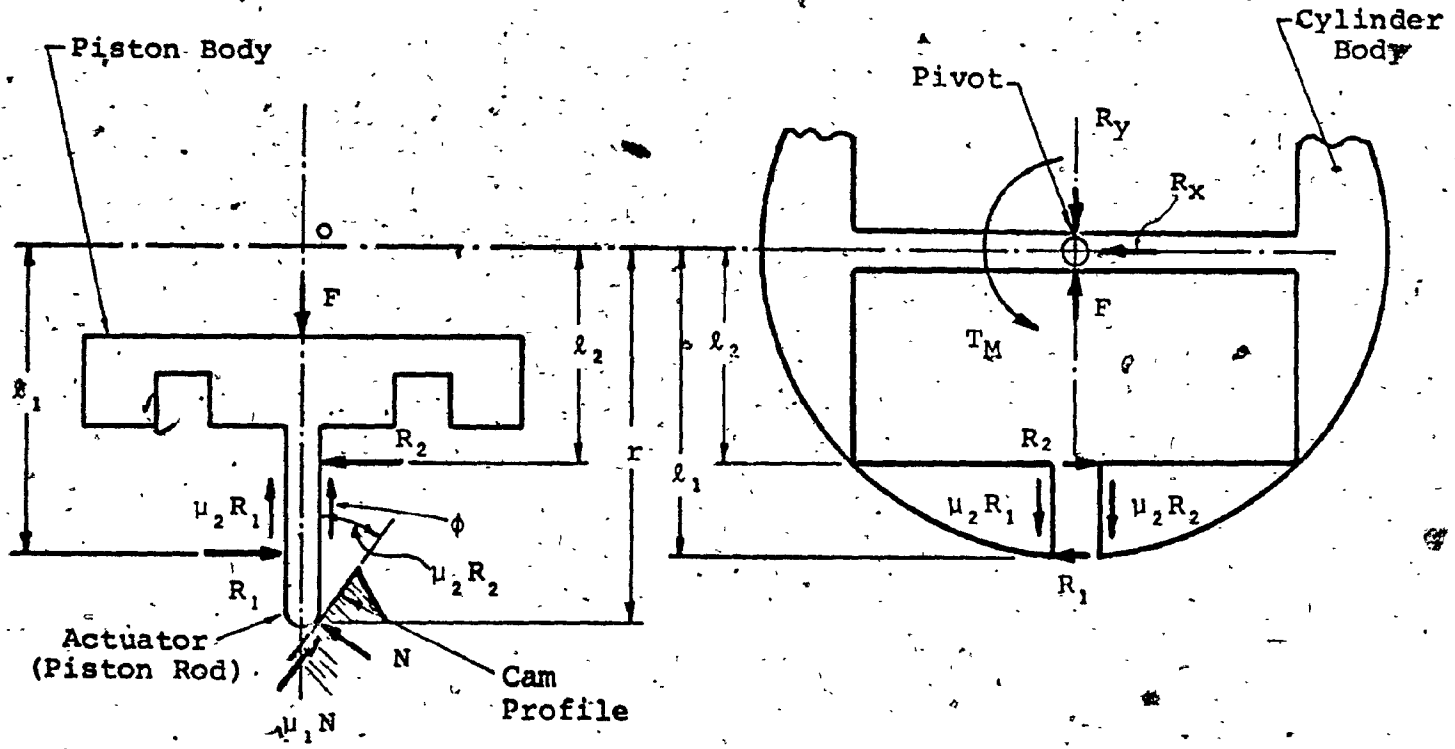

Fig. IV.8a

Fig. IV.8b

Fig. IV.8: Free Body Diagrams of the Piston and Cylinder.

Static force and torque balance of the cylinder (Fig. IV.8b):

$$R_1 - R_2 + R_x = 0 \qquad \text{(IV.10a)}$$

$$R_y + \mu_2 (R_1 + R_2) - F = 0 \qquad \text{(IV.10b)}$$

$$T_M - R_1 \ell_1 + R_2 \ell_2 = 0 \qquad \text{(IV.10c)}$$

The solution of Eqs. IV.8 and IV.10 is given by Eq. C-18 [Appendix C] as

$$T_M = \frac{F\ r\ S}{S+\mu_2 (2r-2R_d+S)} \cdot \frac{\cos\phi-\mu_1 \sin\phi}{\sin\phi+\mu_1 \cos\phi} \qquad \text{(IV.11)}$$

where S = piston rod guide length.

Rearranging Eq. IV.11 and substituting for F and ϕ from Eqs. IV.6a and IV.9, the static torque is given by

$$T_M = \frac{(p_C A_C - K_S r - f_{CS}) rs}{S+\mu_2 (2r-2R_d+S)} \cdot \frac{dr/d\theta-\mu_1 r}{r+\mu_1\ dr/d\theta} \qquad \text{(IV.12a)}$$

where

$$p_C A_C - K_S r - f_{CS} \geq 0$$

Since the relation between the instantaneous radius r and the displacement θ for most profiles can be expressed as:

$$r = R_d f(\theta)$$

and utilizing Eq. IV.6b, Eq. IV.12a becomes:

$$\frac{T_M}{FR_d} = \frac{f(\theta)}{\left[1+2\ \frac{\mu_2}{S^*}\left(f(\theta)-1+\frac{S^*}{2}\right)\right]} \cdot \frac{f'(\theta)-\mu_1 f(\theta)}{f(\theta)+\mu_1 f'(\theta)} \qquad \text{(IV.12b)}$$

where $S^* = S/R_d$ is the nondimensionalized piston rod guide height.

When the supply pressure P_s (gage) is used in Eq. IV.12b, a "stall force" F_s is developed in the cylinder, resulting in a stall torque T_{st}. The relation given by Eq. IV.12b in this case becomes the stall torque function Ξ, and is defined as:

$$\Xi = \frac{T_{st}}{F_s R_d} \qquad \text{(IV.12c)}$$

At the beginning of the step (at $\theta = 0$), the instantaneous radius r is the same as the inner radius of the cam R_d, thus making $f(\theta) = 1$. Furthermore, $f'(\theta)/f(\theta)$ at $\theta = 0$ is proportional to the initial angle of attack of the profile ϕ_0:

$$[f'(\theta)/f(\theta)]_{\theta=0} = \cot\phi_0$$

Thus the stall torque function at the beginning of the step Ξ_0 becomes:

$$\Xi_0 = \frac{1}{1+2\frac{\mu_2}{S^*}\left(\frac{S^*}{2}\right)} \cdot \frac{\cot\phi_0 - \mu_1}{1 + \mu_1\cot\phi_0}$$

$$= \frac{1}{1 + \mu_2} \cot(\phi_0 + \psi_1) \qquad \text{(IV.12d)}$$

where ψ_1 is the friction angle between the cam and actuator.

The stall torque function Ξ is a convenient measure of the effectiveness of the motor as a torque generating device. Figure V.1 of Chapter V shows a plot of this function versus the displacement for the prototype motor.

IV.3 Dynamic Analysis of the Motor-Load System

The experimental setup used in the dynamic analysis has already been described in Section III.4. The mathematical model describing the system of Fig. III.5 is best visualized through the linear flow graph [Ref. 14] shown in Fig. IV.9. The model consists of a pneumatic section and a mechanical section, which are interconnected through a pneumatic-to-mechanical gyrator corresponding to the cylinder-actuator-cam arrangement in hardware.

The pneumatic section of the graph consists of four components namely, the control valve (V), the connecting line between the valve and the motor (L), the rotary junction (J) which forms a rotating connection leading to the cylinder, and the cylinder (C) itself. In this analysis, these components are modelled by resistances (R_V, R_L, R_J, and R_C), and capacitances (C_V, C_L, C_J, and C_C) as shown in Fig. IV.9.

The link between the pneumatic section and the mechanical section is the cylinder-actuator-cam arrangement. This arrangement transforms the cylinder pressure into a torque T_M, and is represented on the flow graph by a gyrator.

In the mechanical section, part of the motor torque T_M is consumed in overcoming the motor inertia J_M, and output shaft seal friction μ_s. The balance of T_M is passed on to the load through the motor shaft (of torsional stiffness K_M),

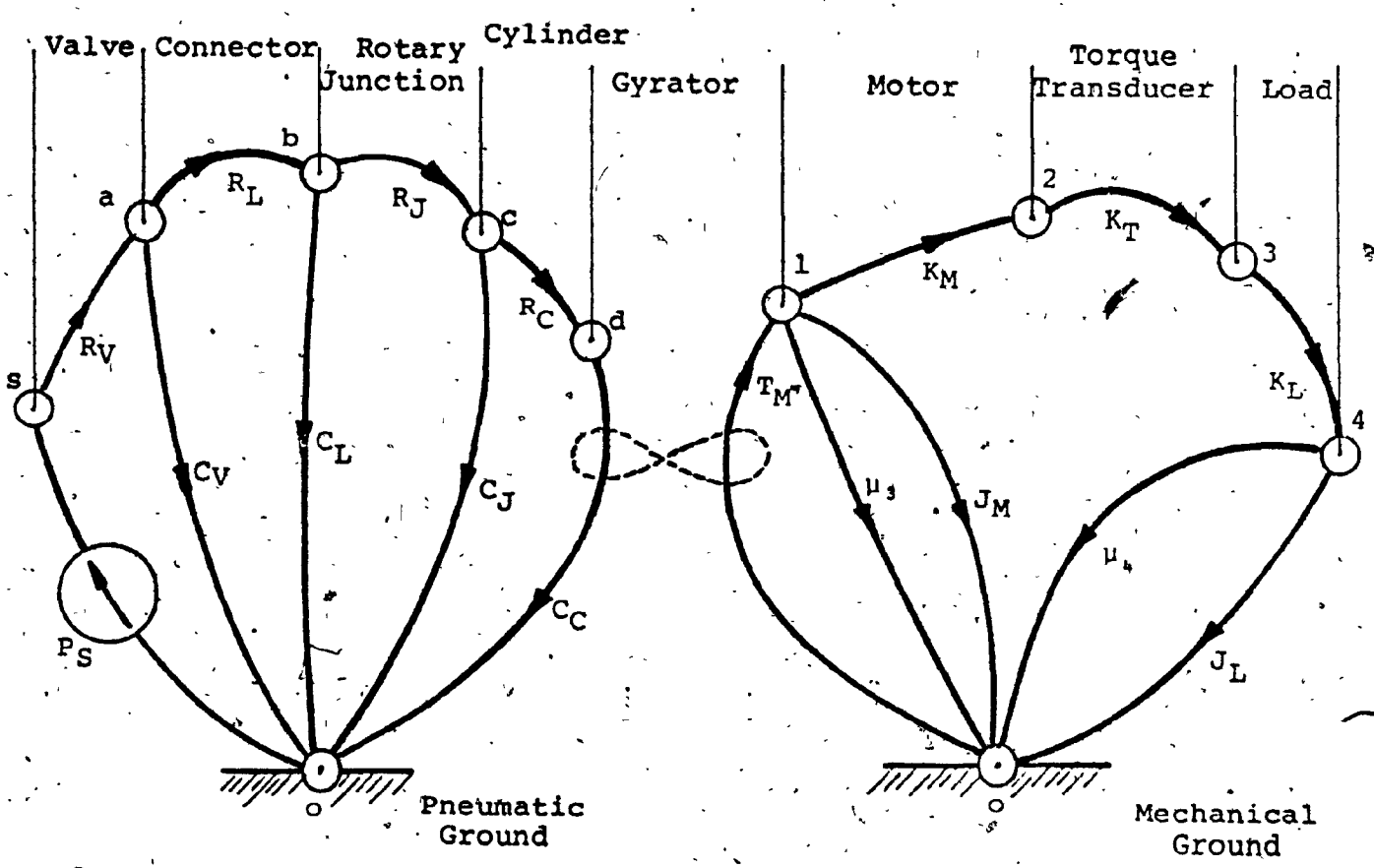

Fig. IV.9: Linear Flow Graph Representation of the System Used in the Analysis.

torque transducer shaft (of torsional stiffness K_T, and negligible inertia), and load shaft (of torsional stiffness K_L). This balance of T_M is finally utilized in moving the load inertia J_L and in overcoming the load friction μ_4. In the analysis of the mechanical section the angles θ_1, θ_2, θ_3 and θ_4 indicate the angles of displacement of the motor, the beginning and the end of the torque transducer shaft, and the load respectively. These angles have initial values of ϵ.

The set of simultaneous equations describing the entire system are nonlinear, and the input-output relation of each component is affected by the neighboring components. Also some components (e.g. the cylinder), have intrinsic feedback loops, thus introducing further complications. To reduce the complexity of the solution of the system equations, and to get a better understanding of the input-output relations, the variables and parameters are nondimensionalized as follows (the nondimensional parameters are indicated by an asterisk):

1) All areas of fluid passages are nondimensionalized with respect to the maximum opening of the control valve,

e.g. $a_V^* = a_V / A_V$.

2) Volumes are expressed as ratios of the total volume V_t of the system at start,

e.g. $V_V^* = V_V/V_t$

where $V_t = (V_V + V_L + V_J + V_{C(0)})$.

3) Temperatures are expressed as ratios of the constant supply temperature t_s,

e.g. $t_a^* = t_a/t_s$.

4) All pressures are expressed as ratios of the constant supply pressure P_s,

e.g. $P_a^* = P_a/P_s$.

5) All flow rates are expressed as a ratio to the maximum (choked) flow across the valve at its maximum opening,

e.g. $W_{sa}^* = W_{sa}/(W_{sa})_{max}$

where

$$(W_{sa})_{max} = \frac{A_V P_s}{\sqrt{t_s}} \sqrt{\frac{k}{R} \left(\frac{2}{k+1}\right)^{\frac{k+1}{k-1}}}$$ [Eq. 2.1.13, Ref. 17]

6) Masses of air occupying different components are expressed as ratios of the mass of air occupying the total system at start

e.g. $m_V^* = m_V/m_t$

7) A nondimensional time τ is utilized throughout and is given by

$\tau = \Omega_L t$

where Ω_L is the combined natural frequency of the load shaft and torque transducer shaft assembly.

Ω_L is given by

$\Omega_L = \sqrt{K_E/J_L}$

8) All angular displacements are expressed as ratios to the angle of the driving profile of the motor,

e.g. $\theta_1^* = \theta_1/\alpha_s$

9) Forces are nondimensionalized with respect to the maximum pressure force on the piston $P_s A_C$

e.g. $F^* = F/P_s A_C$

10) All torques are expressed as ratios of a torque quantity given by $P_s A_C R_d$

e.g. $T_M^* = T_M/P_s A_C R_d$

11) All torsional stiffnesses are expressed as a ratio of the combined torsional stiffness of the load and torque transducer shafts [combined according to formulae in Ref. 18]

e.g. $K_L^* = K_L/K_E$

The analysis of the three sections of the linear flow graph follows.

IV.3.a Analysis of the Pneumatic Section

In the following analysis, the symbols p_{ij} and t_{ij} will refer to the pressure ratio and temperature ratio between the two points i and j. Thus,

$$p_{ij} = \frac{p_i}{p_j}$$

and

$$t_{ij} = \frac{t_i}{t_j}$$

Also $p^*_{n(0)}$ and $m^*_{m(0)}$ indicate in general the non-dimensional initial condition of pressure at junction n, and nondimensional initial condition of mass of fluid in component m. The upper limit of all integrations τ_f is the nondimensional time at which the motor and load come to rest after performing a step.

A certain number of parameter groups appears frequently in the analysis due to nondimensionalizing and these are defined as follows:

$$\beta_1 = 1/A_V \sqrt{k\left(\frac{2}{k+1}\right)^{\frac{k+1}{k-1}}}$$

$$\beta_2 = t_s (W_{sa})_{max}\, kR/(P_s \Omega_L)$$

$$\beta_3 = 1/(V_V + V_L + V_J + V_{C(0)})$$

$$\Lambda_1 = A_V \sqrt{Rkt_s \left(\frac{2}{k+1}\right)^{\frac{k+1}{k-1}}} \Big/ (V_V + V_L + V_J + V_{C(0)})\Omega_L$$

Referring to Fig. IV.9, the analysis of the pneumatic components, starting from left to right, now follows:

Control Valve:

The control valve is modelled by an equivalent orifice whose maximum opening corresponds to the maximum opening of the valve A_V [Appendix D], and a volume which is the internal volume of the valve V_V. The orifice thus corresponds to the resistance, and the volume the capacitance, in the equivalent circuit. When the valve receives an actuating signal, a finite time elapses before its maximum opening is reached. It is assumed here that the valve opening a_V linearly progresses from the fully closed position (i.v. $a_V = 0$) at time $t = 0$ to the fully opened position (i.e. $a_V = A_V$) at time τ_V, [Appendix D].

Thus, the valve opening can be expressed as:

$$a_V = A_V \frac{t}{\tau_V} \qquad t < \tau_V$$

$$= A_V \qquad t \geq \tau_V$$

In nondimensional form, this function becomes

$$a_V^* = \frac{t}{\tau_V} \qquad t < \tau_V$$

$$= 1 \qquad t \geq \tau_V \qquad \text{(IV.13a)}$$

When the ratio between the downstream and upstream pressures of the valve is below or equal to the critical ratio given by

$$\left(\frac{2}{k+1}\right)^{\frac{k}{k-1}}$$

the flow through the valve equivalent orifice becomes choked. When the downstream to upstream pressure ratio exceeds the critical ratio, the flow is subsonic. Thus, the flow through the valve equivalent orifice under the above two conditions is given by

$$W_{sa} = \frac{a_v P_s}{\sqrt{t_s}} \sqrt{\frac{k}{R}\left(\frac{2}{k+1}\right)^{\frac{k+1}{k-1}}} \quad \text{when } P_{as} \le \left(\frac{2}{k+1}\right)^{\frac{k}{k-1}}$$

[Eq. 2.1.13 Ref. 17]

$$= \frac{a_v P_s}{\sqrt{t_s}} \sqrt{\frac{2k}{R(k-1)}} \, (P_{as})^{1/k} \sqrt{1-(P_{as})^{\frac{k-1}{k}}}$$

when $P_{as} > \left(\frac{2}{k-1}\right)^{\frac{k}{k-1}}$ [Eq. 3.86 Ref.16]

When nondimensionalized, these flow equations become

$$\left.\begin{aligned} W^*_{sa} &= \Lambda_2 a^*_v \quad \text{when } P_{as} \le \left(\frac{2}{k+1}\right)^{\frac{k}{k-1}} \\ &= \Lambda_3 a^*_v (P_{as})^{1/k} \sqrt{1-(P_{as})^{\frac{k-1}{k}}} \end{aligned}\right\} \quad \text{(IV.13b)}$$

$$\text{when } P_{as} > \left(\frac{2}{k+1}\right)^{\frac{k}{k-1}}$$

Summation of flows at the junction (a) in Fig. IV.9 yields the flow through the valve capacitance branch:

$$W^*_{ao} = W^*_{sa} - W^*_{ab} \quad \text{(IV.13c)}$$

The charging of the internal volume of the valve is given by Eq. E.15 [Appendix E]. In nondimensional form, this equation is as follows:

$$\frac{dP_a^*}{d\tau} = \Lambda_4 W_{ao}^* \qquad \text{(IV.13d)}$$

At any instant of time, the mass of air in the above internal volume is given by

$$m_V^* = \Lambda_1 \int_0^{\tau_f} W_{ao}^* \, d\tau + m_{V(0)}^* \qquad \text{(IV.13e)}$$

The temperature of the fluid at junction (a) is calculated from the state equation of a perfect gas using the nondimensional parameters. Thus,

$$t_a^* = \Lambda_5 P_a^* / m_V^* \qquad \text{(IV.13f)}$$

The nondimensional constants Λ_2 through Λ_5 are given as follows:

$$\Lambda_2 = \beta_1 A_V \sqrt{k \left(\frac{2}{k+1}\right)^{\frac{k+1}{k-1}}} \qquad \text{(IV.13g)}$$

$$= 1$$

$$\Lambda_3 = \beta_1 A_V \sqrt{\frac{2k}{k-1}} \qquad \text{(IV.13h)}$$

$$\Lambda_4 = \beta_2 / V_V \qquad \text{(IV.13i)}$$

$$\Lambda_5 = \beta_3 V_V \qquad \text{(IV.13j)}$$

Connecting Line:

The connecting line system consists of an entrance resistance followed by a transmission line. For the analysis, the resistance of the latter was lumped together with the entrance resistance. As a result, the transmission line could be considered lossless. However, calculations based

on fluid circuit theory [15], showed that the above lossless line could be represented by a pure capacitance at the frequency of operation. Thus, the connecting line was modelled on a resistance-capacitance basis. The assumptions made in this regard proved to be valid in view of the experimental correlation obtained.

The equations of the connecting line are derived in a similar manner to those of the control valve, with the exception of the flow equation through the entrance resistance of the line. The flow through this resistance is given by Eq. F.5 [Appendix F]. Thus, the describing equations of the connecting line are listed as follows:

$$W^*_{ab} = \Lambda_6 p^*_b \sqrt{(p_{ab}-1)(p_{ab}t_{ba}+1)} \Big/ \sqrt{t^*_b} \qquad \text{(IV.14a)}$$

[nondimensional form of Eq. F.5 Appendix F]

$$W^*_{bo} = W^*_{ab} - W^*_{bc} \qquad \text{(IV.14b)}$$

$$\frac{dp^*_b}{d\tau} = \Lambda_7 t^*_a W^*_{bo} \qquad \text{(IV.14c)}$$

[nondimensional form of Eq. E.15 Appendix E]

$$m^*_L = \Lambda_1 \int_0^{\tau_f} W^*_{bo}\, d\tau + m^*_L(0) \qquad \text{(IV.14d)}$$

$$t^*_b = \Lambda_8 p^*_b / m^*_L \qquad \text{(IV.14e)}$$

where

$$\Lambda_6 = \beta_1 A_L / \sqrt{c_L} \qquad \text{(IV.14f)}$$

$$\Lambda_7 = \beta_2 / V_L \qquad \text{(IV.14g)}$$

$$\Lambda_8 = \beta_3 V_L \qquad \text{(IV.14h)}$$

Rotary Junction:

The equations of the rotary junction are exactly similar in form to those of the connecting line. The listing of these equations is as follows:

$$W^*_{bc} = \Lambda_9 p^*_c \sqrt{(p_{bc}-1)(p_{bc}t_{cb}+1)} \Big/ \sqrt{t^*_c} \qquad \text{(IV.15a)}$$

$$W^*_{co} = W^*_{bc} - W^*_{cd} \qquad \text{(IV.15b)}$$

$$\frac{dp^*_c}{d\tau} = \Lambda_{10} t^*_b W^*_{co} \qquad \text{(IV.15c)}$$

$$m^*_J = \Lambda_1 \int_0^{\tau_f} W^*_{co}\, d\tau + m^*_J(0) \qquad \text{(IV.15d)}$$

$$t^*_c = \Lambda_{11} p^*_c / m^*_J \qquad \text{(IV.15e)}$$

where

$$\Lambda_9 = \beta_1 A_L / \sqrt{c_J} \qquad \text{(IV.15f)}$$

$$\Lambda_{10} = \beta_2 / V_J \qquad \text{(IV.15g)}$$

$$\Lambda_{11} = \beta_3 V_J \qquad \text{(IV.15h)}$$

Cylinder:

The describing equations of the cylinder are similar to those of the connecting line and the rotary junction with the exception of the charging equation of the cylinder volume. The cylinder volume is variable and the charging process of such a volume is given by Eq. E.14 [Appendix E]. The cylinder equations are listed as follows:

$$W^*_{cd} = W^*_{do} = \Lambda_{12} p^*_d \sqrt{(p_{cd}-1)(p_{cd}t_{dc}+1)} \Big/ \sqrt{t^*_d} \qquad \text{(IV.16a)}$$

$$\frac{dp^*_d}{d\tau} = \frac{t^*_c \; W^*_{do}}{\Lambda_{13}+\Lambda_{14}x^*} - \frac{p^*_d(dx^*/d\tau)}{\Lambda_{15}+\Lambda_{16}x^*} \qquad \text{(IV.16b)}$$

[nondimensional form of Eq.E.14 Appendix E]

$$m^*_C = \Lambda_1 \int_0^{\tau_f} W^*_{do} \, d\tau + m^*_{C(0)} \qquad \text{(IV.16c)}$$

$$t^*_d = \Lambda_{17} p^*_d V^*_C \; / \; m^*_C \qquad \text{(IV.16d)}$$

where

$$\Lambda_{12} = \beta_1 A_D / \sqrt{c_C} \qquad \text{(IV.16e)}$$

$$\Lambda_{13} = V_{C(0)} / \beta_2 \qquad \text{(IV.16f)}$$

$$\Lambda_{14} = A_C R_d / \beta_2 \qquad \text{(IV.16g)}$$

$$\Lambda_{15} = V_{C(0)} \Omega_L / k A_C R_d \qquad \text{(IV.16h)}$$

$$\Lambda_{16} = \Omega_L / k \qquad \text{(IV.16i)}$$

$$\Lambda_{17} = \beta_3 \; V_t \qquad \text{(IV.16j)}$$

IV.3.b Link Between Pneumatic and Mechanical Sections

The gyrator shown in Fig. IV.9 corresponds in hardware to the cylinder-cam-actuator combination. It transforms the pressure force on the piston into a torque that acts on the motor shaft. Since there are losses involved in the transformation, the gyrator in the above figure is not an ideal one. The instantaneous torque T_M is a function of both the instantaneous pressure P_d in the cylinder and the angular displacement of the output shaft. Since one side of the piston is vented to atmosphere, the net pressure acting

on the piston is given by

$$P_C = P_d - P_{atm} \tag{IV.17a}$$

The torque output from the gyrator is given by Eq. IV.12, which, when nondimensionalized, becomes:

$$T_M^* = \frac{\Gamma}{1 + \frac{\mu_2}{S^*}(2r^* - 2 + S^*)} \cdot \frac{dr^*/d\theta_1^* - \mu_1 \alpha_s r^*}{\alpha_s r^* + \mu_1 dr^*/d\theta^*} \tag{IV.17b}$$

where

$$\Gamma = (p_C A_C - K_s r - f_C) r / P_s A_C R_d \geq 0 \tag{IV.17c}$$

and

$$f_C = f_{CS} \qquad dr/dt = 0$$

$$= f_{CD} \qquad dr/dt \neq 0$$

f_{CS} and f_{CD} are the values of f_C corresponding to the rolling and sliding, respectively, of the piston O-ring seal. The rolling of the seal occurs at the beginning of piston motion, whereas the sliding motion of the O-ring occurs when it reaches the end of its groove. The values of μ_1 and μ_2 used in Eq. IV.17b are the dynamic values of the friction between the actuator and cam and the actuator and its guide respectively. This is due to the presence of clearances which allow the actuator to be already in motion when it touches the cam and starts producing torque.

IV.3.c Analysis of the Mechanical Section

In the mechanical section shown in Fig. IV.9, μ_3 and μ_4 represent the frictional losses in the O-ring rotary seal on the motor shaft and in the friction brake of the load. The frictional torque of the O-ring rotary seal is constant for a given system. The torque transducer rotary element has negligible inertia in comparison with either the motor inertia or the load inertia. Thus, referring to Fig. IV.9, and proceeding from left to right, the equations describing the mechanical section are as follows:

Motor:

The equation for the motor according to the linear graph is given by

$$T_M = J_M \frac{d^2\theta_1}{dt^2} + K_M(\theta_1 - \theta_2) + T_{FM}$$

where

$$T_{FM} = f(\mu_3)$$

Rearranging and nondimensionalizing the above equation yields:

$$\frac{d^2\theta_1^*}{d\tau^2} = \Lambda_{18}(T_M^* - T_{FM}^*) - \Lambda_{19}(\theta_1^* - \theta_2^*) \qquad \text{(IV.18a)}$$

In practice, a certain amount of backlash between the actuator and its guide is inevitable, and has to be accounted for in the equations. Figure IV.10 shows, in exaggerated form, a schematic diagram of the actuator and

its guide, during the stepping action (Fig. IV.10a), and at the end of the step (Fig. IV.10b). Referring to Fig. IV.10a, while the actuator is following the driving profile, it is always subject to the positive driving torque T_M, while the cylinder housing is subject to the negative torques

$$J_M \frac{d^2\theta_1}{dt^2} \; ; \; K_M(\theta_1 - \theta_2) \; , \text{ and } T_{FM}$$

The effect of this torque distribution is shown in Fig. IV.10a, where the actuator always assumes the position shown, which is the zero backlash position. Therefore, the angular velocity of the cylinder housing, and hence of the output shaft, is the same as that of the actuator and is given by:

$$\frac{d\theta_1^*}{d\tau} = \int_0^{\tau_f} [\frac{d^2\theta_1^*}{d\tau^2}]d\tau \qquad \text{(IV.18b.1)}$$

However, at the end of the step, when the actuator is locked in position, the cylinder housing can oscillate as part of the moving system, but only within the bounds of the backlash given by

$$1 \leq \theta_1^* \leq 1 + \eta^*$$

where η^* is the nondimensional backlash angle. Figure IV.10b shows the actuator positions at zero backlash ($\theta_1^* = 1$, solid line) and at maximum backlash ($\theta_1^* = 1 + \eta^*$, dashed line). The angular velocity of the cylinder housing within the backlash region is hence given by:

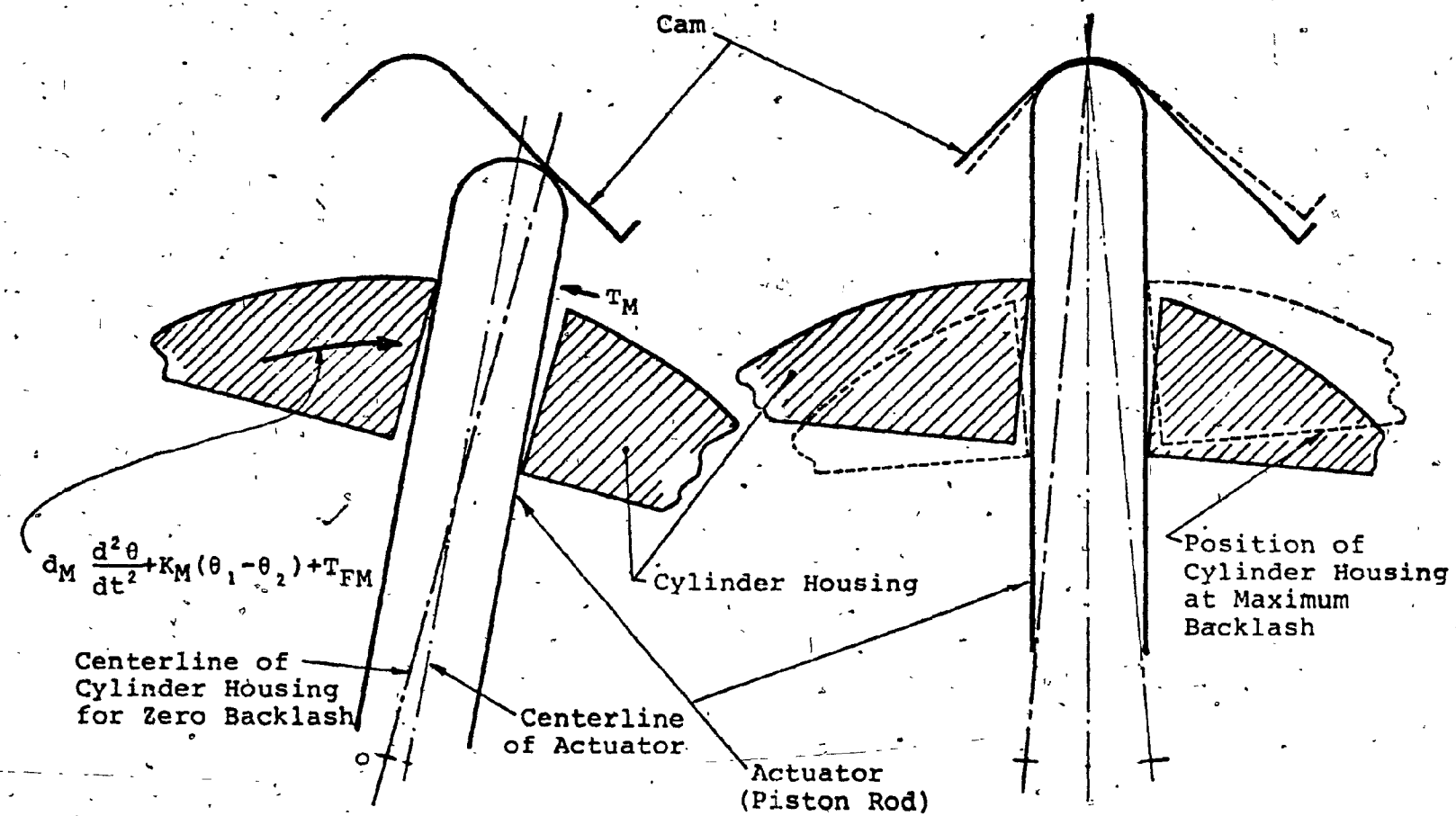

Fig. IV.10a: Position of Zero Backlash

Fig. IV.10b: The Actuator and Its Guide at the End of the Step

Fig. IV.10: Schematic Diagram Showing Backlash Between Actuator and Guide.

$$\frac{d\theta_1^*}{d\tau} = \int_0^{\tau_f} [\frac{d^2\theta_1^*}{d\tau^2}]d\tau ; \; 1 \leq \theta_1^* \leq 1 + \eta^* \qquad \text{(IV.18b.2)}$$

when the cylinder housing hits the actuator, it comes to an instant stop, and the velocity is given by

$$\frac{d\theta_1^*}{d\tau} = 0 \; ; \; 1 > \theta_1^* > 1 + \eta^* \qquad \text{(IV.18b.3)}$$

Torque Transducer:

Since the torque transducer has negligible inertia, its characteristics are similar to those of a lossless torsional spring. Thus,

$$K_M(\theta_1 - \theta_2) = K_T(\theta_2 - \theta_3)$$
$$= K_L(\theta_3 - \theta_4)$$

In nondimensional form the torque transducer equation becomes

$$K_M^*(\theta_1^* - \theta_2^*) = K_T^*(\theta_2^* - \theta_3^*)$$
$$= K_L^*(\theta_3^* - \theta_4^*) \qquad \text{(IV.18c)}$$

Load:

The load equation according to Fig. IV.9 is given by:

$$K_L(\theta_3 - \theta_4) - J_L \frac{d^2\theta_4}{dt^2} - T_{FB} = 0$$

The torque T_{FB} is given in Appendix G as

$$T_{FB} = K_1 \cdot F_B \cdot \mu_4$$

where μ_4 can vary exponentially between the static value $\mu_{4(s)}$ and the dynamic value $\mu_{4(d)}$ [Appendix G]. Thus,

$$\mu_4(s) \geq \mu_4(s) \cdot e^{-K_2 \cdot |d\theta_4/dt|} \geq \mu_4(d)$$

Rearranging and nondimensionalizing, the load equation becomes:

$$\frac{d^2\theta_4^*}{d\tau^2} = \Lambda_{20}(\theta_3^* - \theta_4^*) - \Lambda_{21} T_{FB}^* \qquad \text{(IV.18d)}$$

In the mechanical section, the nondimensional constants Λ_{18} through Λ_{21} are given by:

$$\Lambda_{18} = (P_S A_C R_d)/(\alpha_S J_M \Omega_L^2) \qquad \text{(IV.18e)}$$

$$\Lambda_{19} = (\Omega_M/\Omega_L)^2 \qquad \text{(IV.18f)}$$

$$\Lambda_{20} = K_L^* \qquad \text{(IV.18g)}$$

$$\Lambda_{21} = (P_S A_C R_d)/(\alpha_S K_E) \qquad \text{(IV.18h)}$$

Equation IV.18 completes the set of simultaneous equations, describing the entire system. Equations IV.13 through IV.18 must be solved to complete the analysis. Since an analytical solution of these equations would be extremely complex, a numerical technique based on the fourth-order Runge-Kutta integration method was implemented using MIMIC. The computer listing together with the different parameters used in the calculations are given in Appendix H. The theoretical results will be presented in Chapter V, and compared with the experimental results obtained from the prototype system. The experimental results are also given in Appendix H.

CHAPTER V

THEORETICAL AND EXPERIMENTAL RESULTS

V.1 Theoretical and Experimental Stall Torque Function Comparisons

As mentioned in Section IV.2, the stall torque function Ξ provides a measure of the effectiveness of torque conversion in the motor. The function was also used as a basis for the comparisons between the theoretical and experimental results. The experimental results were obtained by indexing the motor output shaft to the desired angle at which the stall torque was to be measured (with supply pressure disconnected). The shaft was then physically locked in that position by applying a sufficient number of weights on the brake arm. The supply pressure was then applied, and the torque transducer output recorded on the oscilloscope. The stall torque thus measured was then substituted into Eq. IV.12c to obtain the stall torque function Ξ. The theoretical value for Ξ was also obtained from Eq. IV.12c but with the calculated T_{st} being used. In the calculation of T_{st} the static values for the friction coefficient between the cam and actuator, and actuator and its guide (μ_1 and μ_2, respectively) were used.

Figure V.1 shows a comparison of the theoretical and experimental stall torque function versus the angular displacement, within a single step of the prototype motor.

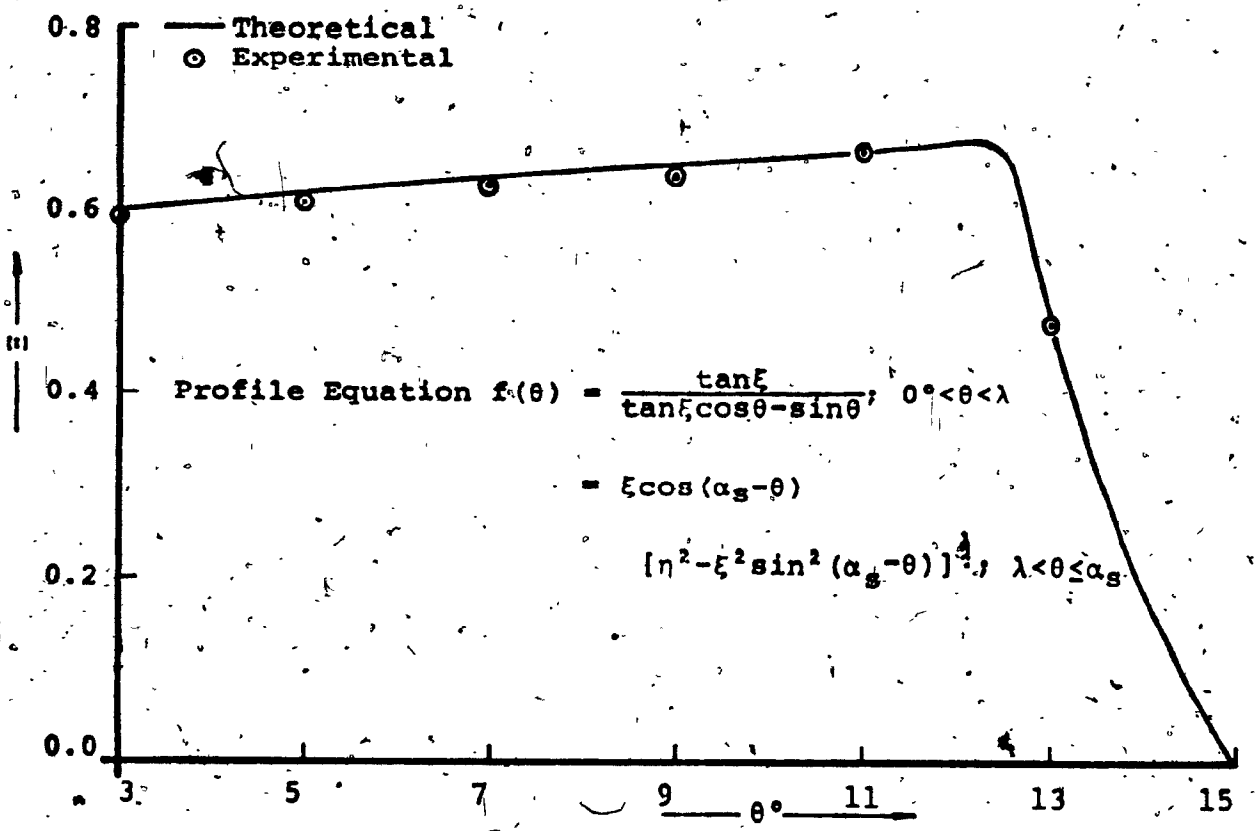

Fig. V.1: Comparison of Theoretical and Experimental Stall Torque Functions.

The theoretical stall torque function Ξ is seen to compare very favourably with the experimental measurements in the above figure. The value of Ξ is observed to increase slightly with an increase in angular displacement for the straight line part of the driving profile (until $\theta = 12.5°$). For the remainder of the driving profile (i.e. the circular part) Ξ decreases rapidly to zero. The actuator tip then comes to rest snugly at the bottom of the profile, thus providing a positive lock at the end of the step which is a major favourable feature of this motor.

V.2 Comparison of the Dynamic Theoretical and Experimental Results and Discussion

Figure V.2 shows a comparison between the theoretical and experimental dynamic torque T_T ($T_T = K_T(\theta_2 - \theta_3)$) transmitted between the motor and the load. The curves in the above figure have been replotted from one of the experimental oscilloscope traces and the corresponding theoretical computer output plot, to serve as an illustration of the correlation obtained. The theoretical results are observed to correlate with the experimental data to within 10%. This suggests that the equations of Chapter IV are sufficient to describe the prototype system.

In order to aid the explanation of the nature of the traces in Fig. V.2, it is necessary to give a description of the sequence of movements of the different mechanical

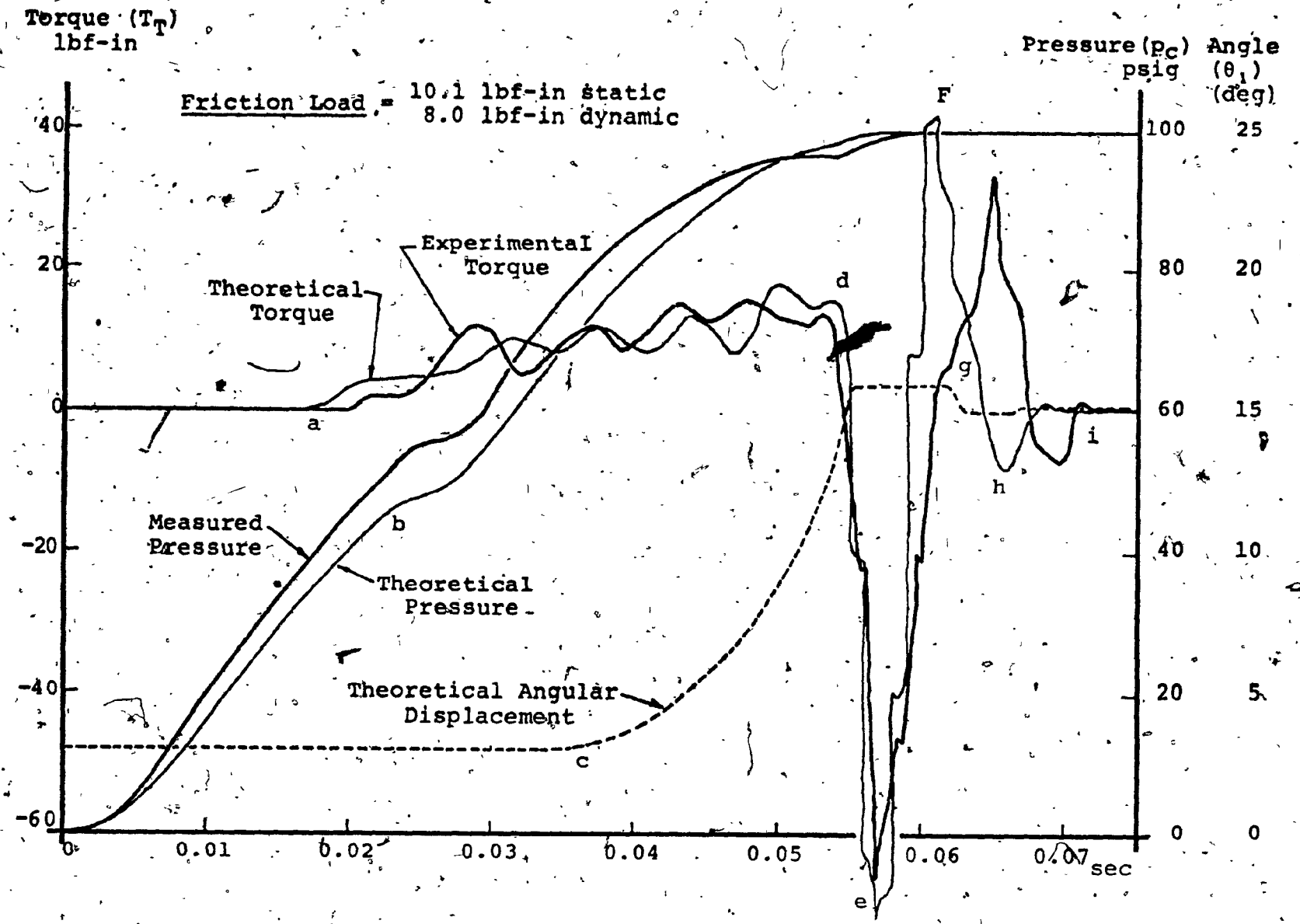

Fig. V.2: Comparison Between Theoretical and Experimental Dynamic Torque.

system parts. This description is best carried out with the aid of the simple mechanical system of Fig. V.3, which is analogous to the motor-load system. In Fig. V.3, M_1 and M_2 represent the cylinder housing and load masses respectively. The two masses are joined together as shown in the figure, by a single shaft which represents the combination of motor, torque transducer, and load shafts. The single actuator shown is located in a gap in the periphery of the disc-shaped 'cylinder-housing' mass, and the actuator-gap combination represents the backlash in an exaggerated manner. Referring to Fig. V.3, and the theoretical curve in Fig. V.2, the following sequence of events occurs. (In the ensuing description a twisting of the shaft in the positive sense implies that the motor is driving the load in the positive direction or that the load is driving the motor in the negative direction, and vice versa).

1.- (Ref. Fig. V.3): The continuously increasing torque T_M (due to cylinder pressure rise) initially forces the actuator to push against the cylinder housing at point (I), thereby moving the latter in the positive direction shown. A part of this torque is utilized in overcoming both the inertia of the housing and the output shaft seal friction, while the remainder twists the shaft in the positive sense.

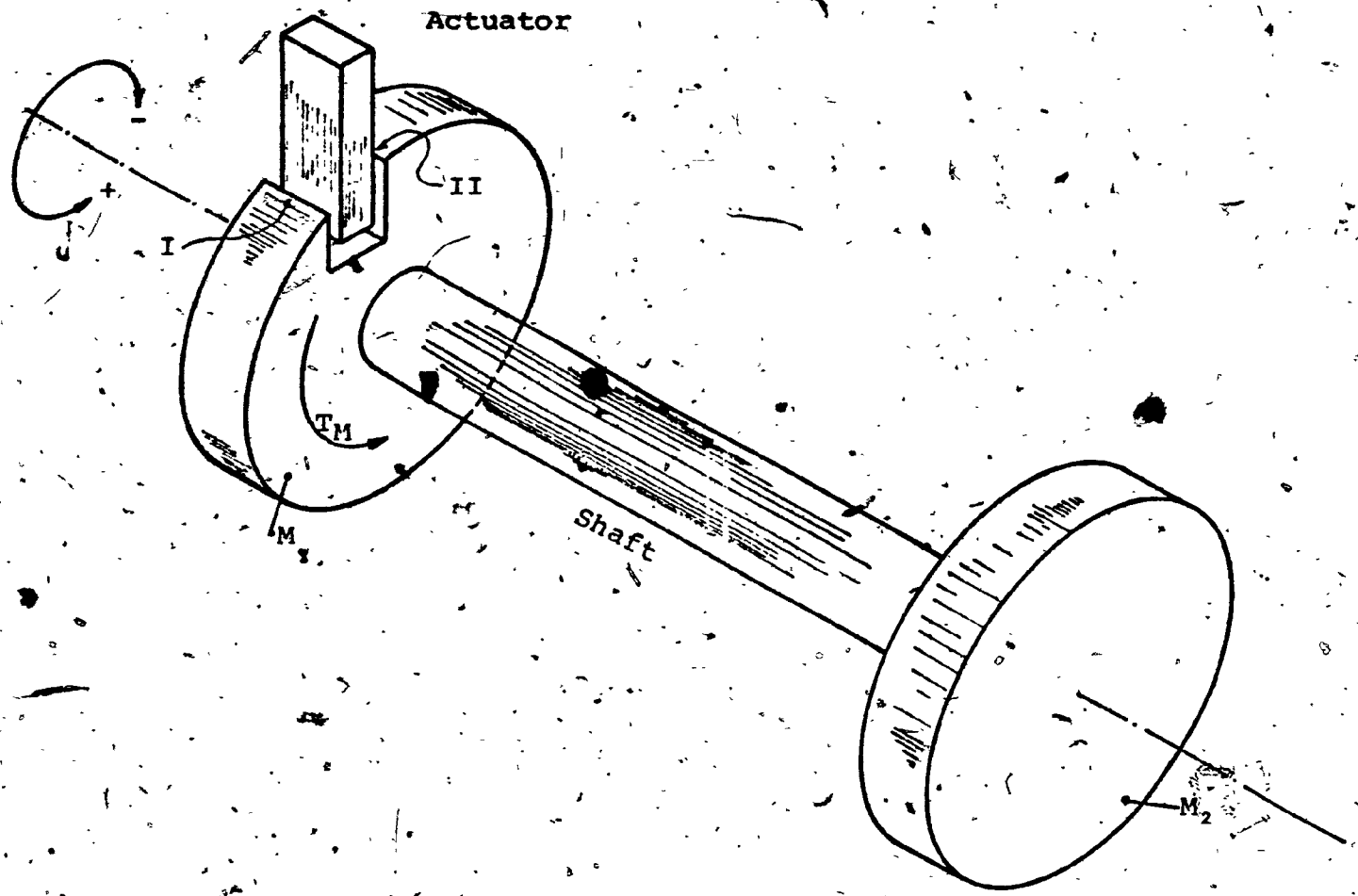

Fig. V.3: Simple Mechanical Analogy of the System.

(Ref. Fig. V.2): The start of the above twisting of the shaft is indicated by the point (a).

2.- (Ref. Fig. V.3): The twist in the shaft is transmitted to the load end in the form of a torque, and a further increase in T_M increases the torque applied to the load. Once the latter torque exceeds the limiting static friction torque of the load (i.e. 'breakaway') the load-cylinder housing system starts to accelerate rapidly in the positive direction shown.

(Ref. Fig. V.2): At 'breakaway', the ensuing high rate of volume change within the cylinder causes a plateau in the pressure-time trace, indicated by point (b). The slope of the pressure-time trace following the point (b) assumes nearly its initial value (before the plateau), owing to the relatively slower rate of volume change within the cylinder after 'breakaway'. The very short time duration of the 'breakaway' as well as the relatively slow increase in piston velocity following it, results in the theoretical angular displacement curve being almost flat up to the point (c). After point (c), the angular displacement rises rapidly as a consequence of the increasing piston velocity. The latter increase also results in a corresponding reduction in the rate of pressure rise until the end of the step.

3.- (Ref. Fig. V.3): As a result of the 'breakaway', the system (M_1-shaft-M_2) is excited and begins to oscillate in its forward motion until it reaches the end of the step.

(Ref. Fig. V.2): The oscillations are shown between points (a) and (d) (end of step, $\theta_1 = 15°$) on the torque trace. The sudden rise in the pressure trace at the end of the step is caused by the piston reaching its stop, thus making the cylinder volume constant once again.

4.- (Ref. Fig. V.3): At the end of the step, the actuator is locked in position. The load and the cylinder housing continue to move due to their inertia, until the cylinder housing collides with the actuator at point (II), thus bringing the cylinder housing to a sudden stop. This position, which is the maximum angular displacement, also corresponds to maximum backlash. The load, however, continues to move in the positive direction due to its inertia, first to unwind the remaining twist in the shaft, and then to twist the shaft in the negative sense.

(Ref. Fig. V.2): As a result of the negative twist of the shaft, a negative torque is recorded by the torque transducer, as indicated by the torque trace after point (d). The load motion continues at a decaying

rate (due to the frictional losses) until it reaches the maximum negative displacement at point (e) on the torque trace. The negative twist in the shaft is maximum at this point.

5.- (Ref. Fig. V.3): As a result of the negative twist, the load starts to accelerate in the negative direction, unwinds the shaft twist, then overshoots the neutral position, and twists the shaft in the positive direction once more to reach a maximum displacement.

(Ref. Fig. V.2): The corresponding maximum positive torque is shown at point (f).

6.- (Ref. Fig. V.3): The torque imposed by the load through the shaft tends to move the cylinder housing towards point (I) (i.e., the position of zero backlash). However, when contact of the actuator with point I is made, the load has already reached maximum negative displacement and is returning in the positive direction.

(Ref. Fig. V.2): Due to the finite time required for velocity build-up, the load succeeds in bringing the cylinder housing to the zero backlash position only at point (g), on the decreasing torque signal trace.

7.- (Ref. Fig. V.3): Once again the load overshoots the neutral position, and reaches a maximum positive displacement.

(Ref. Fig. V.2): The corresponding maximum negative torque is indicated by point (h). The torque trace is seen to decay rapidly after the end of the step to reach zero at point (i). This rapid decay, which is caused by the load friction and the shaft seal friction, effectively constitutes a damping factor at the end of the step.

The above description shows that the present type of motor is more suited to loads that are more resistive than inertive. If inertial loading predominates, however, external damping will have to be employed.

Figure V.4 shows the time variation of the theoretical nondimensional rotary junction pressure p_C^*, angular displacement θ_1^*, and the torque transducer output T_T^* $[T_T^* = K_T^* (\theta_2^* - \theta_3^*)]$, under different frictional loadings.

The dynamic torque traces in the figure show that the torque always starts rising at exactly the same value of $\tau (\tau = 15)$, irrespective of the load on the motor. This is to be expected since the point at which the torque begins to rise is the point at which the developed torque T_M^* just exceeds the output shaft-seal friction, the latter being constant for a given motor. The developed torque T_M^* is unaffected by the load up to this point.

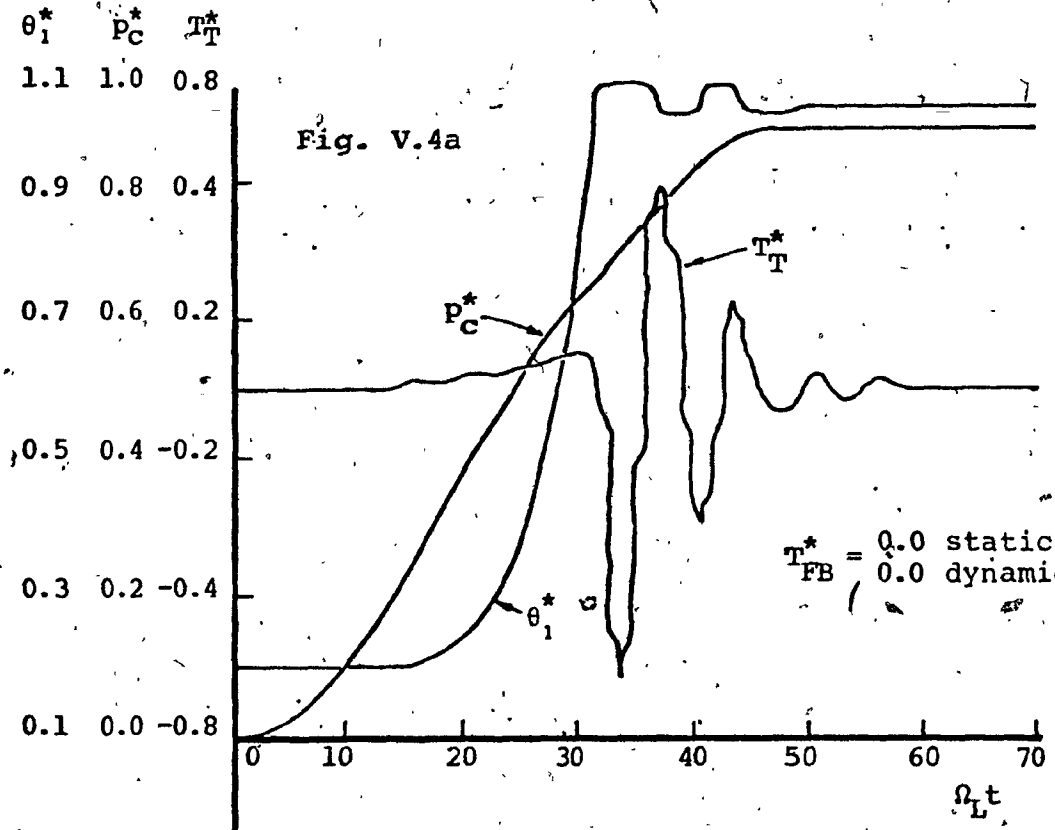

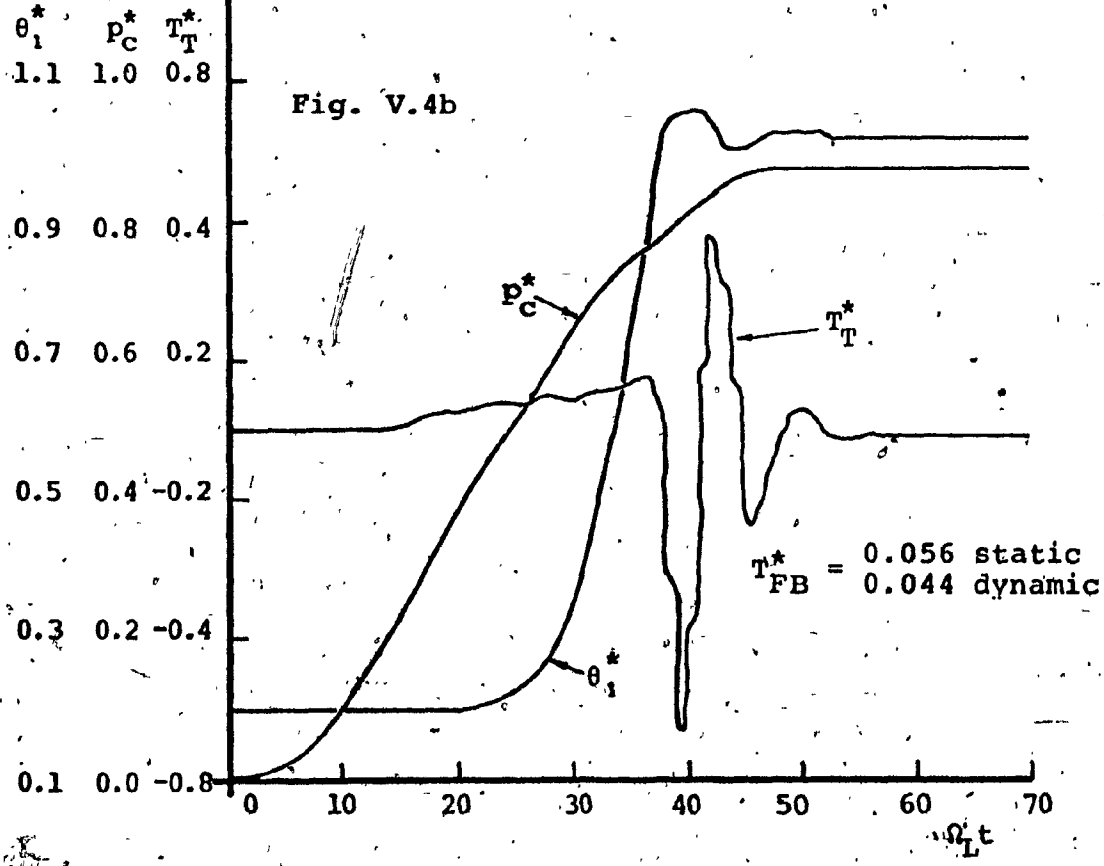

Fig. V.4a-V.4d: Theoretical Dynamic Behavior of the Motor Under Varying Loads (Contn'd).

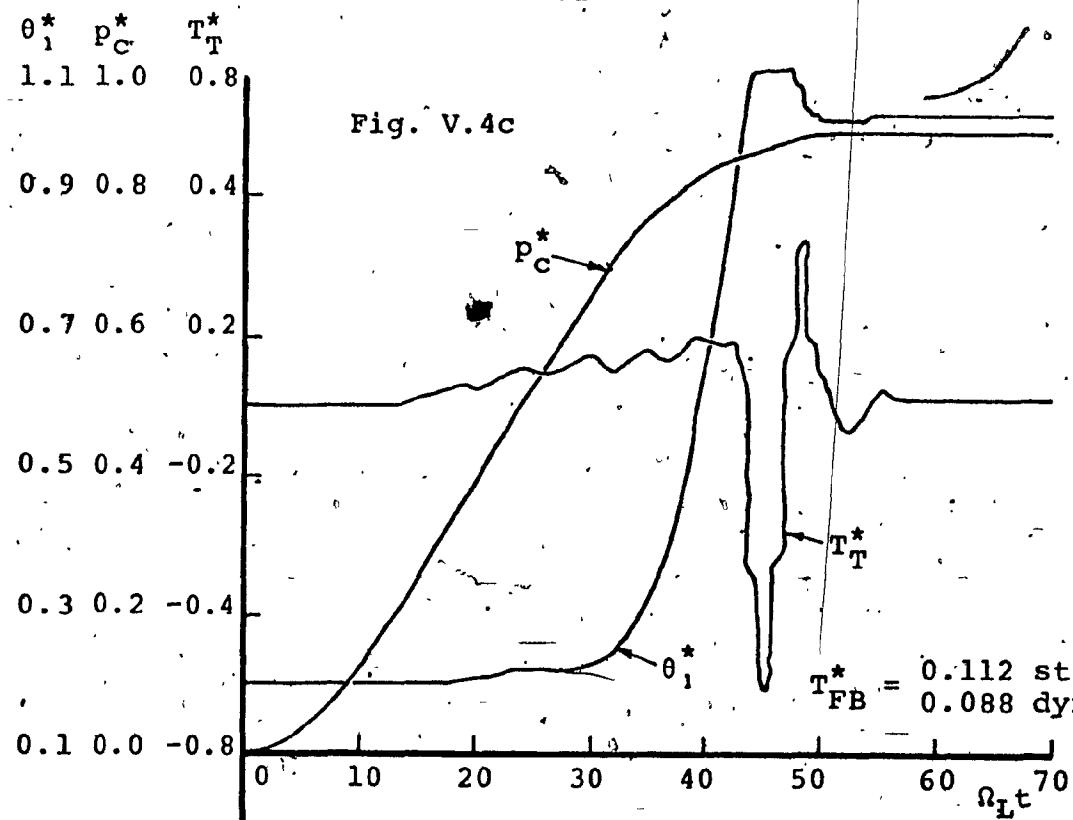

Fig. V.4c

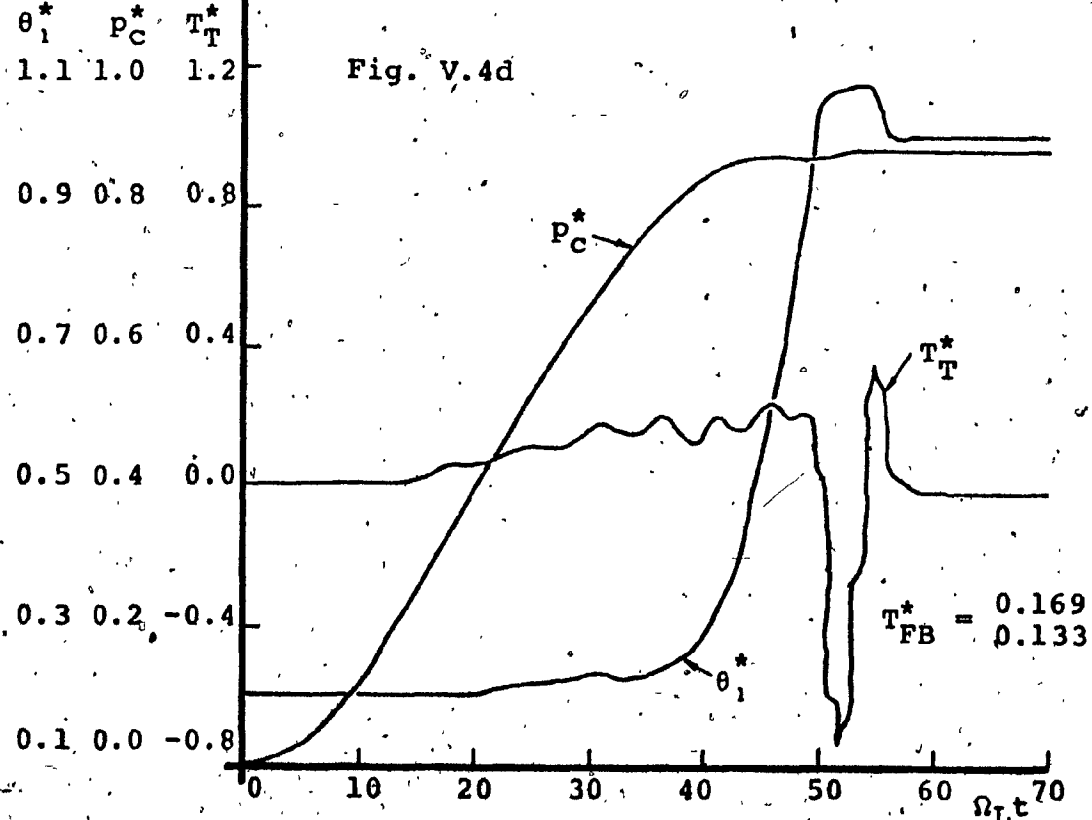

Fig. V.4d

Fig. V.4a-V.4d: Theoretical Dynamic Behavior of the Motor Under Varying Loads (Contn'd).

Throughout the stepping time, for $\theta_1^* < \alpha_s^*$, the torque traces of Fig. V.4 are oscillatory, with a period of approximately $5/\Omega_L$, corresponding to a frequency of about 160 Hz. Although the oscillation frequency does not change appreciably with the loading, its amplitude increases with an increase in the load. This frequency, which can be regarded as a combined "damped" natural frequency of the motor-load system, is 1.66 times higher than the frequency of oscillations of the load alone, measured when the cylinder housing is stationary at the end of the step. Based on the formulae given in Ref. 18, the ratio between the "undamped" natural frequency of the whole system and that of the load alone is found to be 2.24. The measured ratio between the "damped" frequencies is within 30% of the ratio calculated for the "undamped" frequencies.

From Figs. V.4 and V.1, it can be deduced that the maximum dynamic torque and the maximum stall torque both occur at $\theta_1^* = 0.833$ ($\theta = 12.5°$) within a step, thereby showing that both these maximum torques are controlled by the cam geometry.

Figure V.5 shows a replot of some of the parameters of Fig. V.4 versus the load frictional torque, at $\theta_1^* = 0.833$. The above figure has three plots: a) the maximum torque T_T^* during the step, b) the pressure p_C^* at the rotary junction, and c) the time required to reach $\theta_1^* = 0.833$.

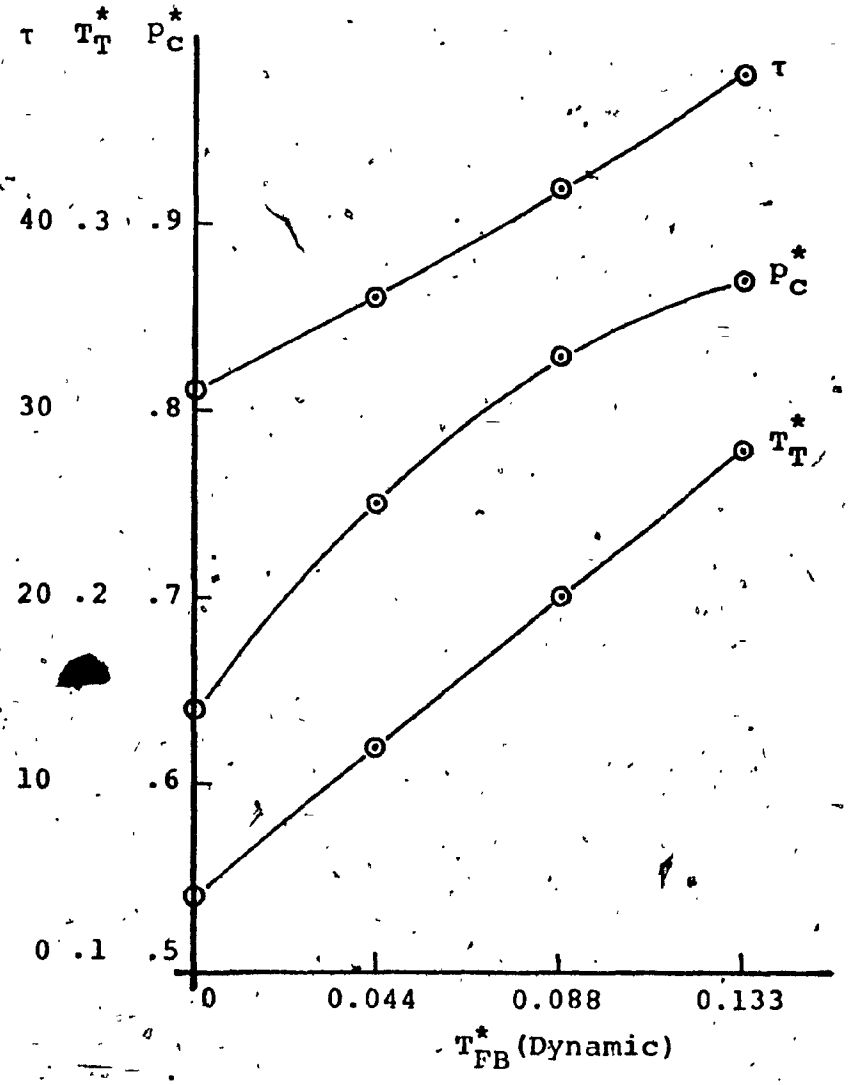

Fig. V.5: Plot of τ, p_C^*, and T_T^* Versus T_{FB}^* at $\theta_1^* = 0.833$ (Taken from Fig. V.4).

In Fig. V.4, the torque transmitted increases with the loading, because successively increasing torque magnitudes are required in order to overcome any increased frictional load. This is also evident in the maximum torque variation shown in Fig. V.5. In addition, the latter figure shows that an increase in load results in an increase in the time required to reach a given displacement, thus allowing a longer time interval for the charging of the cylinder. This, in turn, results in a higher torque being developed.

After the end of the step is reached at $\theta_1^* > \alpha_s^*$, the oscillations correspond to that of a system consisting of an unconstrained load at one end, and a rotor constrained by backlash at the other. In the above region, the oscillations tend to become damped as the frictional load increases. Figure V.6 shows the variation, with loading, of the pertinent time parameters involved with the traces of Fig. V.4.

In Fig. V.6, the curve (c), which is the sum of the other two curves in the figure, shows that the complete time interval measured from the application of air pressure to the final settling down of the rotor is nearly independent of the load friction (e.g. the time varies from 62 at $T_{FB}^* = 0$, to 65 at $T_{FB}^* = 0.133$).

In addition to the above, Figure V.4 shows that the time taken to complete one step increases with an increase in the load inertia (i.e.: small Ω_L).

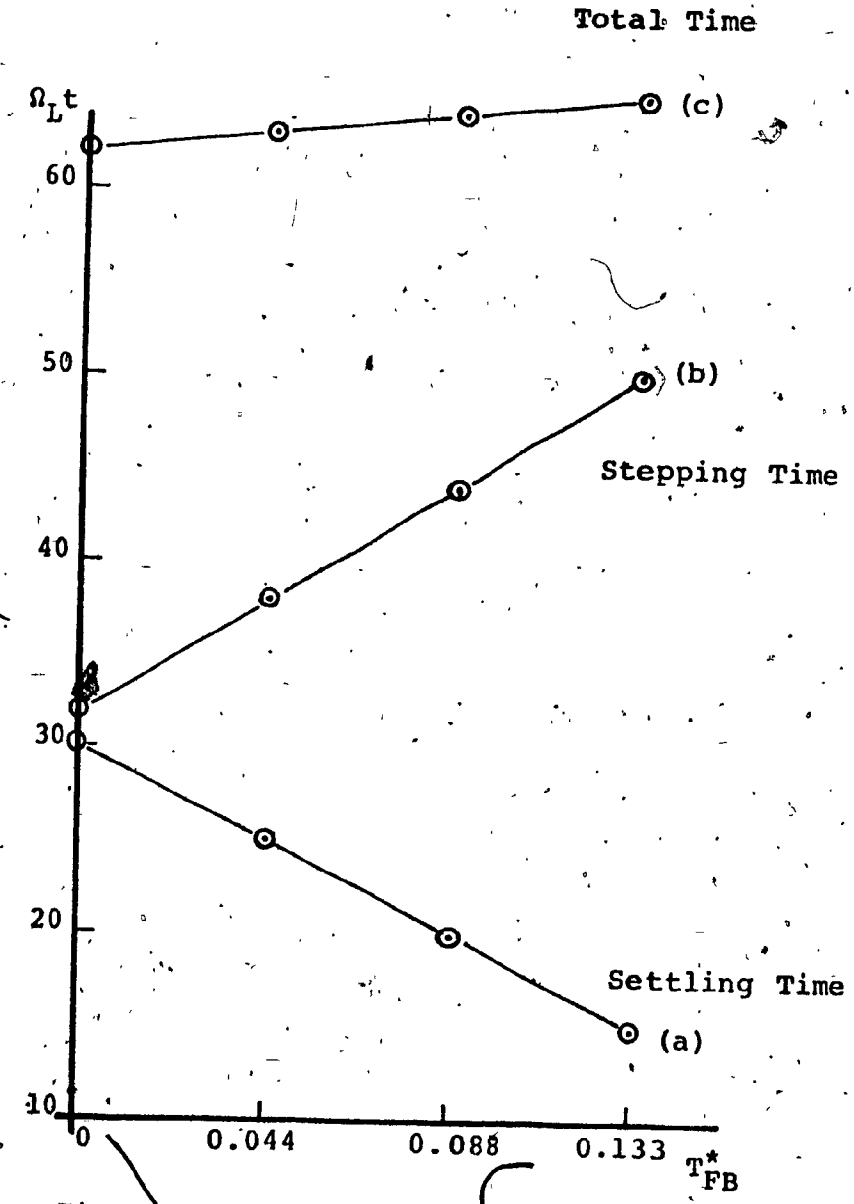

Fig. V.6: Variation of Time Parameters with Loading (Taken from Fig.V.4).

CHAPTER VI

DESIGN PROCEDURE

In this chapter, a general design procedure for the prototype motor will be presented. The procedure does not imply that the particular mechanical layout used in the prototype would have to be followed in any given design. The design procedure outlined here is based on the assumption that the driving profile on the cam is similar to that utilized in the prototype motor (i.e. straight line profile with circular end).

There are three major operating parameters that the designer must know before proceeding with the design. These are: the stall torque to be developed by the motor; the operating (supply) pressure; and the angle of resolution (the step angle). The latter however, has to be chosen from among those angles that can be expressed by Eq. IV.2 in Chapter IV. The designer must also have estimates of the approximate size of the motor, and of μ_1 and μ_2, the latter being determined by the choice of materials for the cam, the actuator, and the cylinder housing.

In the procedure, the driving profile is initially approximated by a straight line profile as shown in Fig. VI.1, and is latter modified into the actual profile. In such an approximation, the tooth depth remains unchanged while the

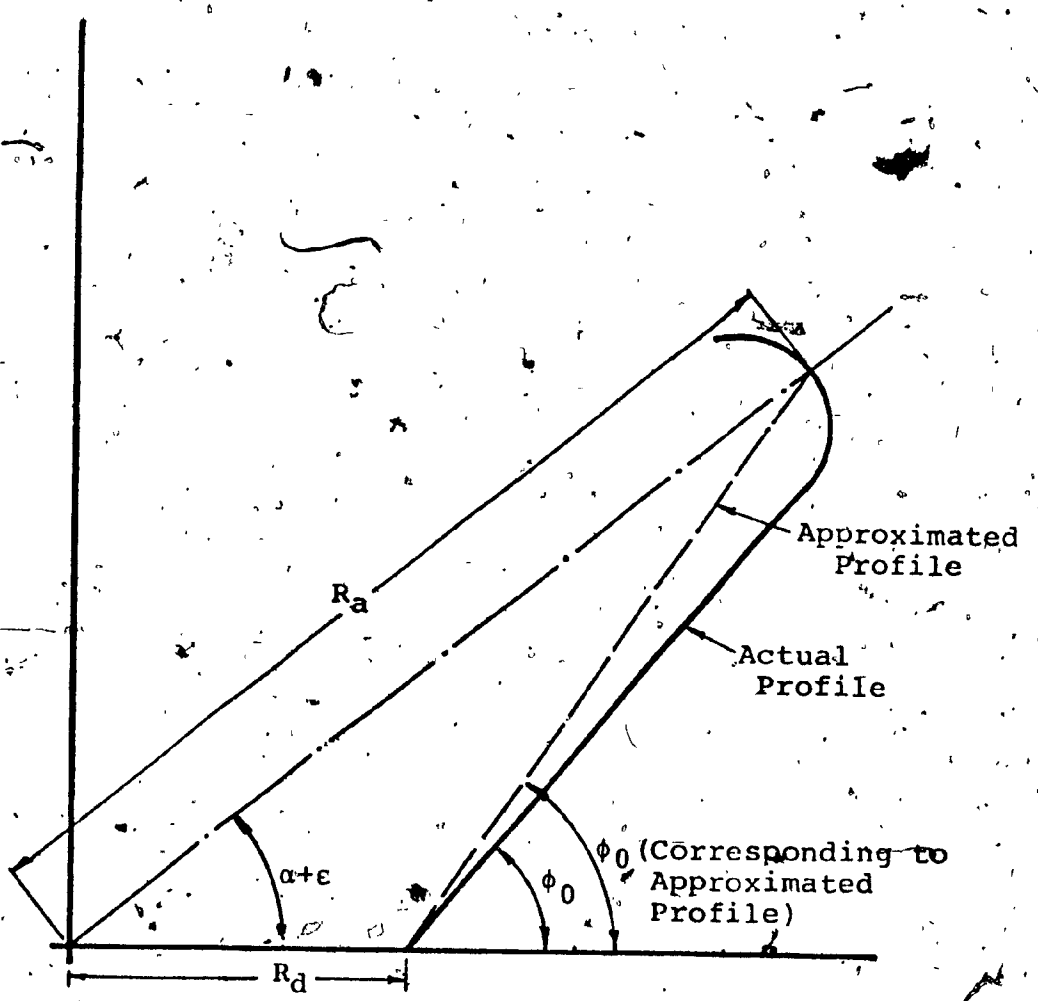

Fig. VI.1: Driving Profile and Its Straight Line Approximation.

angle of attack is increased. Referring to Fig. VI.1, the approximate relation between the cam radii R_a and R_d and the initial angle of attack ϕ_0 is given by:

$$R_d = \frac{R_a \sin(\phi_0 - \alpha - \varepsilon)}{\sin \phi_0} \qquad \text{(VI.1)}$$

The equation of the stall torque $T_{st(0)}$ at the beginning of the step is arrived at by combining Eq. IV.9 and Eq. C[20 [Appendix C], and substituting the values of p_C, r, and ϕ at the beginning of the step (P_s, R_d, and ϕ_0 respectively) in the combined equation. Thus,

$$T_{st(0)} = \frac{[(P_s A_C - (K_S R_d + f_{CS})] R_d}{1 + \mu_2} \cdot \cot(\phi_0 + \psi_1)$$

In the above equation, the term $(K_S R_d + f_{CS})$ represents the contributions of the cylinder return spring, and the friction of the piston seal towards the piston force. The magnitude of this term is usually negligible in comparison with the supply pressure force $P_s A_C$. In the prototype for example, the percentage contribution of $(K_S R_d + f_{CS})$ to the piston force is about 6% at 100 psig supply pressure. Thus, the above term may be neglected and the stall torque equation written as follows:

$$\frac{T_{st(0)}}{P_s} = \frac{A_C R_d}{1 + \mu_2} \cot(\phi_0 + \psi_1) \qquad \text{(VI.2a)}$$

The quantity given by Eq. IV.2 is called the torque-pressure ratio Σ

$$\Sigma = \frac{T_{st(0)}}{P_s} \quad , \qquad \text{(VI.2b)}$$

The design procedure is simplified through the use of two sets of design graphs shown in Figs. VI.2 and VI.3. The composite graph of Fig. VI.2 forms the solution of Eq. VI.2b. The plots in the different quadrants of Fig. VI.2 are as follows:

Quadrant I : Σ versus Σ_1 [$\Sigma_1 = A_C R_d \cot(\phi_0+\psi_1)$] for different μ_2

Quadrant II : Σ_1 versus Σ_2 [$\Sigma_2 = A_C \cot(\phi_0+\psi_1)$] for different R_d

Quadrant III : Σ_2 versus Σ_3 [$\Sigma_3 = \cot(\phi_0+\psi_r)$] for different A_C

Quadrant IV : Σ_3 versus ϕ_0 for different ψ_r.

Figure VI.3 shows the graphic solution of Eq. VI.1, together with replots of Fig. IV.3 and Fig. IV.5 for easy reference. The plots in the different quadrants of Fig. VI.3 are as follows:

Quadrant I : R_d versus R_d' [$R_d' = R_d \sin\phi_0$] for different ϕ_0

Quadrant II : R_d' versus R_a for different $(\phi_0 - \alpha + \varepsilon)$

Quadrant III : ϕ_0 versus ε for different R_t^*

Quadrant IV : R_a^* versus A_C^* for different H^*

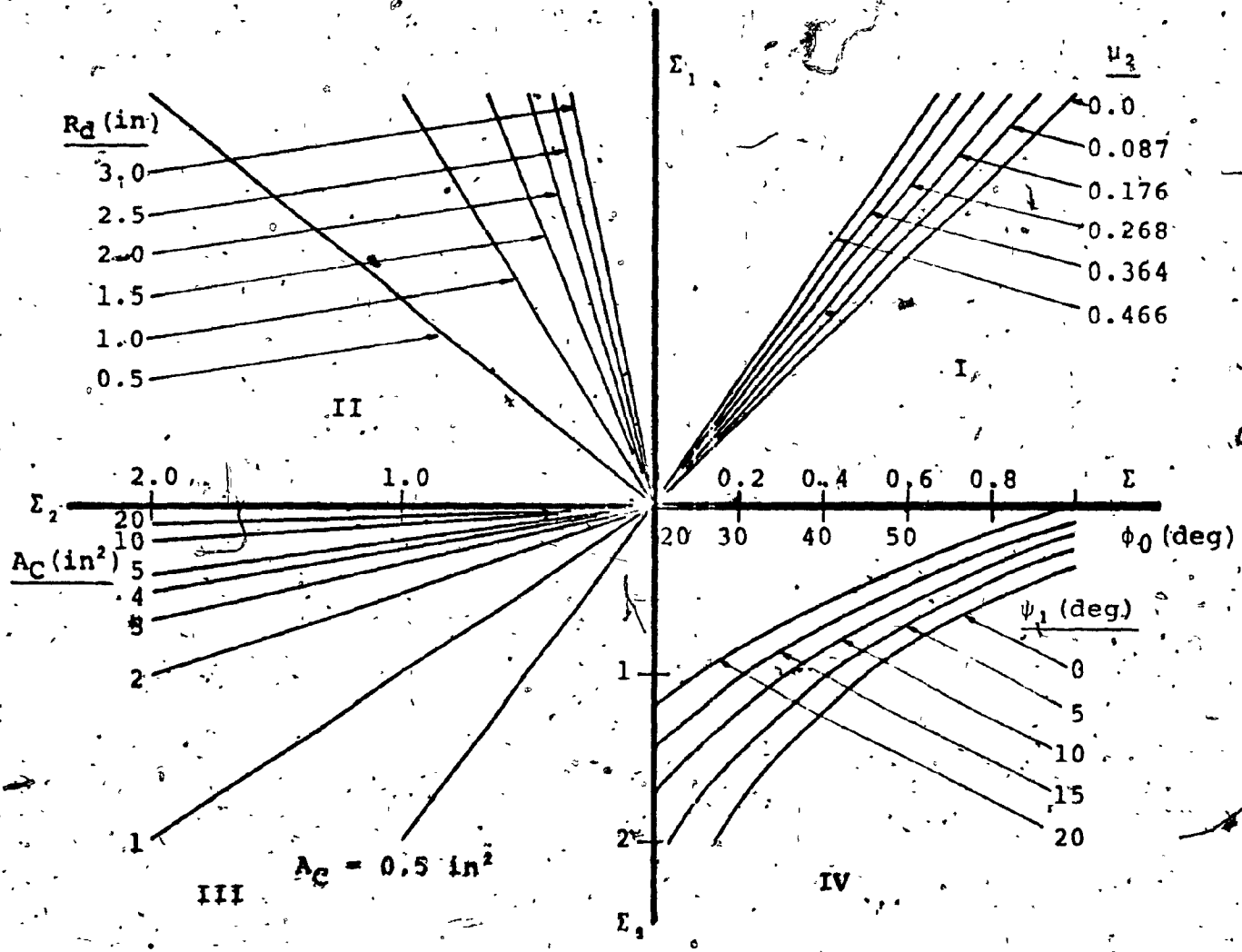

Fig. VI.2: Graphic Solution of the Starting Torque Equation.

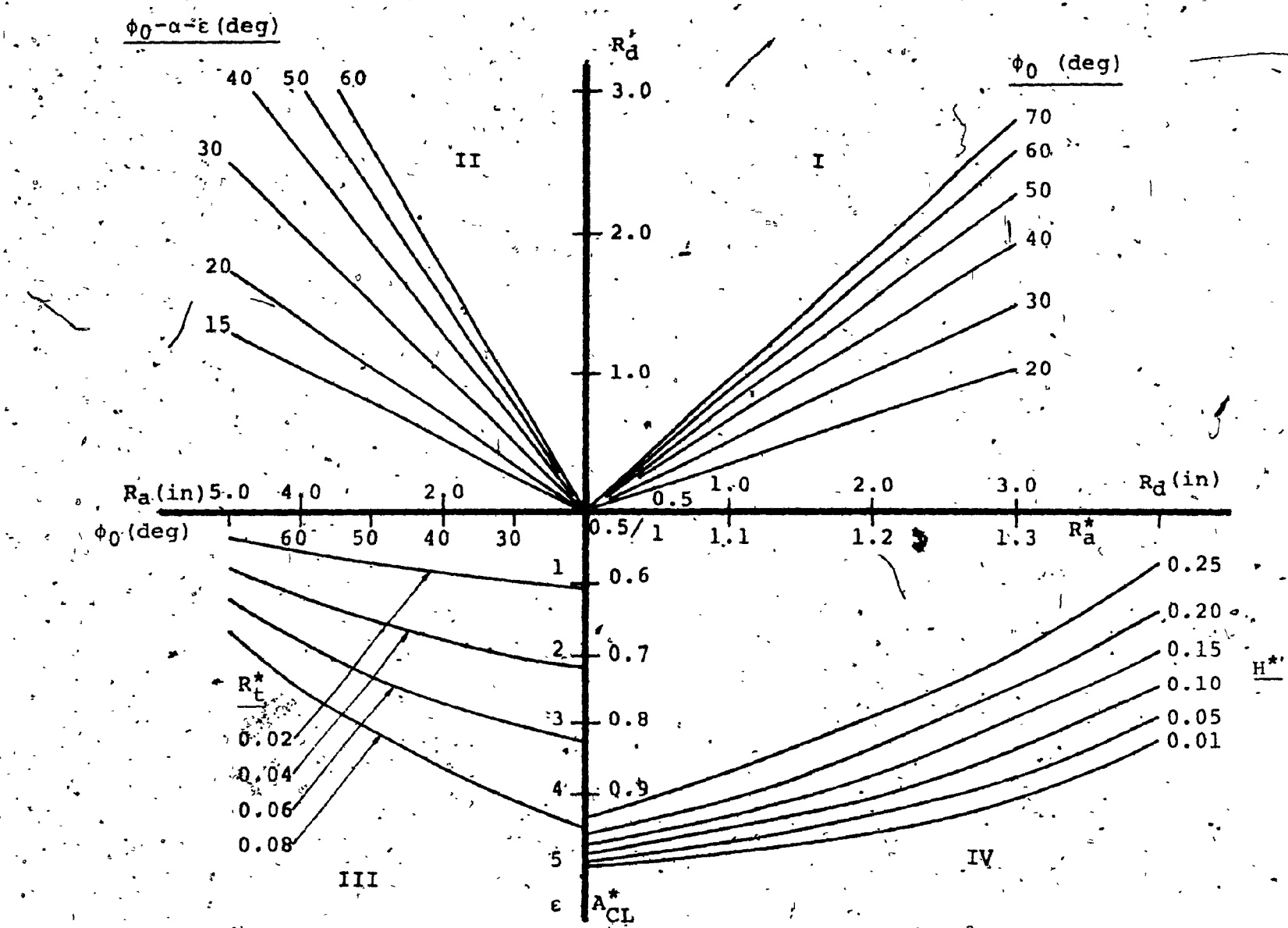

Fig. VI.3: Graphic Solution of the Geometric Equations.

The steps of the design procedure are now as follows:

1- With the required stall torque and the operating pressure known, calculate the torque-pressure ratio Σ.

2- From Quadrant I, Fig. VI.2, find Σ_1 for the coefficient of friction μ_2 between the materials of the actuator and the cylinder housing.

3- As a first approximation, evaluate the dedendum radius of the cam R_d, judging by the estimated size of the motor. Use Quadrant II, Fig. VI.2 to find Σ_2.

4- Estimate the value of H (piston height plus half the separator plate thickness). Assuming $R_a = R_d$ (i.e. $R_a^* = 1$), use Quadrant IV, Fig. VI.3 to find the area A_{CL} of the largest cylinder that can be housed within the cam ($A_{CL} = \pi R_d A_{CL}^*$).

5- Choose a cylinder area A_C below the value of A_{CL}, then find Σ_3 from Quadrant III, Fig. VI.2.

6- Find the initial angle of attack ϕ_0 from Quadrant IV, Fig. VI.2 corresponding to the friction angle ψ_1 between the material of the cam and the actuator.

7- Choose the value of the actuator tip radius R_t, calculate R_t^* ($R_t^* = R_t/R_d$), then use Quadrant III, Fig. VI.3 to obtain the offset angle ε.

8- For the dedendum radius R_d and the initial angle of attack ϕ_0, find R_d' using Quadrant I, Fig. VI.3.

9- Calculate the value of $(\phi_0 - \alpha + \varepsilon)$, then find R_a from Quadrant II, Fig. VI.3.

10- Calculate R_a^* and H^* then find A_{CL}^* from Quadrant IV, Fig. VI.3, calculate A_{CL}.

11- The value of A_{CL} calculated in step 10 becomes the upper limit of the cylinder area. If the A_C chosen in step 5 is larger than the upper limit calculated in step 10, repeat steps 5 to 11.

While designing the motor, if the value of ϕ_0 is found to be small (smaller than about 20°), a larger value of R_d will have to be chosen. This is because a small ϕ_0 implies a steep driving profile, which would result in an awkward design for the cam and actuator.

By following the above procedure, the chief design parameters of the motor can be found. A minor adjustment, however, is needed at this point, to compensate for the straight-line driving profile approximation made initially. This adjustment is carried out by: fixing the values of R_a and R_d, increasing the slope of the profile (i.e. decreasing ϕ_0) and adding a circular end to the profile curve (thus making the profile similar to that shown in Fig. IV.7). As a result of the above adjustments, the values of ε and R_t will change. The new values can be calculated as follows: Referring to Fig. VI.3:

1- Draw vertical lines at the values R_d and R_a that have been fixed in Quadrants I and II respectively.

2- Draw a horizontal line at the intersection of the vertical from R_d with the new value of ϕ_0.

3- The intersection of the above horizontal line with the vertical from R_a, gives the new value of $(\phi_0 - \alpha + \varepsilon)$.

4- With ϕ_0 and α known, calculate ε.

5- From Quadrant III, find the new value of R_t^*, calculate R_t.

Determination of the values of the motor parameters (parameters are R_d, R_a, ϕ_0, ε, α, R_t, A_C, and H) as above, completes the theoretical design of the motor.

CHAPTER VII

CONCLUSION AND EXTENSIONS

In this thesis, a novel high torque, low speed pneumatic stepping motor which has potential applications in Low Cost Automation, was proposed and was followed by an experimental and theoretical investigation into its characteristics. The proposed design has the advantage of improved performance and ease of production, in comparison with earlier designs disclosed by a survey. The results from the analysis were shown to be in good agreement with the experimental data obtained from tests on the prototype. The analysis was hence used as a basis for a graphical design procedure, which was also described.

The chief advantages of the present motor are its high output torque, high accuracy of resolution, and particularly the feature of positive-locking between steps. These features make it eminently suitable for a wide range of digital industrial control applications, two examples of which are outlined in Appendix I.

Two apparent disadvantages of the motor must be mentioned. First, the motor cannot withstand high reverse torque, as a result of the momentary depressurization of the cylinders that occurs at the instant of power switchover between the cylinder. The time interval of this depressurization, which

is also the time available for any reverse torque to act and consequently jam the motor, is a result of the time delays involved in the switching of the supply valves. Possible solutions to overcome this problem are the use of faster switching valves and/or the use of a ratchet-pawl mechanism to prevent reverse motion. When two single-acting cylinders are employed, resistance to reverse torque may be also achieved by using suitably phased input signals (i.e. the 'driving' cylinder could be pressurized before release of the 'locked' cylinder).

The second drawback is the inability of the motor to step bidirectionally. However, a bidirectional motor utilizing the same actuation principle has been designed and built. Theoretical and experimental evaluation of this motor is already underway.

Further extensions on the topic of this thesis could include the following:

- Further work could be carried out on the effect of different cam driving profiles on the output performance. The objective of this would be to define profiles suitable for different applications (e.g. profiles resulting in low angular velocity at the end of the step would be more suitable for high inertia loads in order to reduce mechanical shock).

- Variation of phase relations between the input signals, as well as of their waveforms, could be investigated towards improving the reverse-torque tolerance of the motor.
- Although compressed air is utilized for power in the prototype, it is conceivable that a hydraulic stepping motor can be designed along similar lines. Such a motor can be used in cases where even higher torques are required.
- The graphical design procedure outlined in the thesis could also be utilized in a computer program for the purpose of optimizing design parameters.

REFERENCES

1- Anon, "Slo-Syn", Synchronous/Stepping Motors, Controls and Drives", Catalog SS1265-5.

2- Bell, R., Lowth, A.C. and Shelley, R.B., "The Application of Stepping Motors to Machine Tools". Machinery Publishing Co. Ltd., 1970.

3- Martin, R.P., Jr., "A Pneumatic Stepping Motor", Master of Science Thesis, Pennsylvania State University, 1965.

4- Howland, G.R., "Pneumatic Nutator Actuator Motor", Report No. BPAD-863-1671R (NASA CR-54788) Bendix Corp., Oct. 17, 1965.

5- Griffin, W.S., Cooley, W.C., "Development of High Speed Fluidic Logic Circuit for a Novel Stepping Motor", Advances in Fluidics ASME 1967.

6- Nomoto, A., and Shimada, K., "Fluidic Step Motor", Third Cranfield Fluidics Conference, Turin 1968.

7- Blaiklock, P.M., "Development of a Pneumatic Stepping Motor", IFAC Symposium on Fluidics, RAS London 1968.

8- Hunter, J.M., and Thompson, R.V., "Fluid Operated Stepping Motor", USA Patent No. 3,661,059, 1972.

9- Warren, R.W., "Fluid Stepping Motor", USA Patent No. 3,718,150, 1973.

10- Carlnas, B.E., "High Torque, Low Speed, Stepping Motor Actuated by a Fluidic System", Fifth Cranfield Fluidics Conference, Upssala, Sweden, 1972.

11- Dat, J., Fabre, J., and Yalcin, K., "Two Stepping Motors with Pneumatic or Hydraulic Control", Fifth Cranfield Fluidics Conference, Uppsala, Sweden, 1972.

12- Cheng, R.M.H., and Fahim, A., "Development of a High-Torque Low-Speed Pneumatic Stepping Motor", 4th International Fluid Power Symposium, Organized by the BHRA, Sheffield, England, April 1975.

13- Fahim, A., and Cheng, R.M.H., "Fluid Operated Stepping Motor", USA Patent Application No. 675,228, 1976.

14- Paynter, H.M., "Analysis and Design of Engineering Systems", Cambridge, Mass.: The MIT Press, 1961.

15- Kirshner, J.M. (Ed.) "Fluid Amplifiers", McGraw-Hill Book Company, 1966 [Section 11.7].

16- Blackburn, J.F., Reethof, G., and Shearer, J.L., "Fluid Power Control", The Technology Press of MIT and John Wiley and Sons Inc.

17- Andersen, B.W., "The Analysis and Design of Pneumatic Systems", John Wiley and Sons Inc., 1967.

18- Timoshenko, S.P., Young, D.H. and Weaver, W., Jr., "Vibration Problems in Engineering", D. Van Nostrand Co. Inc., 1955, pp. 9-13.

19- Marks, L.S., "Standard Handbook for Mechanical Engineers", McGraw-Hill Book Company, 1967.

20- Cheng, R.M.H., and Svoboda, J., "A Low Cost Pneumatic Programmable Sequential Control Unit", Hungarian Society of Mechanical Engineering, Pneumatics and Hydraulics 75 Gyor, 29 September, 1975.

APPENDIX A

DESIGN DRAWINGS OF THE PROTOTYPE MOTOR

Figures A.1 to A.12 show the design drawings of the prototype motor. A list of specifications of the components used is given below:

Shaft seal O-rings : LINEAR No. 11-014

Piston seal O-rings: LINEAR No. 11-020

Bearings : RHP Mj$^{\frac{1}{2}}$

Spring : SPEC C0600-045-0625 (St. Steel)

Figure A.13 shows a photograph of the motor.

Figure A.14 shows a photograph of the motor components.

Figure A.15 shows a photograph of the motor rotor components.

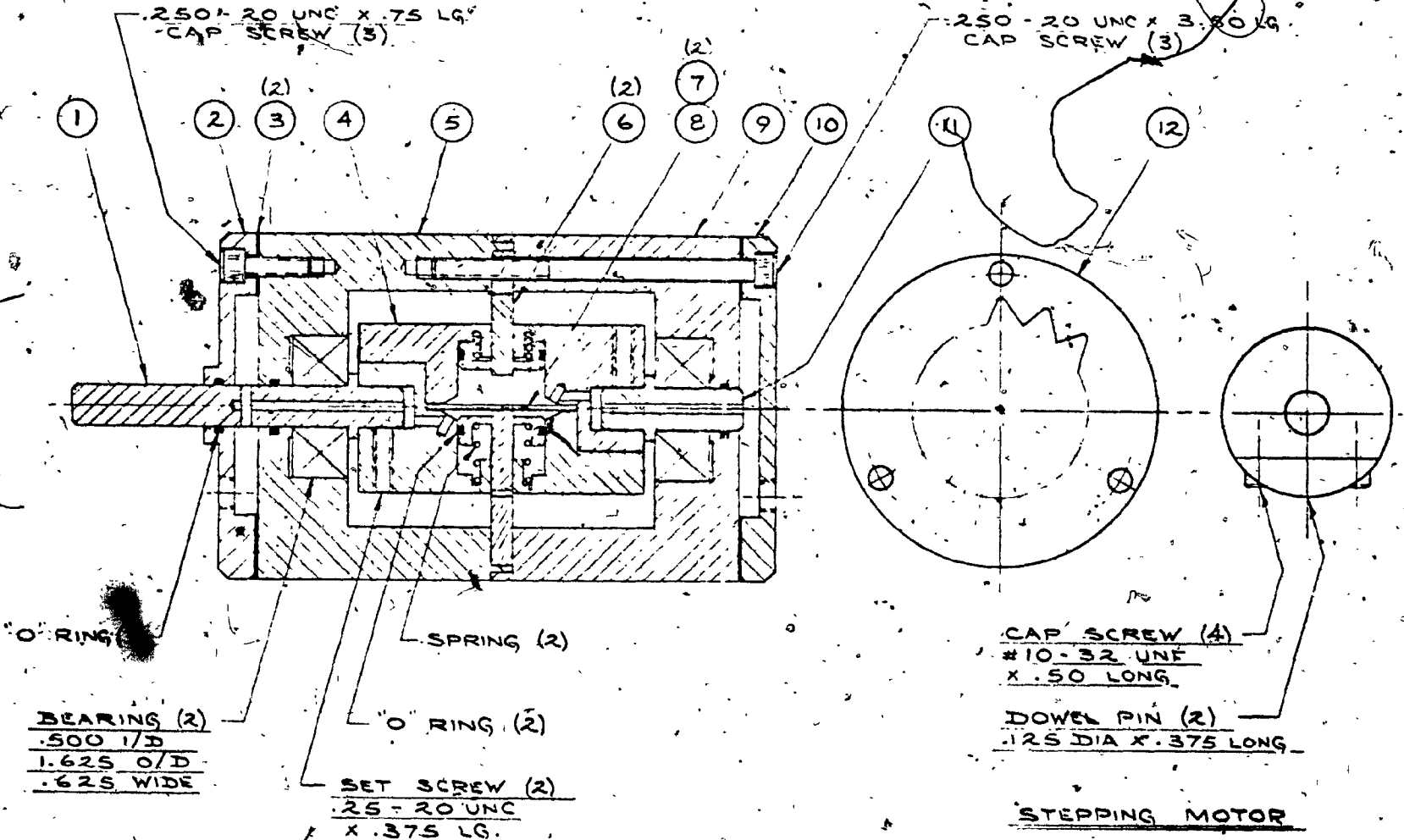

Fig. A.1: Design Drawings of the Stepping Motor (Continued).

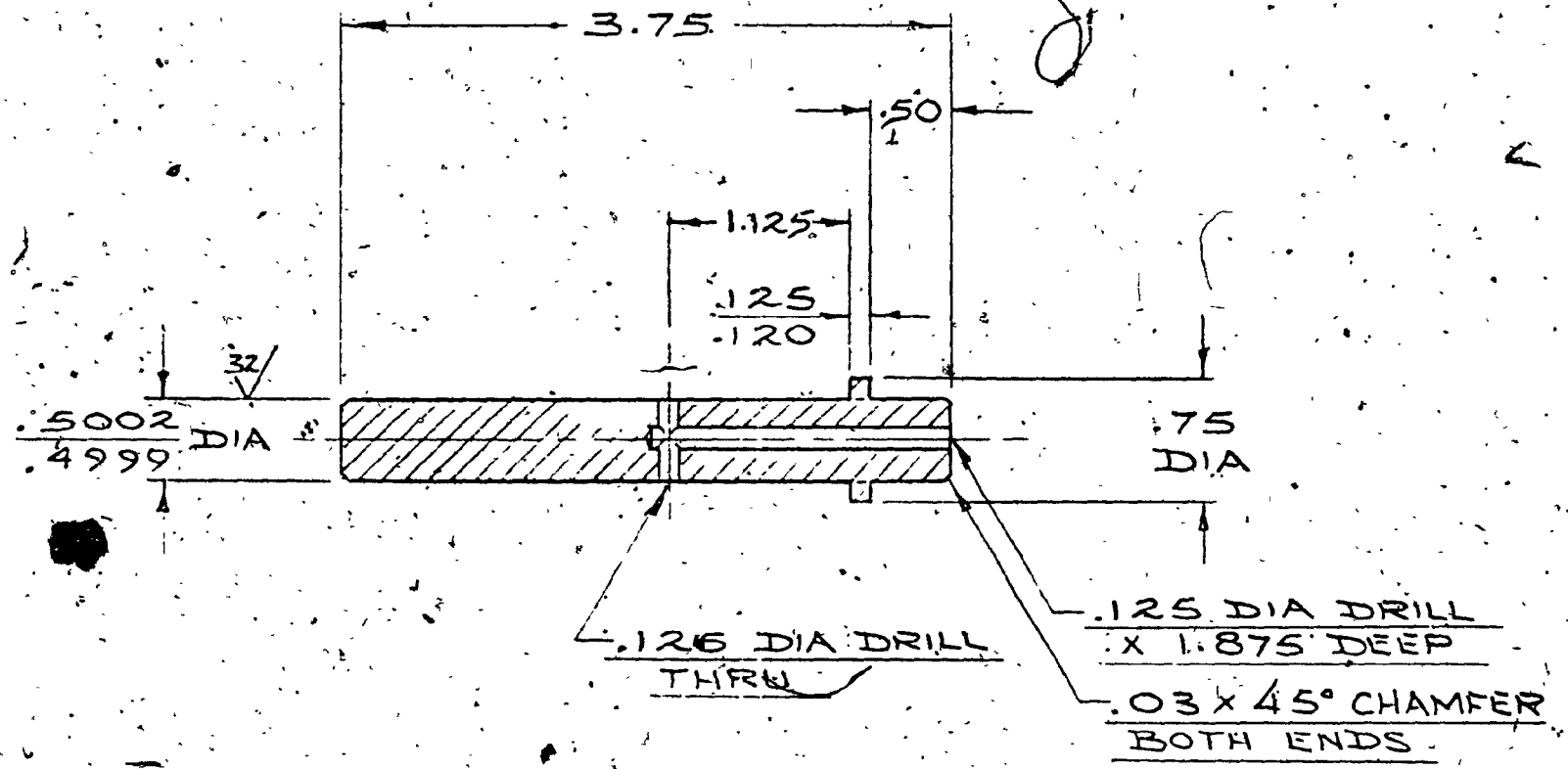

(1) MATERIAL: STEEL

STEPPING MOTOR

Fig. A.2: Design Drawings of the Stepping Motor (Continued).

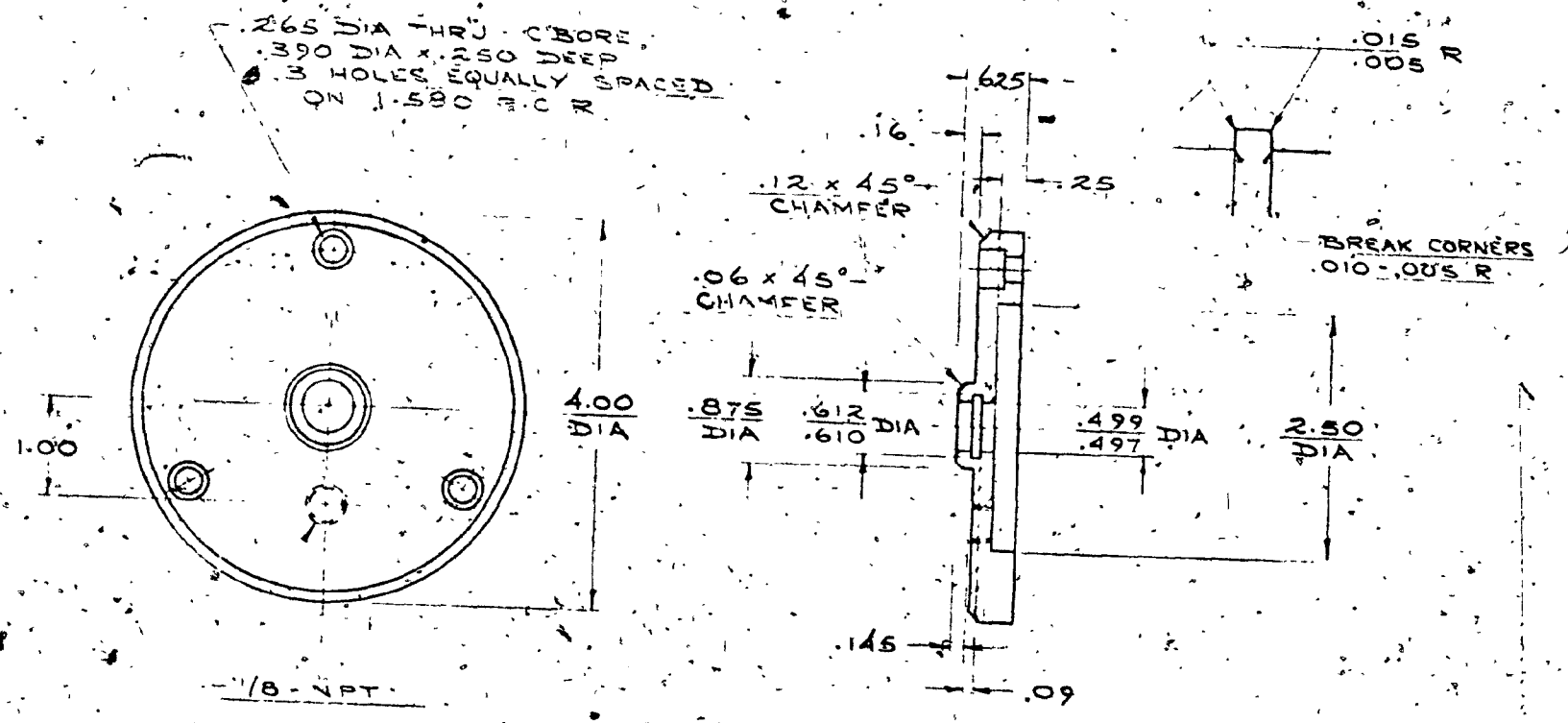

Fig. A.3: Design Drawings of the Stepping Motor (Continued).

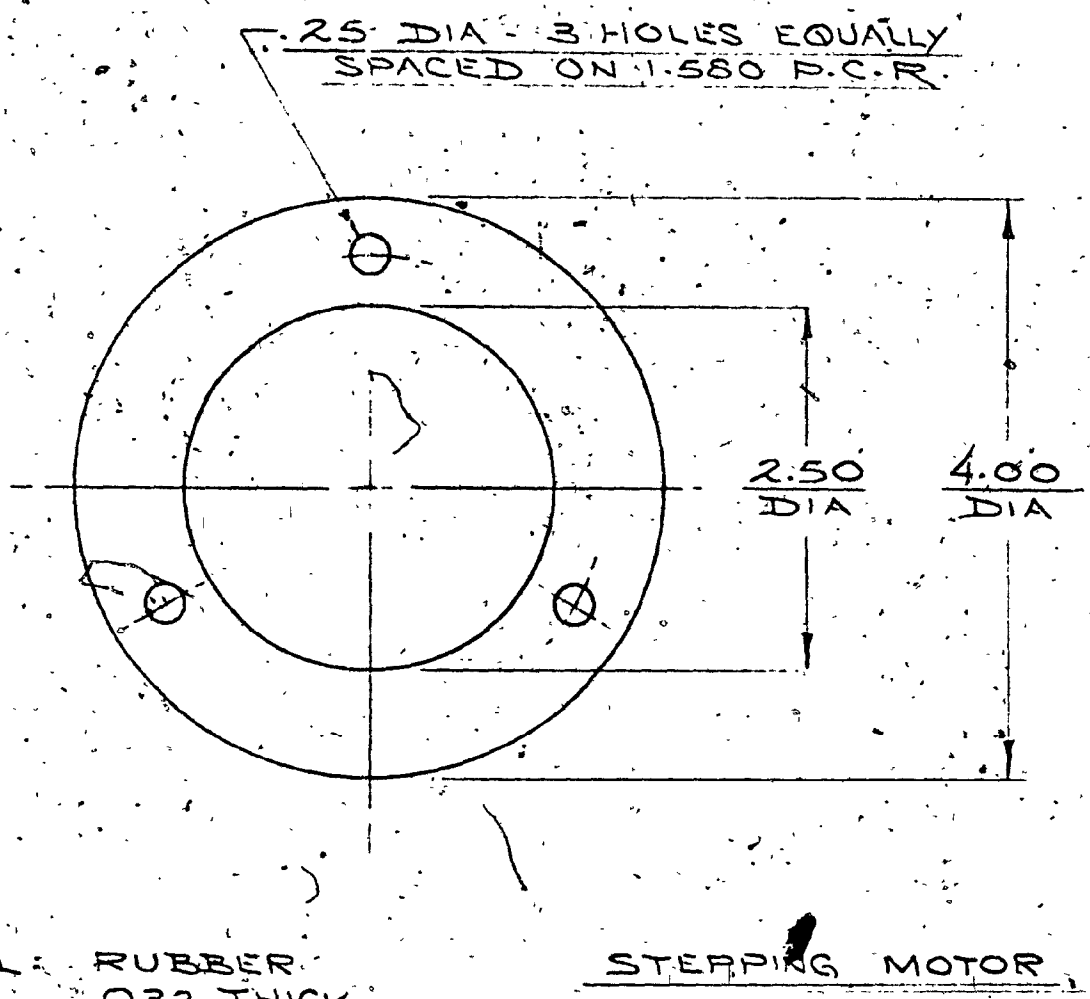

(3) MATERIAL: RUBBER .032 THICK

Fig. A.4: Design Drawings of the Stepping Motor (Continued).

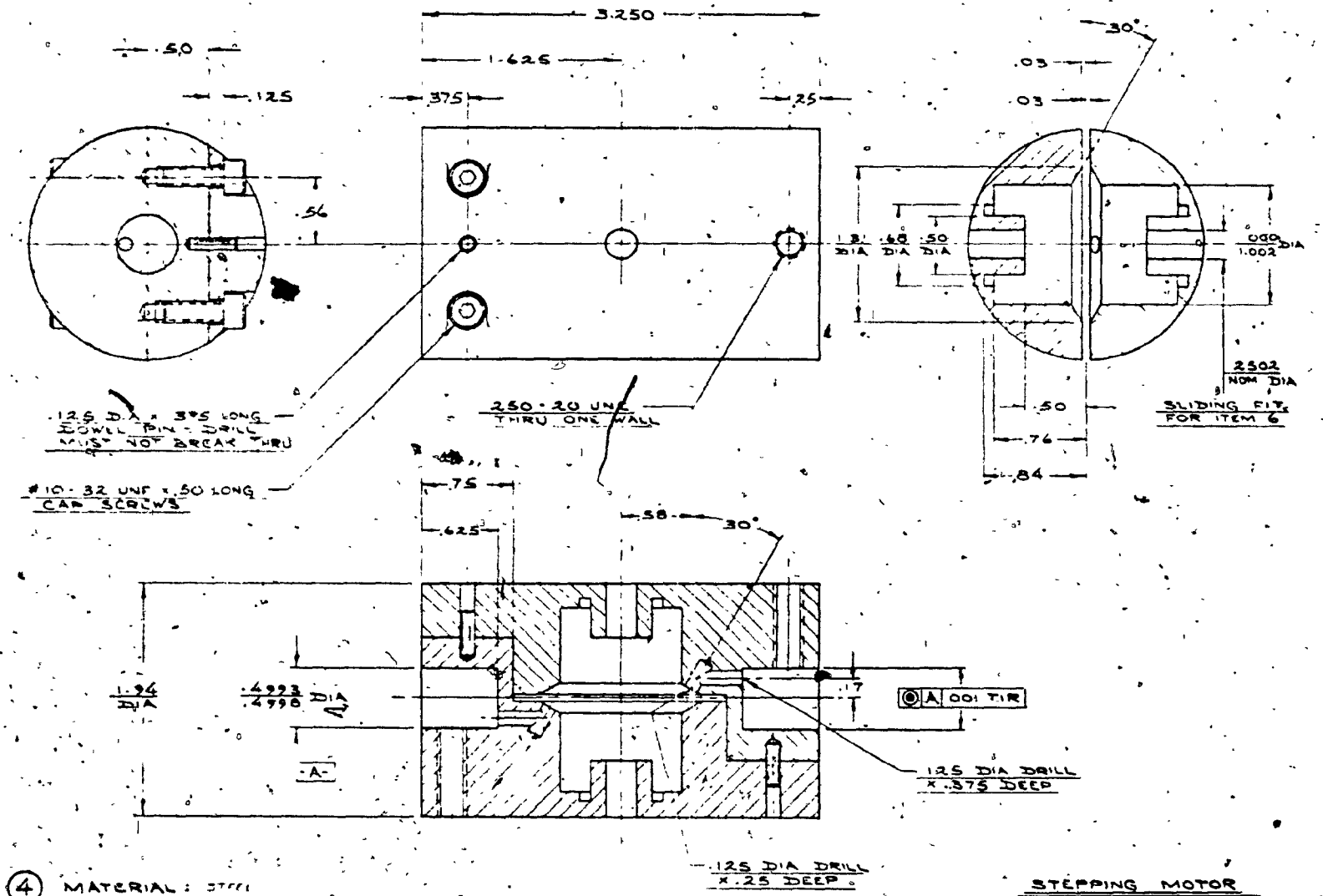

Fig. A.5: Design Drawings of the Stepping Motor (Continued).

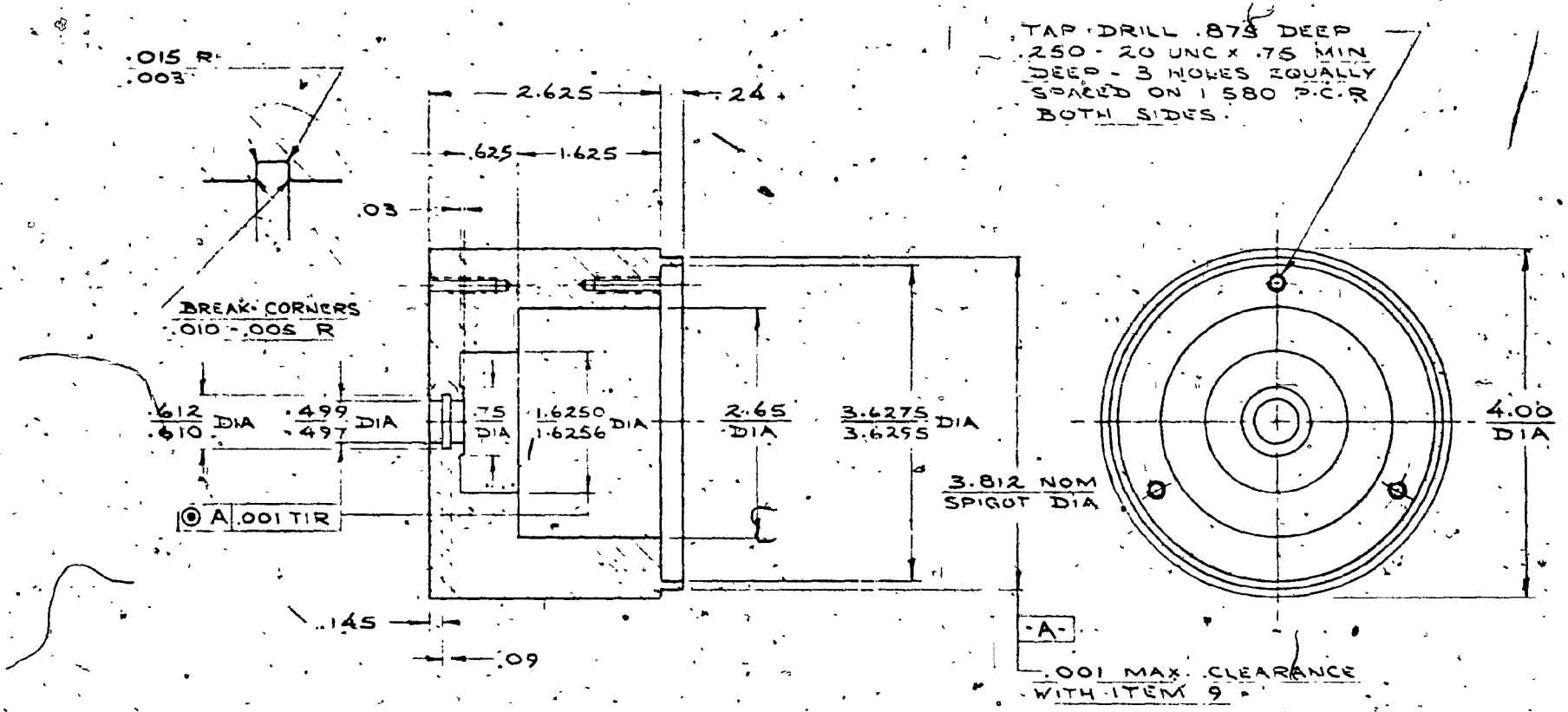

Fig. A.6: Design Drawings of the Stepping Motor (Continued).

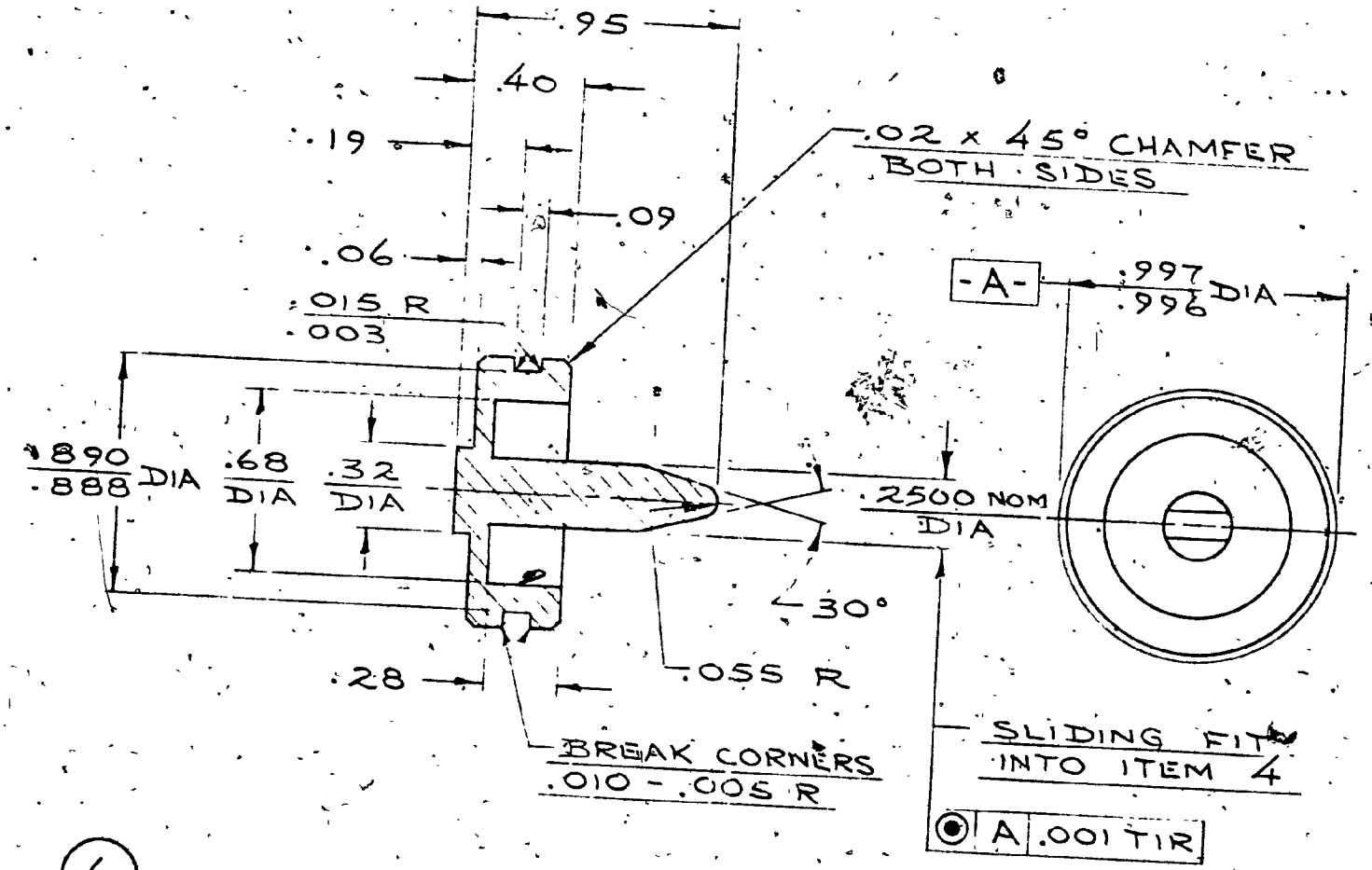

Fig. A.7: Design Drawings of the Stepping Motor (Continued).

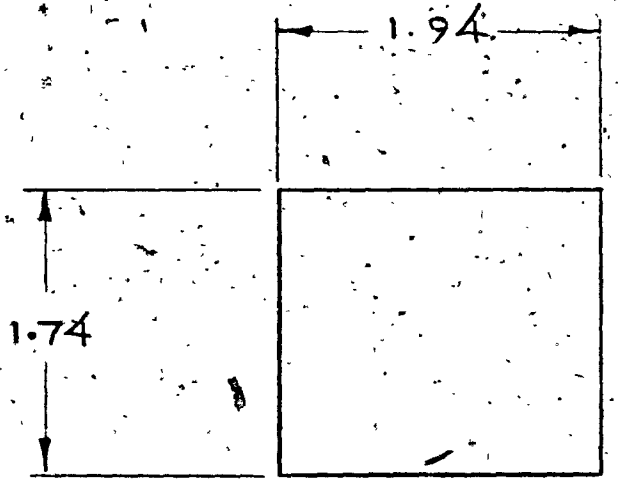

(7) MATERIAL: STEEL PLATE
.032 THICK

STEPPING MOTOR

Fig. A.8: Design Drawings of the Stepping Motor (Continued).

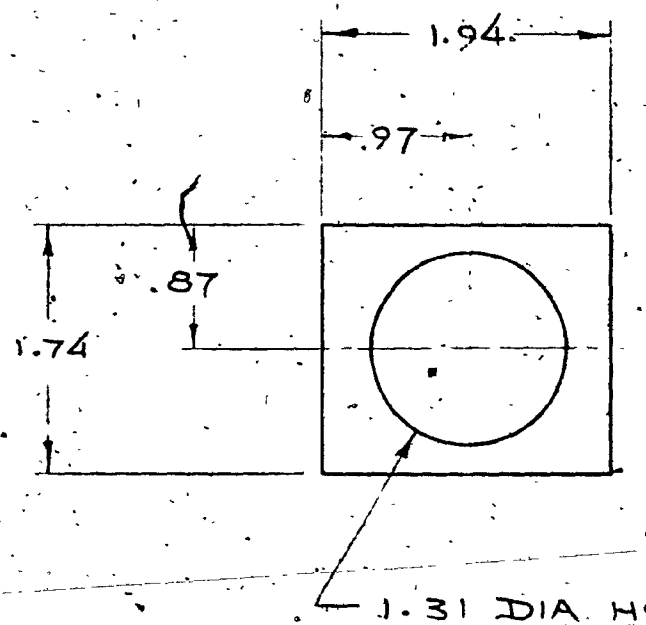

(8) MATERIAL: RUBBER GASKET
.015 THICK

STEPPING MOTOR

Fig. A.9: Design Drawings of the Stepping Motor (Continued).

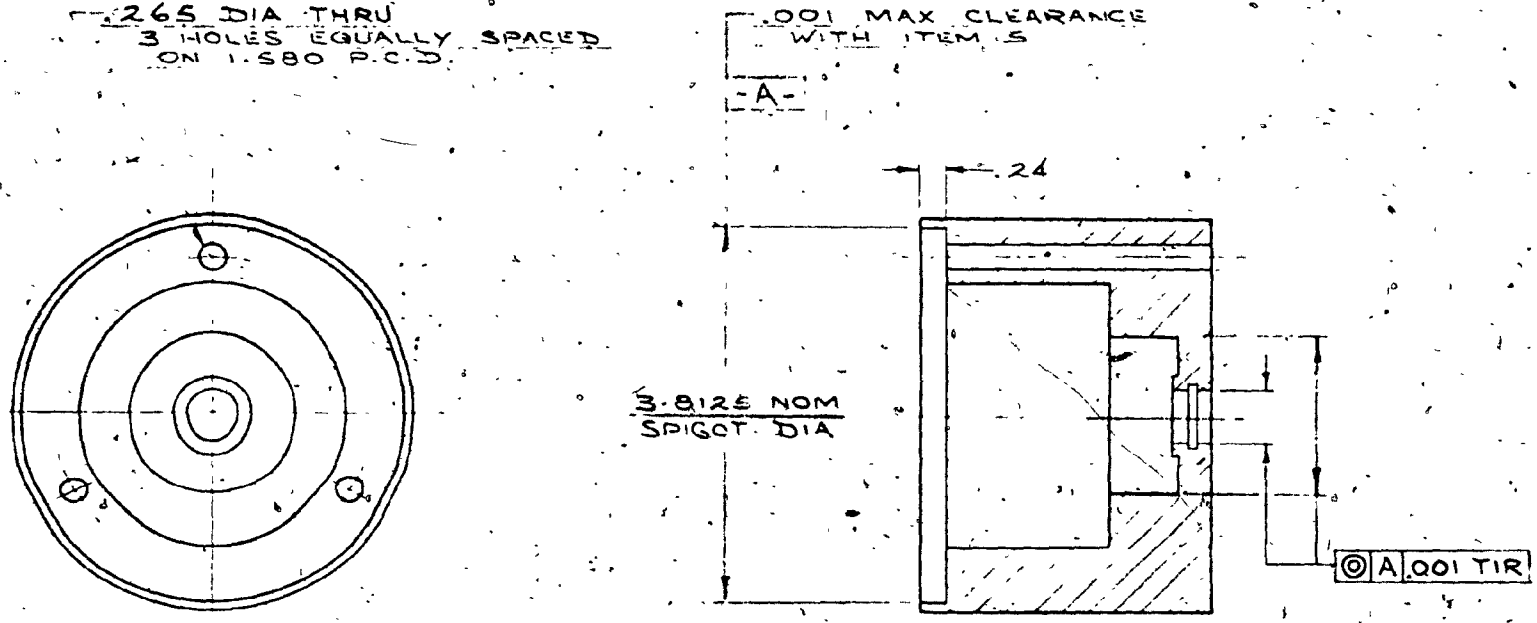

NOTE

DIMENSIONS NOT SPECIFIED ARE THE SAME AS SHOWN FOR ITEM 5.

(9) MATERIAL: ALUMINUM

STEPPING MOTOR

Fig. A.10: Design Drawings of the Stepping Motor (Continued).

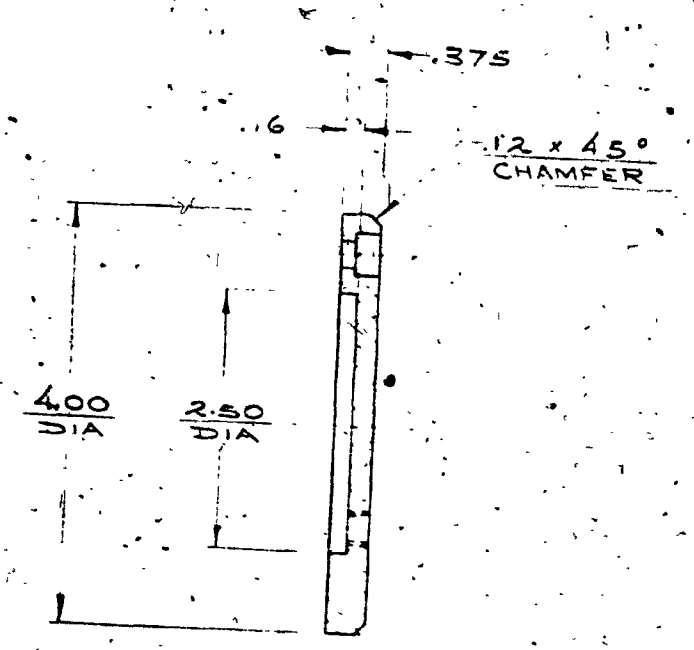

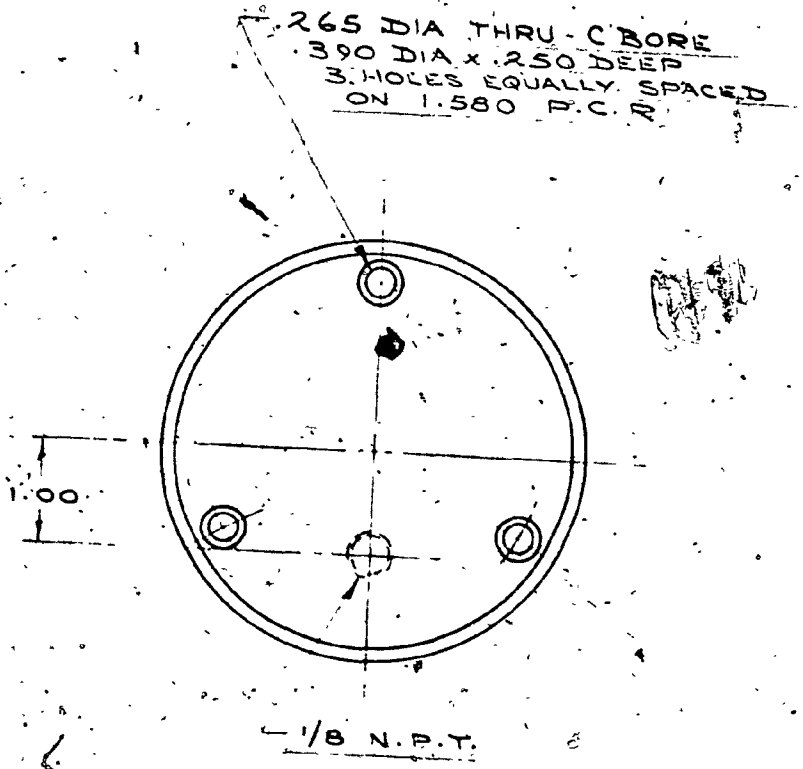

(10) MATERIAL: ALUMINUM

"STEPPING MOTOR"

Fig. A.11: Design Drawings of the Stepping Motor (Continued).

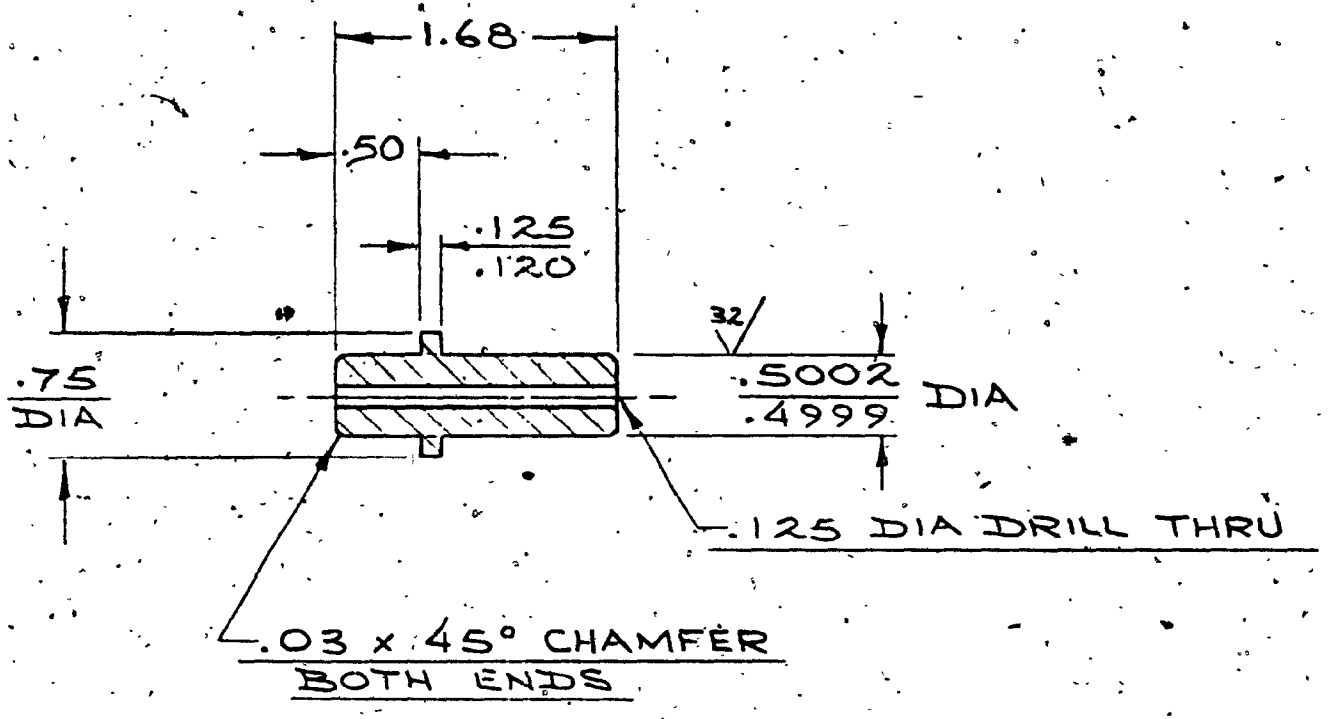

(11) MATERIAL: STEEL

STEPPING MOTOR

Fig. A.12: Design Drawings of the Stepping Motor (Continued).

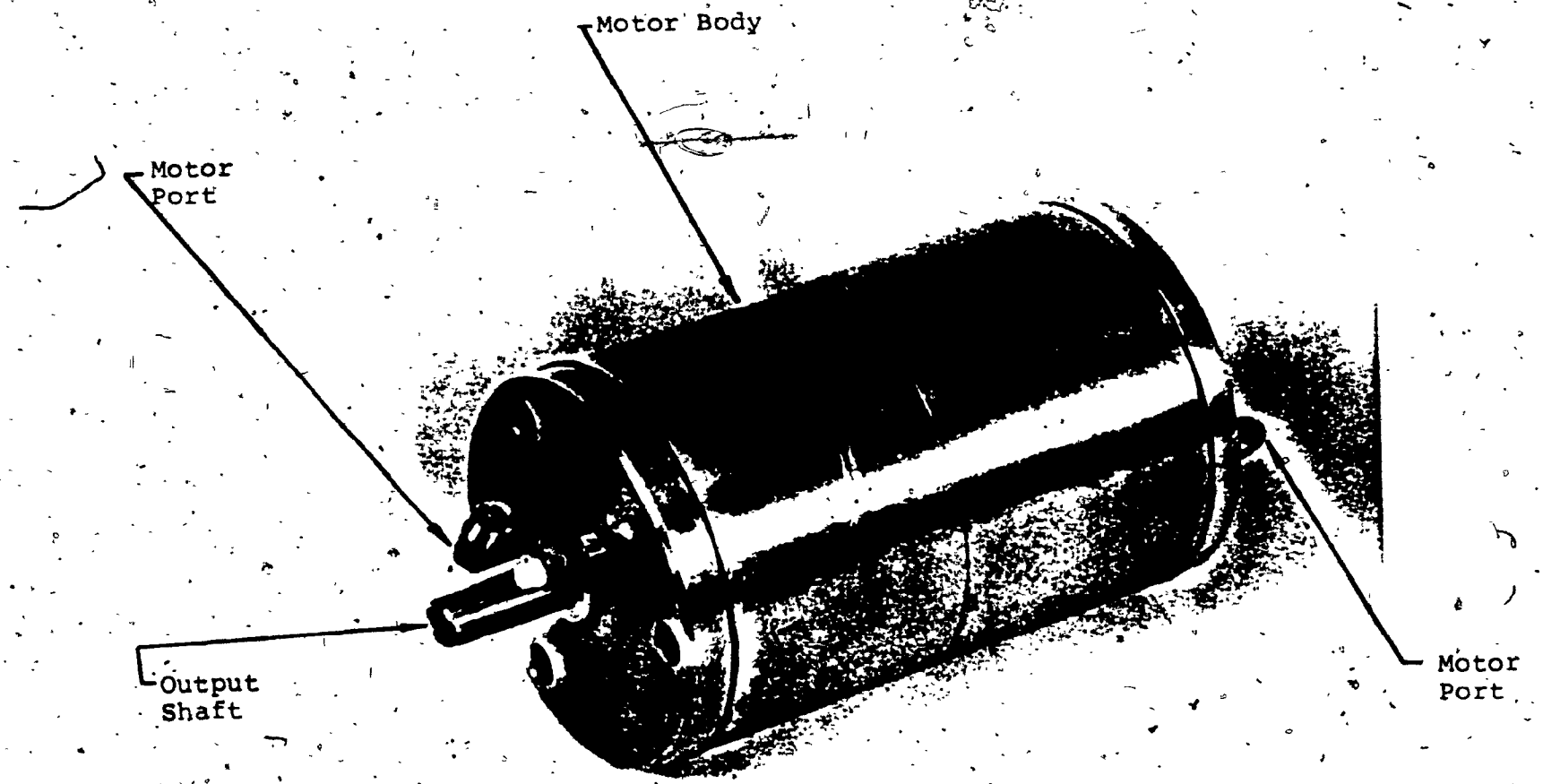

Fig. A.13: Photograph of the Prototype Motor.

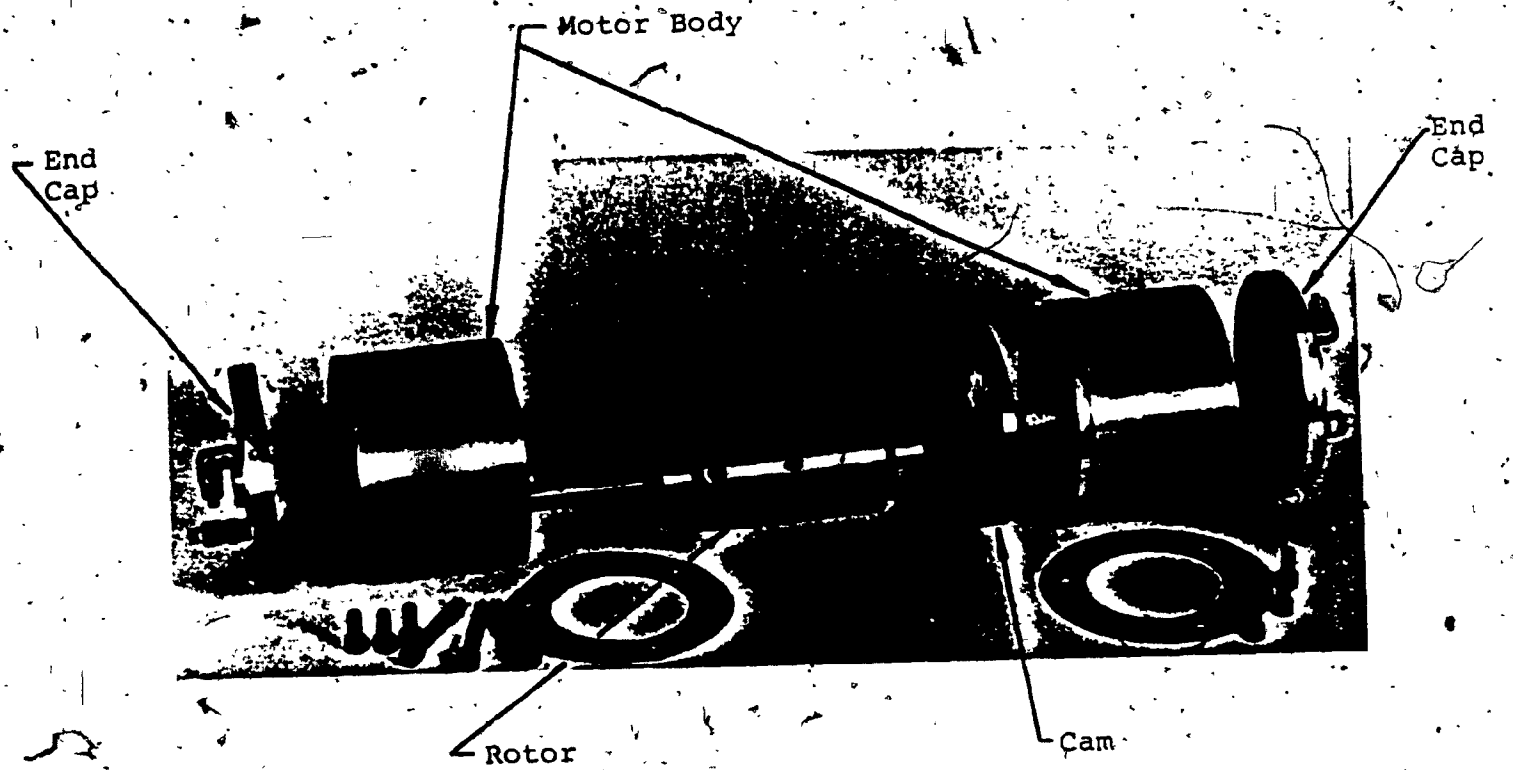

Fig. A.14: Photograph of the Motor Components.

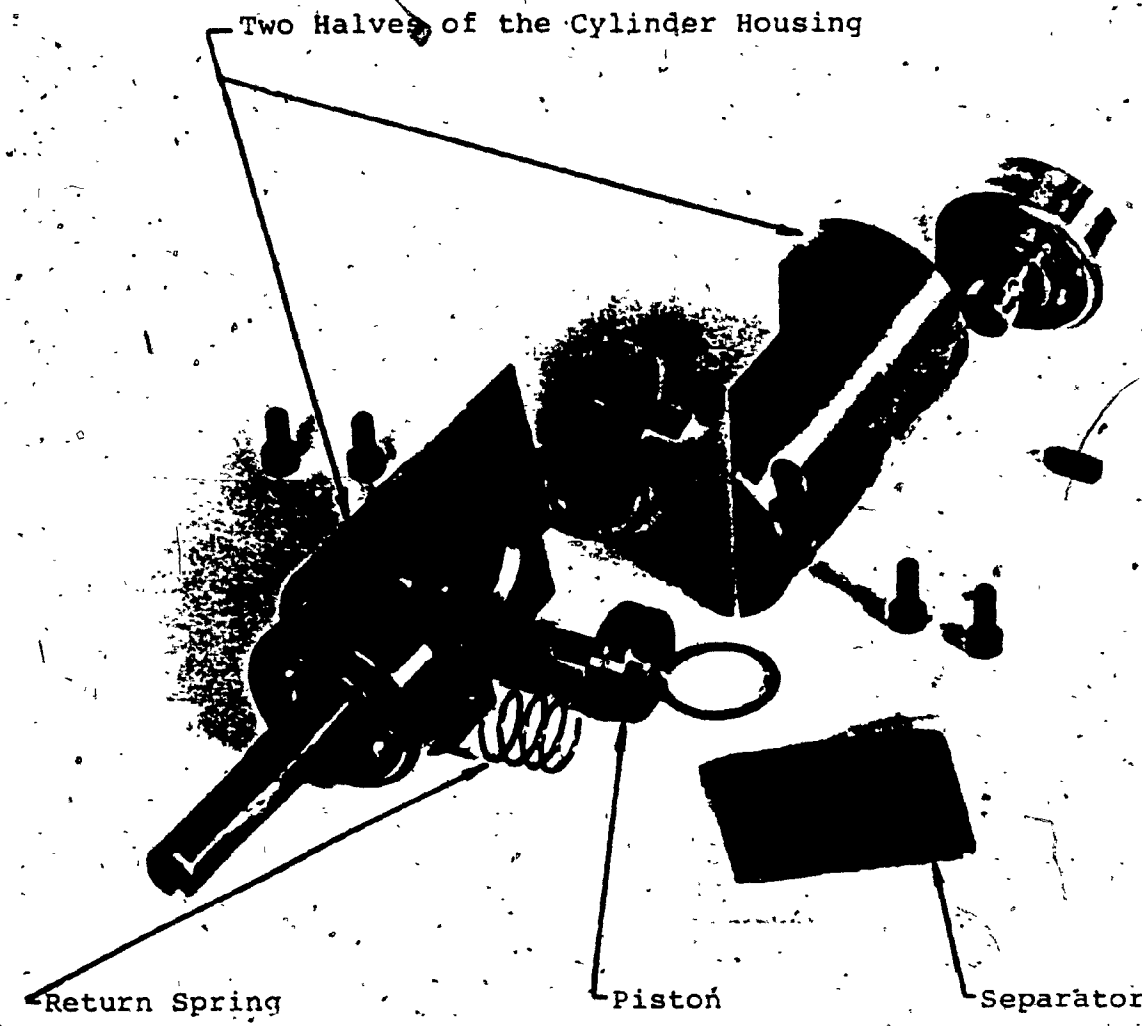

Fig. A.15: Photograph of the Motor Rotor Components.

APPENDIX B

EQUATION OF THE DRIVING PROFILE

(Straight line profile ending with a circular curve)

Figure B.1 shows a driving profile similar to the one used in the prototype motor. The profile consists of two parts: a straight line part up to angle λ, and a circular part between λ and α_s. Referring to the figure, the equation of the profile can be derived as follows:

a) Straight Line Part of the Profile

The angle ξ complements the initial angle of attack and is given by

$$\xi = \pi - \phi_0 \tag{B.1}$$

However, if ϕ_0 is not known, ξ can be calculated independently from Fig. B.1 as follows:

$$E = [R_d^2 + (R_a - R_t)^2 - 2(R_a - R_t)R_d \cos\alpha_s]^{\frac{1}{2}} \tag{B.2}$$

$$\beta = \sin^{-1}\left[\frac{(R_a - R_t)\sin\alpha_s}{E}\right] \tag{B.3}$$

and

$$\gamma = \sin^{-1}\left[\frac{R_t}{E}\right] \tag{B.4}$$

$$\xi = \beta + \gamma = \sin^{-1}\left[\frac{(R_a - R_t)\sin\alpha_s}{E}(1 - R_t^2/E^2)^{\frac{1}{2}} + \frac{R_t}{E}\left(1 - \frac{(R_a - R_t)^2 \sin^2\alpha_s}{E^2}\right)^{\frac{1}{2}}\right] \tag{B.5}$$

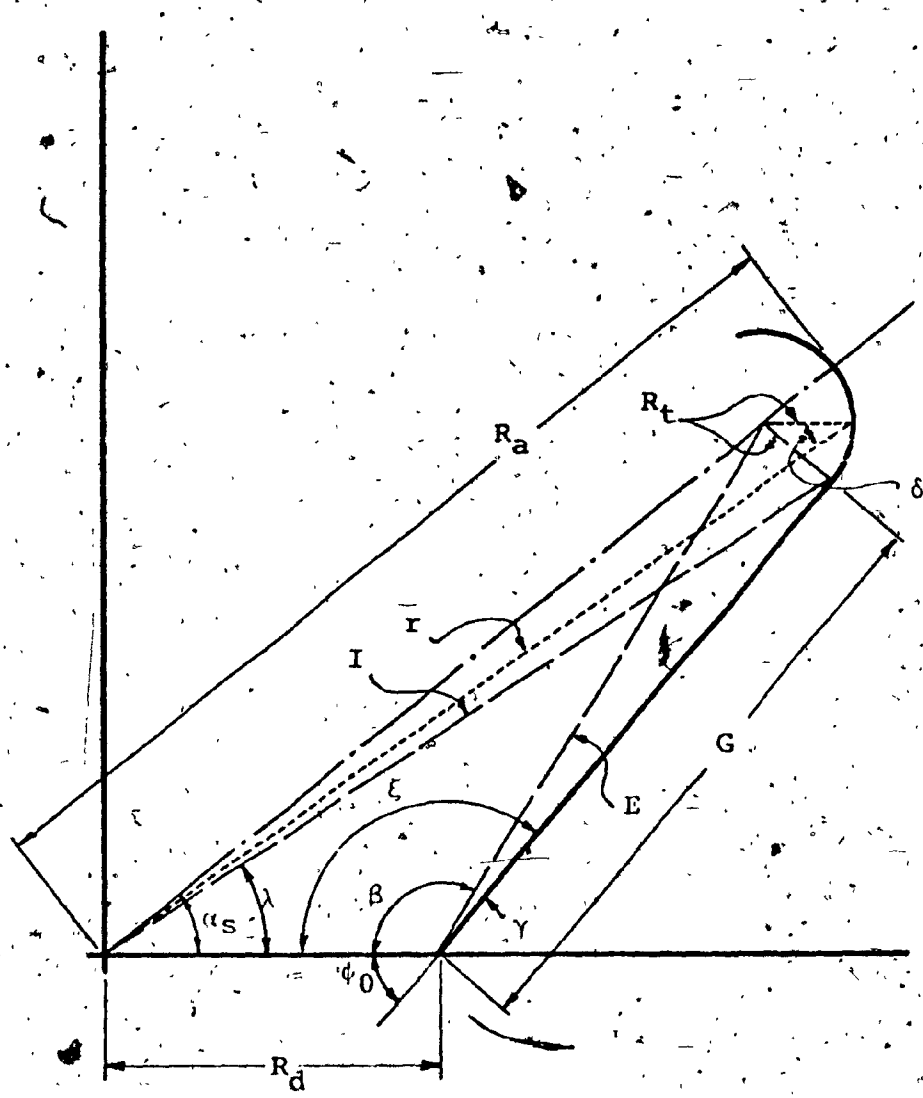

Fig. B.1: Driving Profile.

The equation of the straight line part of the profile is calculated using analytical geometry:

$$y - 0 = \tan(\pi-\xi)\,[x - R_d]$$

or $$y = x\tan\xi - R_d\tan\xi \qquad (B.6)$$

Substituting $y = r\sin\theta$

and $x = r\cos\theta$ in Eq. B.6

$$r = \frac{R_d\tan\xi}{\tan\xi\cos\theta - \sin\theta} \qquad (B.7)$$

b) End of the Straight Line Part of the Profile Angle

From Fig. B.1,

$$G = [E^2 - R_t^2]^{\frac{1}{2}} \qquad (B.8)$$

$$I = [R_d^2 + G^2 - 2R_dG\cos\xi] \qquad (B.9)$$

and the angle λ at which the straight line part of the profile ends is given by:

$$\lambda = \sin^{-1}\left[\frac{G\sin\xi}{I}\right] \qquad (B.10)$$

c) Circular Part of the Profile

The angle δ between the moving radii r and R_t at any point on the circular part of the profile is given by:

$$\delta = \sin^{-1}\left[\frac{(R_a-R_t^o)\sin(\alpha_s-\theta)}{R_t}\right] \qquad (B.11)$$

Thus, the equation of the circular part of the profile is:

$$r = R_t\cos\delta + (R_a-R_t)\cos(\alpha_s-\theta) \qquad (B.12)$$

The equation of the driving profile is given by Eqs. B.7, B.10 and B.12 above and can be written as:

$$\left.\begin{aligned} r &= \frac{R_d \tan\xi}{\tan\xi \cos\theta - \sin\theta} && 0° < \theta \leq \lambda \\ &= R_t\cos\delta + (R_a - R_t)\cos(\alpha_s - \theta) && \lambda \leq \theta \leq \alpha_s \end{aligned}\right\} \quad (B.13)$$

In nondimensional form, Eq. B.13 can be expressed as follows:

$$\left.\begin{aligned} r^* &= \frac{\tan\xi}{\tan\xi \cos\theta - \sin\theta} && 0° \leq \theta \leq \lambda \\ &= R_t^*\cos\delta + (R_a^* - R_t^*)\cos(\alpha_s - \theta) && \lambda \leq \theta \leq \alpha_s \end{aligned}\right\} \quad (B.14)$$

APPENDIX C

SOLUTION OF THE EQUATIONS OF FORCE AND TORQUE BALANCE OF THE PISTON AND CYLINDER

[The equations from the text are listed here again, but are, re-numbered for ease of reference. Thus, Eqs. IV.8a through IV.10c in the text are identical with Eq. C.1 through C.7 in this appendix].

$$R_1 - R_2 + \mu_1 N \sin\phi - N\cos\phi = 0 \qquad (C.1)$$

$$F - N\sin\phi - \mu_1 N\cos\phi - \mu_2 (R_1 + R_2) = 0 \qquad (C.2)$$

$$R_1 \ell_1 + \mu_1 Nr\sin\phi - R_2 \ell_2 - Nr\cos\phi = 0 \qquad (C.3)$$

$$F = p_C A_C - K_S f - f_{CS} \qquad (C.4)$$

$$R_1 - R_2 + R_x = 0 \qquad (C.5)$$

$$R_y + \mu_2 (R_1 + R_2) - F = 0 \qquad (C.6)$$

$$T_M - R_1 \ell_1 + R_2 \ell_2 = 0 \qquad (C.7)$$

The solution is as follows:

From Eq. C.1

$$R_1 = R_2 + N\cos\phi - \mu_1 N\sin\phi \qquad (C.8)$$

From Eq. C.3

$$R_1 = [R_2 \ell_2 + Nr\cos\phi - \mu_1 Nr\sin\phi]/\ell_1 \qquad (C.9)$$

Substituting Eqs. C.8 and C.9 into Eq. C.3

$$\ell_1 R_2 + \ell_1 N(\cos\phi - \mu_1 \sin\phi) = R_2 \ell_2 + Nr(\cos\phi - \mu_1 \sin\phi) \qquad (C.10)$$

Simplifying Eq. C.10

$$R_2 = N(\cos\phi - \mu_1 \sin\phi) \frac{(r - \ell_1)}{(\ell_1 - \ell_2)} \qquad (C.11)$$

Substituting Eq. C.11 into Eq. C.8

$$R_1 = N(\cos\phi - \mu_1 \sin\phi) \frac{(r-\ell_1)}{(\ell_1-\ell_2)} + N(\cos\phi - \mu_1 \sin\phi) \qquad (C.12)$$

Again simplifying Eq. C.12 to obtain

$$R_1 = N(\cos\phi - \mu_1 \sin\phi) \cdot [\frac{r - \ell_2}{\ell_1 - \ell_2}] \qquad (C.13)$$

and substituting Eqs. C.13 and C.11 into Eq. C.2

$$F = N(\sin\phi + \mu_1 \cos\phi) + \mu_2 N(\cos\phi - \mu_1 \sin\phi) [\frac{r-\ell_2+r-\ell_1}{\ell_1 - \ell_2}] \qquad (C.14)$$

Using the relation $S = \ell_1 - \ell_2$ and solving Eq. C.14 for N,

$$N = \frac{F\ S}{(\sin\phi + \mu_1 \cos\phi)(s + \mu_2 (2r - (\ell_1 + \ell_2)))} \qquad (C.15)$$

Now, from Eqs. C.7, C.11 and C.13, solution for T_M yields:

$$T_M = Nr(\cos\phi - \mu_1 \sin\phi) \qquad (C.16)$$

Substituting Eq. C.15 into Eq. C.16, the torque equation is given by:

$$T_M = \frac{F\ r\ S}{S + \mu_2 (2r - (\ell_1 + \ell_2))} \cdot \frac{\cos\phi - \mu_1 \sin\phi}{\sin\phi + \mu_1 \cos\phi} \qquad (C.17)$$

For the motor configuration shown in Fig. IV.1:

$$\ell_1 = R_d \quad \text{and} \quad \ell_2 = R_d - S$$

Thus Eq. C.17 can be written as

$$T_M = \frac{F\ r\ S}{S+\mu_2(2r-2R_d+S)} \cdot \frac{\cos\phi-\mu_1\sin\phi}{\sin\phi+\mu_1\cos\phi} \qquad (C.18)$$

Expressing the coefficient of friction μ_1 in terms of the pressure angle ψ_1 [$\mu=(\sin\psi_1)/(\cos\psi_1)$] and substituting Eq. C.18, we obtain

$$T_M = \frac{F\ r\ S}{S+\mu_2(2r-2R_d+S)} \cdot \frac{\cos\phi\cos\psi_1-\sin\phi\sin\psi_1}{\sin\phi\cos\psi_1+\cos\phi\sin\psi_1} \qquad (C.19)$$

Using trigonometric rules, Eq. C.19 can be further simplified to yield:

$$T_M = \frac{F\ r\ S}{S+\mu_2(2r-2R_d+S)} \cdot \cot(\phi+\psi_1) \qquad (C.20)$$

APPENDIX D

CALCULATION OF THE CONTROL VALVES EQUIVALENT AREA AND OPENING TIME

The control valves used in the prototype system are the Festo Model No. 007-098. Double Diaphragm Pressure Amplifiers. Two of these valves are connected in parallel to supply each cylinder with the required flow rate. Thus, Figure D.1a shows the manifold block on which the four valves, employed to control the two stepping motor cylinders, are mounted.

D.1 Equivalent Area of the Valve

The experimental setup, shown schematically in Fig. D.1b, was used to collect the necessary data for the equivalent area calculations. In the setup, the pressures upstream and downstream of the valve were recorded by the pressure transducers shown, and the flow was measured using a linear electronic flowmeter. The flow through the valve was regulated by the needle valve on the downstream side. Thus, the downstream pressure could be varied by adjusting the needle valve. The experiment was conducted with the valve fully opened. In the tests, the upstream pressure is maintained at a constant value using the pressure regulator, and the downstream pressure is varied by means of the needle valve. Curves of the mass flow rate of air, versus the

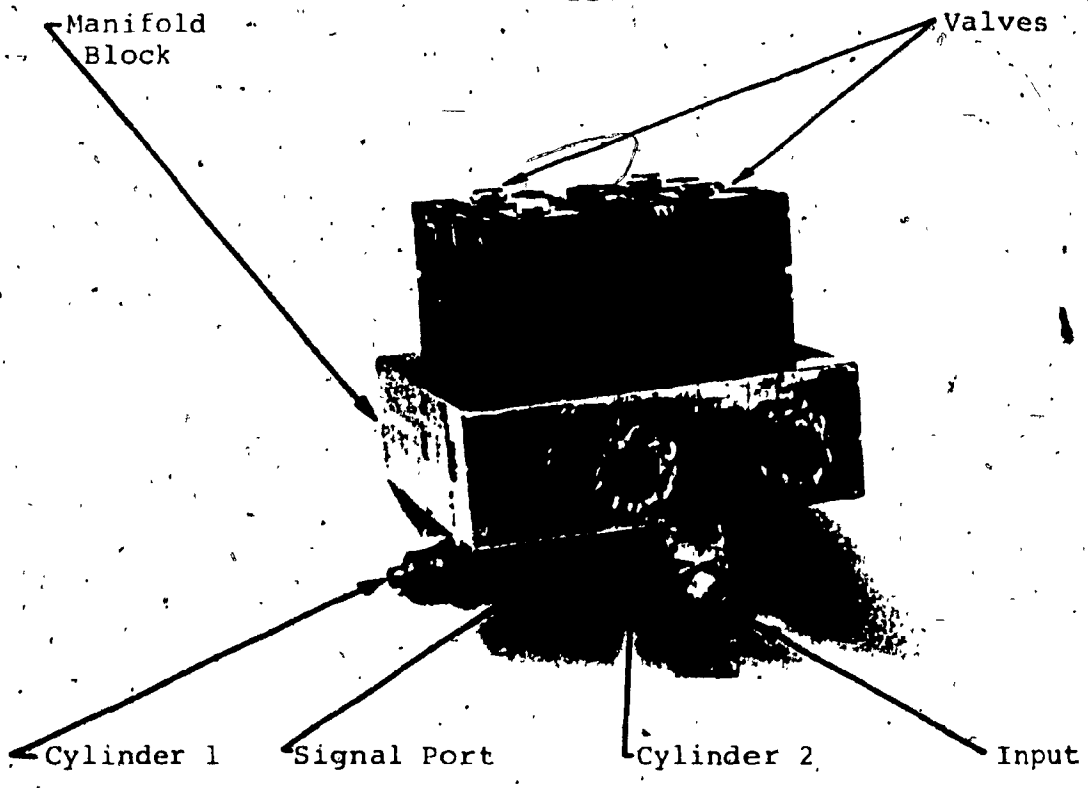

Fig. D.1a: Photograph of the Manifold Block and the Control Valves of the Motor System.

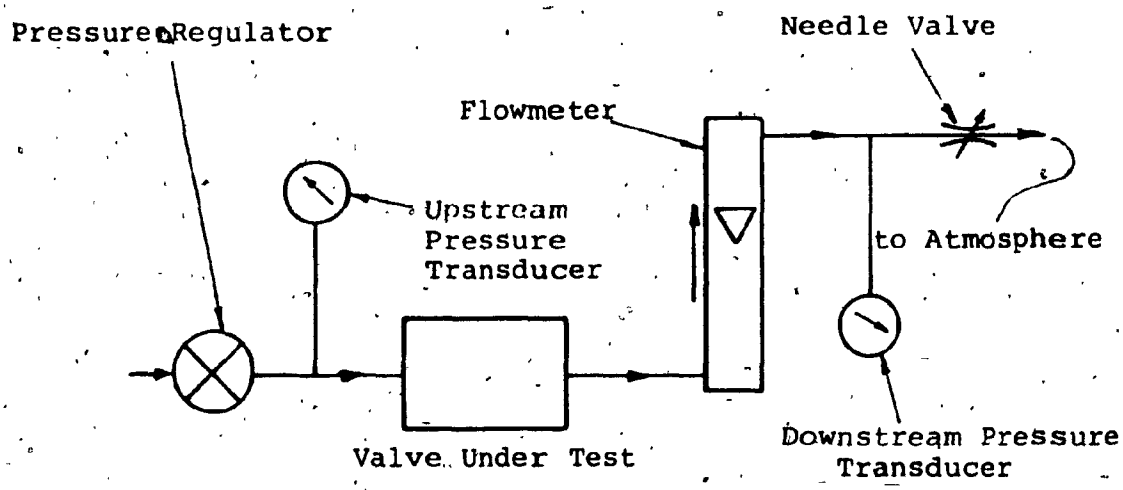

Fig. D.1b: Schematic of the Experimental Setup for Testing the Valve.

downstream pressure, are then plotted for different supply pressures. These curves are shown in Fig. D.2a.

The valve equivalent area is calculated by substituting the data of Fig. D.2a in the following equations:

$$W = \frac{A_V P_u}{\sqrt{t_s}} \sqrt{\frac{k}{R} \left(\frac{2}{k+1}\right)^{\frac{k+1}{k-1}}} \quad \text{when} \quad \frac{P_d}{P_u} \leq \left(\frac{2}{k+1}\right)^{\frac{k}{k-1}}$$

[Eq. 2.1.13 Ref. 17]

$$= \frac{A_V P_u}{\sqrt{t_s}} \sqrt{\frac{2k}{R(k-1)}} \left(\frac{P_d}{P_u}\right)^{1/k} \sqrt{1 - \left(\frac{P_d}{P_u}\right)^{\frac{k-1}{k}}}$$

$$\text{when} \quad \frac{P_d}{P_u} > \left(\frac{2}{k+1}\right)^{\frac{k}{k-1}}$$

[Eq. 3.86 Ref. 16]

The plot of the valve equivalent area A_V versus the pressure ratio $\frac{P_d}{P_u}$ for different supply pressures is shown in Fig. D.2b. An average value of $A_V = 0.0061$ sq.in is taken as the equivalent area of the valve over the range of the operating pressure.

D.2 Opening Time of the Valve

The time required by the valves to open fully was measured experimentally. The valve is made to oscillate by applying a symmetric square-wave signal to its pilot port, and the diaphragm position is visually monitored by using a stroboscope. The frequency beyond which the valve fails to reach the fully opened position was found to be

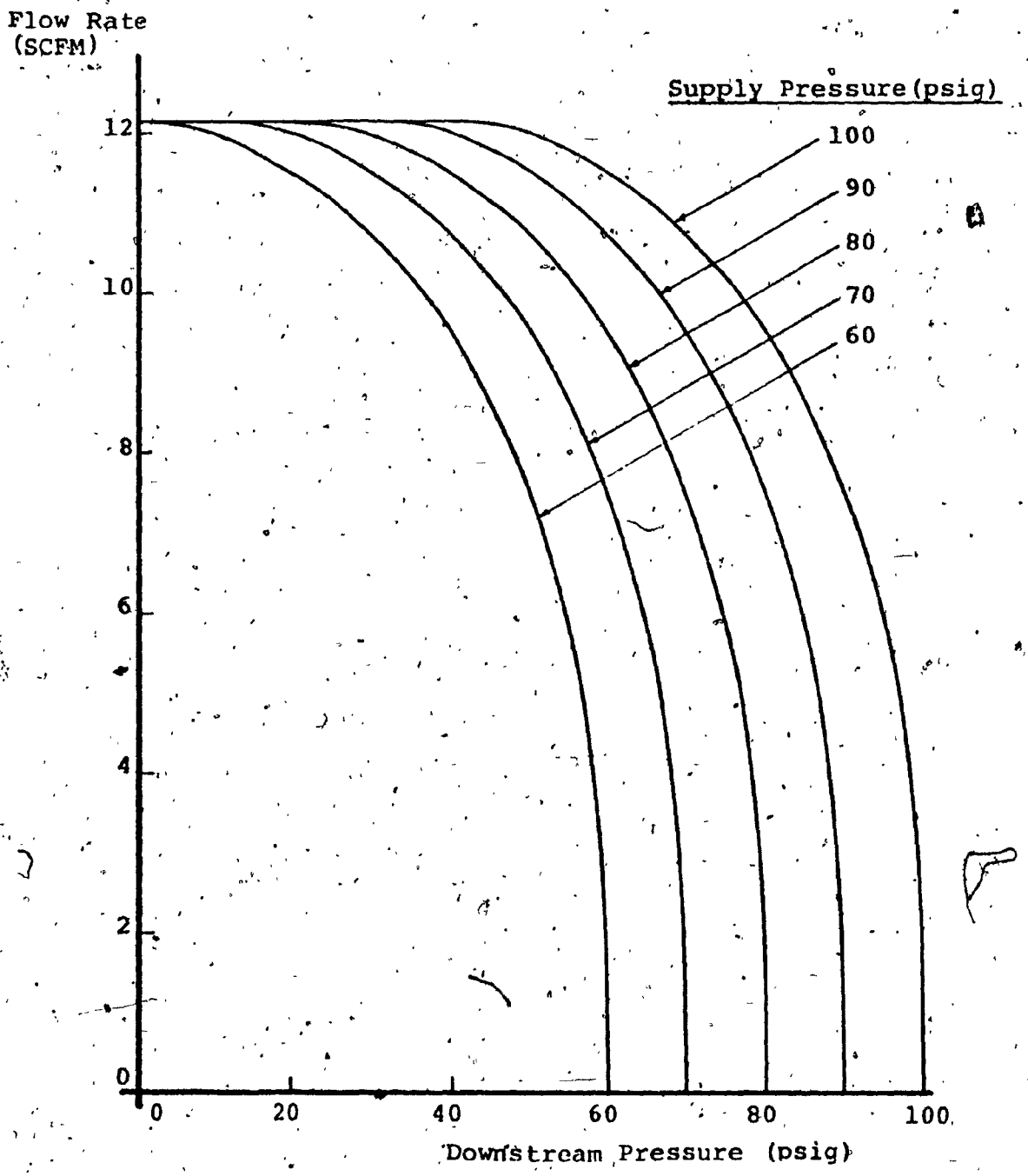

Fig. D.2a: Pressure Flow Characteristics of the Valve Used in the System.

45 Hz (@ 1 psig pilot signal) as compared to the figure of 30 Hz (@ 0.3 psig pilot signal) quoted by the manufacturer.

Assuming equal opening and closing times, the opening or closing time of the valve τ_v would be approximately 11 msec.

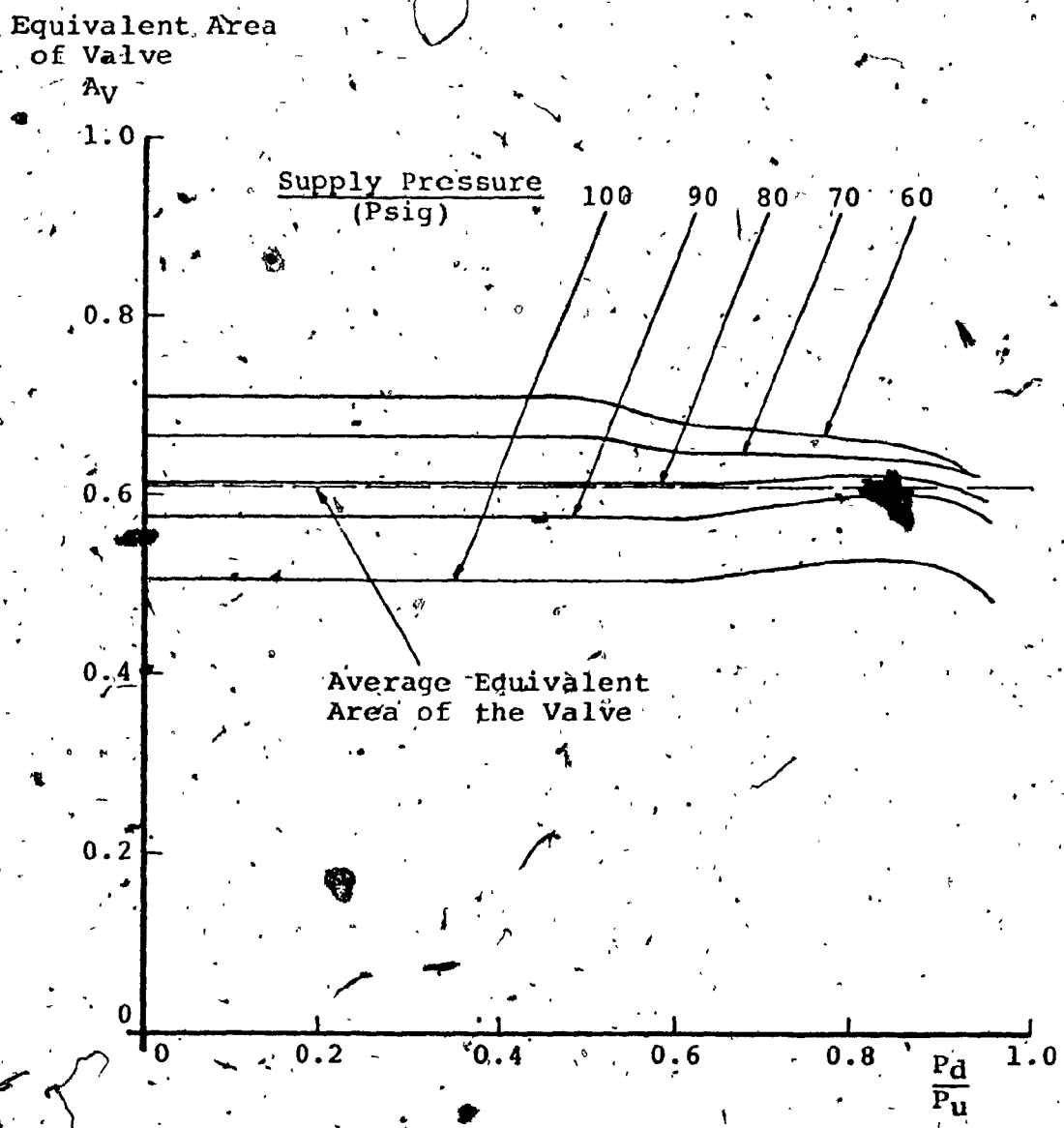

Fig. D.2b: Equivalent Area of Valve Versus Pressure Ratio.

APPENDIX E

THE CHARGING PROCESS OF A PNEUMATIC VOLUME

Since the charging of both fixed and variable volumes are involved in the analysis, a general equation for charging of a pneumatic volume (i.e. pneumatic cylinder) will be derived. Figure E.1 shows schematically a pneumatic cylinder. The following assumptions are made:

a) The working fluid (air) is a perfect gas with constant specific heat values.

b) The process is too rapid for any heat transfer to occur and is hence adiabatic.

c) Entrance losses for the cylinder are negligible.

The equation of the pressure rise in the volume is derived then as follows:

let h be the total energy of fluid in the volume,
e be the internal energy,
and w be the work done by the fluid in the volume.

From the law of conservation of energy:

$$h = e + w \qquad (E.1)$$

Differentiating with respect to time, we get:

$$\frac{dh}{dt} = \frac{de}{dt} + \frac{dw}{dt} \qquad (E.2)$$

The internal energy of the fluid in the cylinder, according to Joule's law is given by:

$$e = c_v \, m_v \, T_v \qquad \text{(E.3)}$$

where c_v is the specific heat of the fluid at constant volume, m_v the mass of fluid present in the cylinder, and T_v is the absolute temperature of the fluid in the cylinder. Differentiating Eq. E.3, the change in the internal energy with respect to time is given by:

$$\frac{de}{dt} = m_v \, c_v \, \frac{dT_v}{dt} \qquad \text{(E.4)}$$

The work done by the fluid in the cylinder is given by:

$$w = \int p_v \, dV_v \qquad \text{(E.5)}$$

where p_v is the instantaneous pressure and V_v is the instantaneous volume.

The rate of change of work with respect to time is obtained by differentiating Eq. E.5 as follows:

$$\frac{dw}{dt} = p_v \, \frac{dV_v}{dt} \qquad \text{(E.6)}$$

Since the fluid is supplied to the cylinder from the source at a total temperature T_s, the rate of increase of the total energy of the fluid in the cylinder is given by:

$$\frac{dh}{dt} = T_s \, c_p \, \frac{dm_v}{dt} \qquad \text{(E.7)}$$

where c_p is the specific heat of the fluid at constant pressure. The equation of state for the fluid in the cylinder is

$$p_v V_v = m_v R T_v$$

Differentiating with respect to time,

$$\frac{d}{dt}(p_v V_v) = m_v R \frac{dT_v}{dt}$$

Thus,

$$V_v \frac{dp_v}{dt} + p_v \frac{dV_v}{dt} = m_v R \frac{dT_v}{dt} \qquad (E.8)$$

Substituting for $(m_v d T_v/dt)$ from Eq. E.8 into Eq. E.4

$$\frac{de}{dt} = \frac{c_v}{R}\left(p_v \frac{dV_v}{dt} + V_v \frac{dp}{dt}\right. \qquad (E.9)$$

Substituting Eqs. E.6, E.7, E.9 into Eq. E.2

$$T_s c_p \frac{dm_v}{dt} = p_v \frac{dV_v}{dt}\left(1 + \frac{c_v}{R}\right) + \frac{V_v c_v}{R}\frac{dp_c}{dt} \qquad (E.10)$$

Using the relations $R = c_p - c_v$, and $k = c_p/c_v$, Eq. E.10 can now be simplified to the following equation:

$$\frac{dp_v}{dt} = \frac{kRT_s}{V_v}\frac{dm_v}{dt} - \frac{kp_v}{V_v}\frac{dV_v}{dt} \qquad (E.11)$$

Referring to Fig. E.1, the volume of the cylinder at any instant of time is given by

$$V_v = V_{(0)} + A_c x \qquad (E.12)$$

where $V_{(0)}$ is the initial volume of the cylinder, A_c is the area of the cylinder and x is the displacement of the cylinder.

Differentiating Eq. E.12 with respect to time,

$$\frac{dV_v}{dt} = A_c \frac{dx}{dt} \qquad (E.13)$$

Substituting Eqs. E.12 and E.13 into Eq. E.11, the following equation for the charging of a cylinder is obtained:

$$\frac{dp_v}{dt} = \frac{kRT_s}{V_{(0)} + A_c x} \frac{dm_v}{dt} - \frac{kp_v A_c}{V_{(0)} + A_c x} \frac{dx}{dt} \qquad (E.14)$$

The equivalent of Eq. E.11 for the case of a constant volume is obtained by substituting $dV_v/dt = 0$ into Eq. E.11. Thus,

$$\left[\frac{dp_v}{dt}\right]_{\text{const.vol.}} = \frac{kRT_s}{V_v} \frac{dm_v}{dt} \qquad (E.15)$$

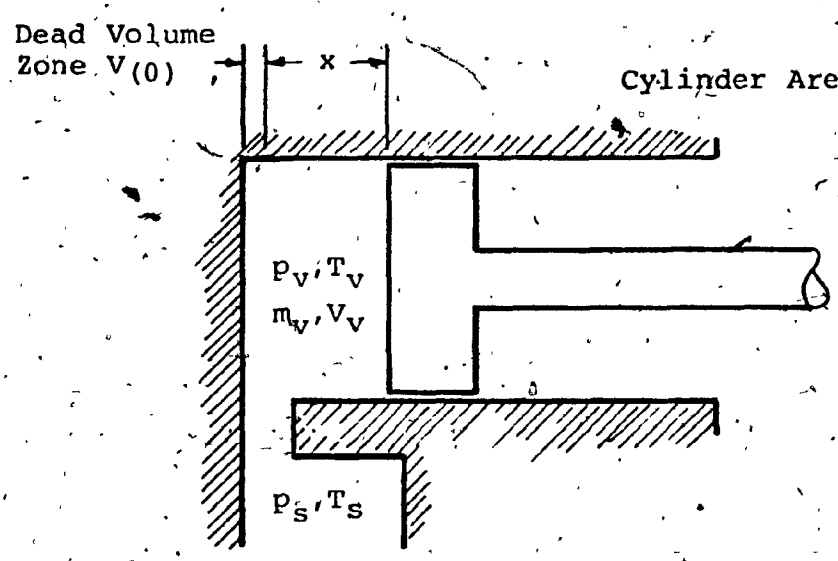

Fig. E.1: Schematic Diagram of a Cylinder.

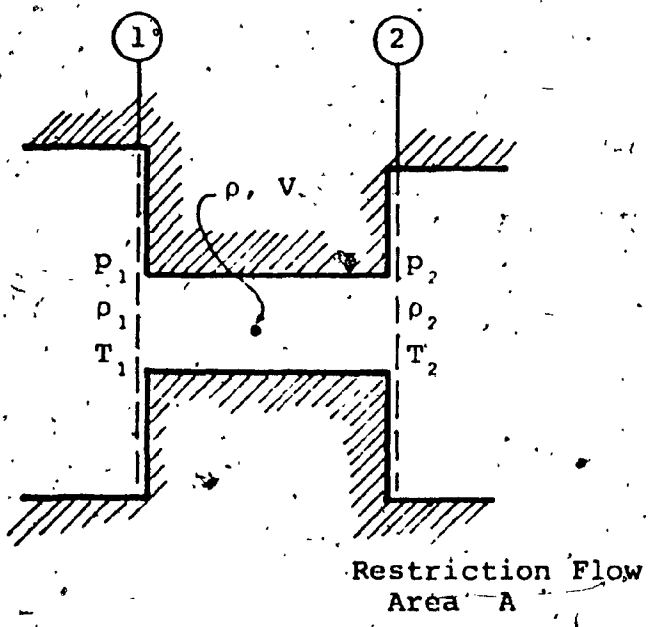

Fig. F.1: Schematic Diagram of the Flow Restriction.

APPENDIX F

EQUATION OF FLOW THROUGH A RESTRICTION

A restriction here is defined as a flow passage which offers resistance to flow, where the flow velocities are small (Mach number less than 0.3). In order to derive the flow equation, the following assumptions are made:

a) The flow has a Mach number less than 0.3, hence the equations for incompressible flow can be used for compressible flow, with less than 13% error [Section 3.3 Ref. 16]. The error decreases as the Mach number decreases.

b) The density change across the restriction is assumed to be linear with reference to the distance along the restriction ($d\rho/d\ell$ = constant, where x is the passage length).

Referring to Fig. F.1, the pressure drop across the restriction is given by:

$$\Delta P = P_1 - P_2 = C \rho \frac{V^2}{2} \qquad \text{[Eq. 5.5 Ref. 16]} \qquad (F.1)$$

where P_1 and P_2 are the pressures at Sections 1 and 2, C is a resistance factor, and ρ and V are the density and the velocity at a point intermediate to Sections 1 and 2 as shown in Fig. F.1.

Knowing the densities ρ_1 and ρ_2 at Sections 1 and 2 respectively, it follows from assumption (b) that,

$$\rho = (\rho_1 + \rho_2)/2 \qquad (F.2)$$

Combining the equation of state of a perfect gas, and Eq. F.2,

$$\rho = \frac{1}{2R}\left[\frac{P_1}{T_1} + \frac{P_2}{T_2}\right] \qquad (F.3)$$

where T_1 and T_2 are the temperature of the fluid at Sections 1 and 2 respectively.

The mass flow rate W through the restriction is given by:

$$W = \rho A V \qquad (F.4)$$

where A is the area of the restriction.

Substituting for V and ρ from Eqs. F.1 and F.3 in Eq. F.4, the mass flow rate through the restriction is given by:

$$W = \frac{AP_2}{\sqrt{CRT_2}}\sqrt{(p_r - 1)(p_r T_r + 1)} \qquad (F.5)$$

where

$$p_r = P_1/P_2, \text{ and } T_r = T_2/T_1$$

APPENDIX G

BLOCK TYPE FRICTION BRAKE USED IN THE EXPERIMENTAL SETUP

The block type friction brake utilized in the system analyzed is shown schematically in Fig. G.1, together with the flywheel. The brake consists of a lever fitted with an asbestos break pad which presses against the periphery of the flywheel disc.

The fulcrum of the lever is located on the tangent to the flywheel periphery at the point of contact with the brake pad. The lever is pressed against the flywheel by deadweights hanging from its end thus providing the brake force F_B. Referring to Fig. G.1, the normal force N_B at the point of contact between the brake pad and the flywheel is given by:

$$N_B = \left(\frac{a + b}{a}\right) \cdot F_B \qquad (G.1)$$

The tangential force F_{BT} acting on the flywheel rim is:

$$F_{BT} = \frac{(a + b) \cdot F_B \cdot \mu_4}{a} \qquad (G.2)$$

where μ_4 is the coefficient of friction between the materials of the flywheel disc and the brake pad. The torque imposed by the friction brake on the flywheel disc, is given by:

$$T_{FB} = K_1 \cdot F_B \cdot \mu_4 \qquad (G.3)$$

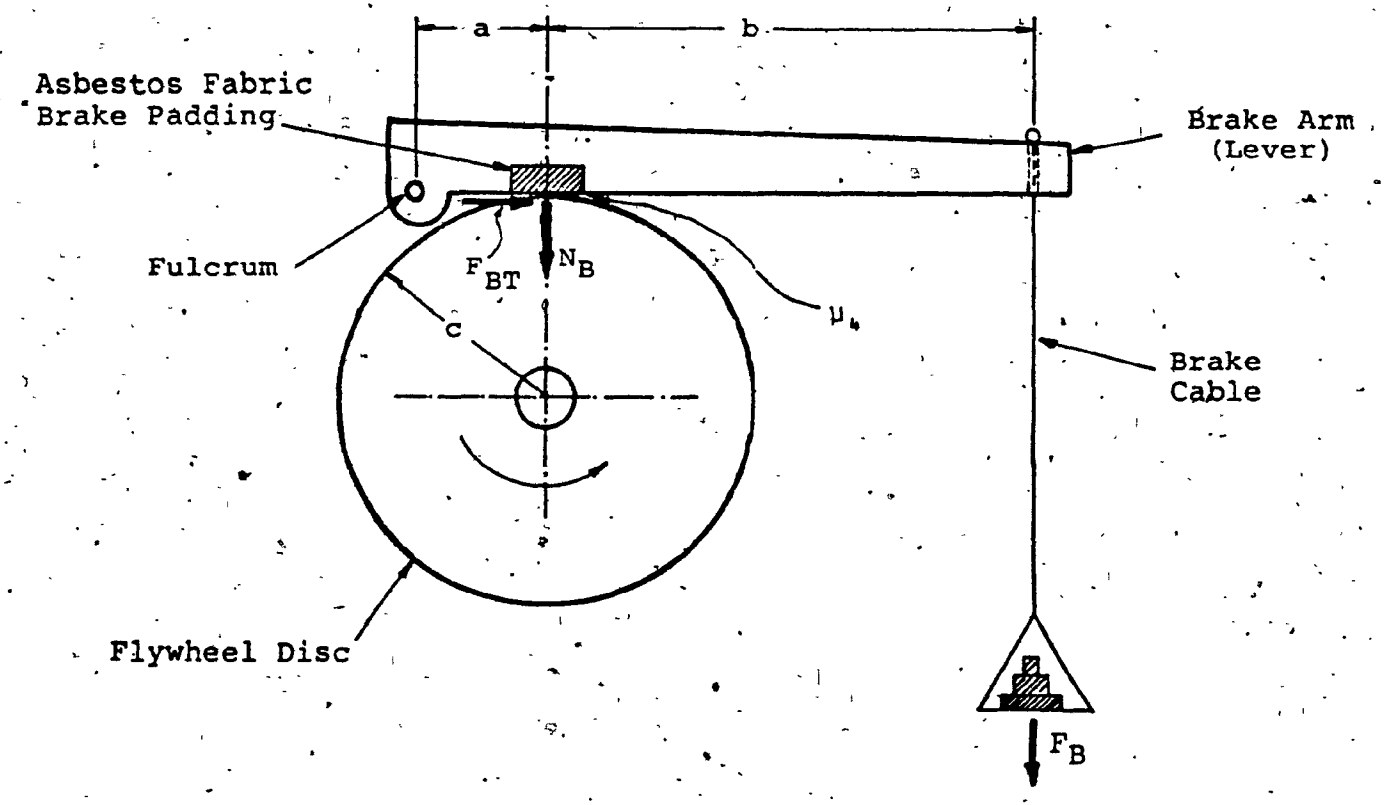

Fig. G.1: Block Type Friction Brake and Flywheel

where $K_1 = \frac{c(a + b)}{a}$ (G.3)

The coefficient of friction between the materials of the flywheel and the brake pad, was found experimentally using the setup shown schematically in Fig. G.2a. In the setup, a bobin wound with a cable was mounted at the end of the flywheel shaft with weights hanging from the end of its cable. By varying the weights acting on both the bobin and the brake arm, the flywheel was made to rotate at constant speeds, the latter having been measured using a stroboscope. The value of the torque imposed by the bobin on the flywheel (i.e. weight on bobin x bobin radius) was substituted together with the brake force in Eq. G.3 to find μ_4.

A plot of μ_4 versus the velocity of rotation of the flywheel is shown in Fig. G.2b. The value of the static coefficient of friction $\mu_{4(s)} = 0.38$ given in the figure was found to be in agreement with published coefficients of friction ranging between 0.35 and 0.4, for similar conditions [Section 3, Ref. 19]. The plot of Fig. G.2b was approximated by an exponentially decreasing function, having an upper limit $\mu_{4(s)}$ and a lower limit $\mu_{4(d)}$, as shown in the figure. The equation of this function is given by:

$$\mu_{4(s)} \geq \mu_{4(s)} \cdot e^{-K_2 \cdot |d\theta_4/dt|} \geq \mu_{4(d)}$$

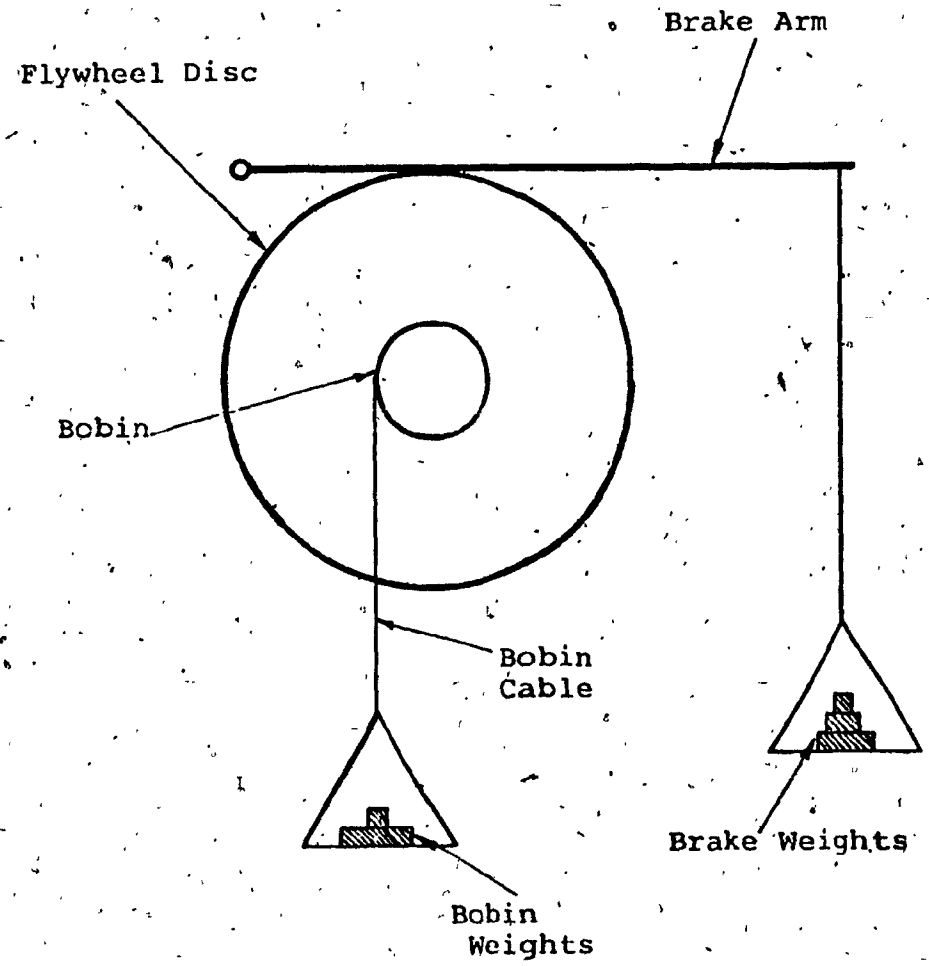

Fig. G.2a: Schematic of Experimental Setup for Measuring μ_4.

where $\mu_4(s) = 0.38$

$\mu_4(d) = 0.30$

and $K_2 = 0.1445$

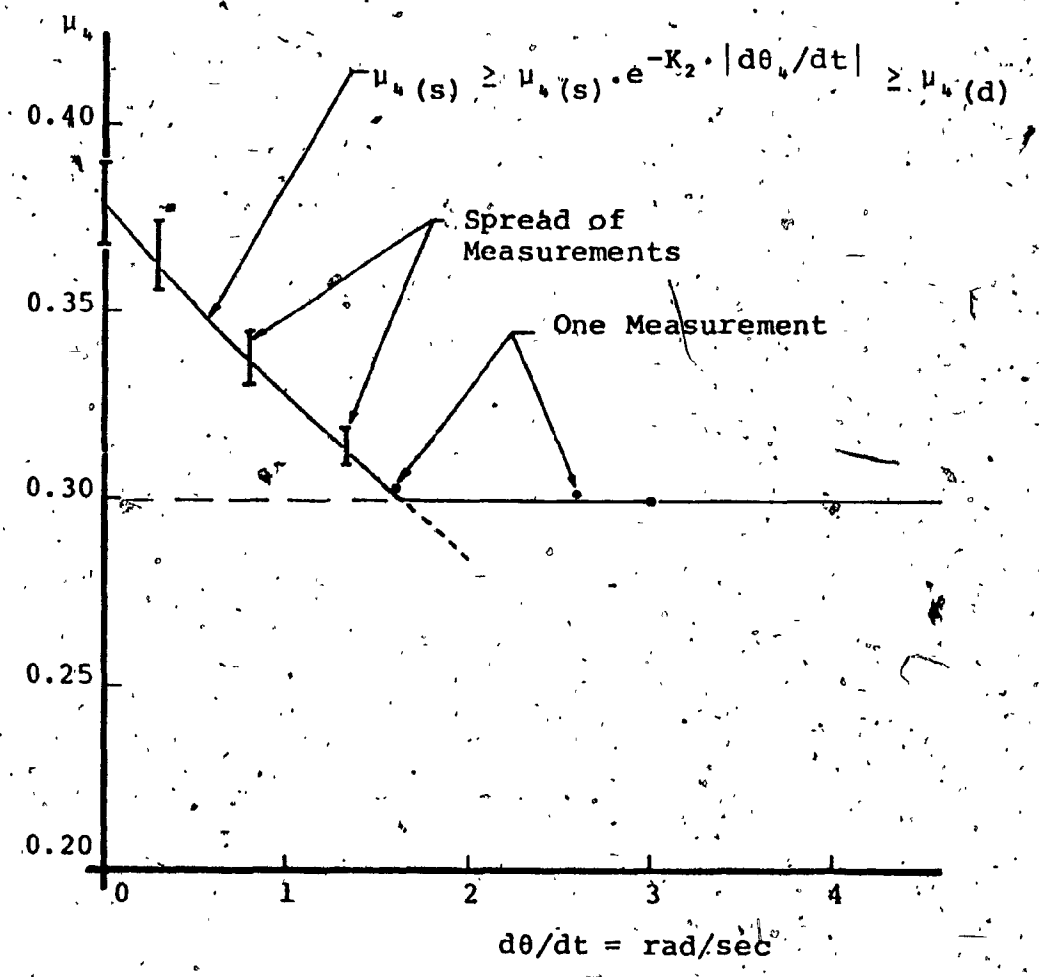

Fig. G.2b: Coefficient of Friction of Brake.

APPENDIX H

COMPUTER LISTING AND OUTPUT, AND EXPERIMENTAL TORQUE AND PRESSURE TRACES

This appendix contains the following:

1) System parameters, Table H.1

2) Dimensional, nondimensional, and initial conditions constants, Table H.2

3) Computer listing of the system equations, Table H.3

4) Computer output in nondimensional form, Figs. H.1a to H.1d

5) Computer output in dimensional form, Figs. H.2a to H.2d

6) Oscilloscope photographs of the experimental torque-time and pressure-time traces. Figs. H.3a to H.3d

TABLE H.1: SYSTEM PARAMETERS

Valve Parameters

$A_V = 0.0061 \text{ in}^2$

$\tau_V = 0.011 \text{ sec}$

$V_V = 0.7322 \text{ in}^3$

Connector Parameters

Length of connector = 6.0 in

Diameter of connector = 0.17 in

$c_L = 1.5$

Rotary Junction Parameters

$V_J = 3.1416 \text{ in}^3$

$c_J = 2$

Cylinder

$A_C = 0.7854 \text{ in}^2$

$V_{C(o)} = 0.0607 \text{ in}^3$

$A_D = 0.0123 \text{ in}^2$

$c_C = 4.48$

Motor-Load System: (Mechanical)

$f_{CS} = 3.5 \text{ lbf}$

$f_{CD} = 5 \text{ lbf}$

$K_S = 15 \text{ lbf/in}$

$S = 0.47 \text{ in}$

TABLE H.1: SYSTEM PARAMETERS (CONTINUED)

μ_2	= 0.28		(dynamic)
	= 0.35		(static)
J_M	= 1.352	lbm/in^1	
K_M	= 22580	lbf.in/rad	
η	= 0.0087	rad	
T_{FM}	= 5.5	lbf.in	
μ_1	= 0.25		(dynamic)
	= 0.35		(static)
α_s	= 0.2618	rad	
ε	= 0.05235	rad	
R_t	= 0.0625	in	
K_T	= 3435	lbf.in/rad	
K_L	= 7700	lbf.in/rad	
J_L	= 1.454	lbm.in^2	
K_E	= 2376	lbf.in/rad	[calculated as in Ref. 18]

TABLE H.2: DIMENSIONAL, NONDIMENSIONAL AND INITIAL CONDITIONS CONSTANTS

Dimensional Constants

$\beta_1 = 42.2260\ in^{-2}$

$\beta_2 = 0.0840\ in^{3}$

$\beta_3 = 0.2457\ in^{-3}$

Nondimensional Constants

$\Lambda_1 = 0.0147$

$\Lambda_2 = 1.0$

$\Lambda_3 = 3.8640$

$\Lambda_4 = 0.1148$

$\Lambda_5 = 0.1799$

$\Lambda_6 = 4.4370$

$\Lambda_7 = 0.6170$

$\Lambda_8 = 0.0335$

$\Lambda_9 = 3.8426$

$\Lambda_{10} = 0.0268$

$\Lambda_{11} = 0.7718$

$\Lambda_{12} = 1.3913$

$\Lambda_{13} = 0.7223$

$\Lambda_{14} = 9.3458$

$\Lambda_{15} = 43.8560$

$\Lambda_{16} = 567.5100$

$\Lambda_{17} = 1.0$

$\Lambda_{18} = 0.1557$

TABLE H.2: DIMENSIONAL, NONDIMENSIONAL AND INITIAL CONDITIONS CONSTANTS (CONTINUED)

$\Lambda_{19} = 10.2203$

$\Lambda_{20} = 3.2407$

$\Lambda_{21} = 0.1448$

Initial Conditions Constants

$m^*_{V(0)} = 0.02305$

$m^*_{L(0)} = 0.00429$

$m^*_{J(0)} = 0.09891$

$m^*_{C(0)} = 0.00191$

$p^*_{a(0)} = p^*_{b(0)} = p^*_{c(0)} = p^*_{d(0)} = 0.12816$

$\theta^*_{1(0)} = \theta^*_{2(0)} = \theta^*_{3(0)} = \theta^*_{4(0)} = 0.19996$

TABLE H.3: COMPUTER LISTING OF THE SYSTEM EQUATIONS

```
                ***MIMIC SOURCE-LANGUAGE PROGRAM***
                VERSION 1  10/01/68  MOD LEVEL 0000

PROGRAM MOTOR SIMULATES THE PNEUMATIC STEPPING MOTOR
WHEN DRIVING A RESISTIVE INERTIVE LOAD
-------------------------------------------------
-------------------------------------------------
.
.
.
PARAMETERS FOR PROGRAM ACCURACY
-------------------------------
                CON(FIXD)
.
PARAMETERS FOR OPERATING CONDITIONS
-----------------------------------
PS=OPERATING PRESSURE,TS=AMBIENT TEMPERATURE,PATMN=NON-
DIMENSIONAL ATMOSPHERIC PRESSURE
                CON(PS,TS,PATMN)
.
PARAMETERS FOR VALVE SPECIFICATIONS
-----------------------------------
ALFA1 TO ALFA5=NONDIMENSIONAL PARAMETERS FOR VALVE SPECIFIC-
ATIONS,MV0N=NONDIMENSIONAL MASS OF AIR INITIALLY IN THE
VALVE,TAWV=VALVE OPENING TIME
                CON(ALFA1,ALFA2,ALFA3)
                CON(ALFA4,ALFA5,MV0N)
                CON(TAWV)
.
PARAMETERS FOR LINE SPECIFICATIONS
----------------------------------
ALFA6 TO ALFA8=NONDIMENSIONAL PARAMETERS FOR VALVE SPECIFIC-
ATIONS,ML0N=NONDIMENSIONAL MASS OF AIR INITIALLY IN THE LINE
                CON(ALFA6,ALFA7,ALFA8)
                CON(ML0N)
.
PARAMETERS FOR ROTARY JUNCTION VOLUME SPECIFICATIONS
----------------------------------------------------
ALFA 9 TO ALFA11=NONDIMENSIONAL PARAMETERS FOR R.J.V.
SPECIFICATIONS,MJ0N=NONDIMENSIONAL MASS OF AIR INITIALLY
IN THE R.J.V.
                CON(ALFA9,ALFA10,ALFA11)
                CON(MJ0N)
```

```
*
PARAMETERS FOR CYLINDER SPECIFICATIONS
--------------------------------------
ALFA12 TO ALFA17=NONDIMENSIONAL PARAMETERS FOR THE CYLINDER
MCON=NONDIMENSIONAL MASS OF AIR INITIALLY IN THE CYLINDER
VOLT=INITIAL TOTAL VOLUME OF PNEUMATIC SYSTEM,AC=CYLINDER AREA
                  CON(ALFA12,ALFA13,ALFA14)
                  CON(ALFA15,ALFA16,ALFA17)
                  CON(MCON,VOLT,AC)

*
PARAMETERS FOR ROTOR SPECIFICATIONS
-----------------------------------
ALFA18 AND ALFA19=NONDIMENSIONAL PARAMETERS FOR ROTOR
FROD AND FROS=PISTON SEAL FRICTION DYNAMIC AND STATIC
FSI=INITIAL SPRING FORCE,KS=SPRING RATE,SG=PISTON ROD GUIDE
LENGTH,GFD=PISTON GUIDEFRICTION,JM=ROTOR INERTIA (JM/386.4)
KSH1=OUTPUT SHAFT STIFFNESS,BAKL=NONDIMENSIONAL BACKLASH ANGLE
TFM=OUTPUT SHAFT SEAL FRICTION
                  CON(ALFA18,ALFA19,FROD)
                  CON(FROS,FSI,KS)
                  CON(SG,GFD,JM)
                  CON(KSH1,BAKL,TFM)
*
PARAMETERS FOR CAM SPECIFICATIONS
---------------------------------
CFD=CAM FRICTION,RD=CAM DEDENDUM RADIUS,SP AND UP=STRAIGHT LINE
PART OF THE DRIVING PROFILE PARAMETERS,RESO=DRIVING PROFILE
ANGLE,OFSAN=NONDIMENSIONAL OFFSET ANGLE,CIRC=ANGLE OF THE END
OF THE STRAIGHT LINE PART OF THE PROFILE,CEE AND EL=CIRCULAR
PART OF THE DRIVING PROFILE PARAMETERS
                  CON(CFD,RD,SP)
                  CON(UP,RESO,OFSAN)
                  CON(CIRC,CEE,EL)
*
PARAMETERS FOR LOAD SPECIFICATIONS
----------------------------------
ALFA20 AND ALFA21=NONDIMENSIONAL PARAMETERS FOR LOAD
JL=LOAD INERTIA (JL/386.4),KSH2=TORQUE TRANSDUCER SHAFT STIFFNESS
KSH3=LOAD SHAFT STIFFNESS,BFS AND BFD=BRAKE FRICTION STATIC
AND DYNAMIC,KSHE=STIFFNESS OF EQUIVALENT LOAD SHAFT
OMEGAL=NATURAL FREQUENCY OF LOAD SYSTEM
                  CON(ALFA20,ALFA21,JL)
                  CON(KSH2,KSH3,BFS)
                  CON(BFD,KSHE,OMEGAL)
                  PAR(BFD)
*
*
*
INTEGRATION AND PRINTOUT STEP SIZE
----------------------------------
        TNOT      FSW(T,FALSE,TRUE,FALSE)
        DT        LSW(STOPN,.0005,.0001)
```

```
          DTMIN     .0001
          DTMAX     .0001
TNOT      TC        SQR(KSHE/JL)
          TAW       T*TC
.
.
VALVE EQUATIONS
---------------
          SSUBN     FSW(0.528-PAS,TRUE,FALSE,FALSE)
          AV        LIM(T/TAWV,0.0,1.0)
          PAS       PA
SSUBN     WSAZ1     EXP(.71429*LOG(PAS))
SSUBN     WSAZ2     SQR(1.0-EXP(.28571*LOG(PAS)))
SSUBN     WSAZ      WSAZ1*WSAZ2
          WSA       LSW(SSUBN,ALFA3*AV*WSAZ,ALFA2*AV)
          PA        INT(ALFA4*(WSA-WAB)*OMEGAL,PATMN)
          MV        INT(ALFA1*(WSA-WAB)*OMEGAL,MVON)
          TA        ALFA5*PA/MV
.
PNEUMATIC LINE EQUATIONS
------------------------
          PAB       PA/PB
          TBA       TB/TA
          WAB       ALFA6*PB*SQR((PAB-1.0)*(PAB*TBA+1.0))/SQR(TB)
          PB        INT(ALFA7*TA*(WAB-WBC)*OMEGAL,PATMN)
          ML        INT(ALFA1*(WAB-WBC)*OMEGAL,MLON)
          TB        ALFA8*PB/ML
.
ROTARY JUNCTION VOLUME EQUATIONS
--------------------------------
          PBC       PB/PC
          TCB       TC/TB
          WBC       ALFA9*PC*SQR((PBC-1.0)*(PBC*TCB+1.0))/SQR(TC)
          PC        INT(ALFA10*TB*(WBC-WCD)*OMEGAL,PATMN)
          MJ        INT(ALFA1*(WBC-WCD)*OMEGAL,MJON)
          TC        ALFA11*PC/MJ
          PRESS     (PC-PATMN)*PS
          PCG       PRESS/PS
.
MOTOR CYLINDER EQUATIONS
------------------------
          VC        MCON+(AC*RD)/VOLT
          PCD       PC/PD
          TDC       TD/TC
          WCD       ALFA12*PD*SQR((PCD-1.0)*(PCD*TDC+1.0))/SQR(TD)
          DPD1      TC*WCD/(ALFA13+ALFA14*RAD)
          DPD2      PD*RSTD/(ALFA15+ALFA16*RAC)
          PD        INT((DPD1-DPD2)*OMEGAL,PATMN)
          MC        INT(ALFA1*WCD*OMEGAL,MCON)
          TD        ALFA17*PD*VC/MC
          PRES      (PD-PATMN)*PS
```

```
*
TORQUE EQUATION FOR THE MOTOR (GYRATOR)
---------------------------------------
        R       RVAR/RD
        FOR     PS*AC*RD
        GAMMA   (PRES*AC-KS*RVAR-FC)*R/FOR
        S       SG/RD
        FC      LSW(PNMOV,FROD+FSI-KS*1.0,FROS+FSI-KS*1.0)
        T1      COS(AATAC)-CFD*SIN(AATAC)
        T2      SIN(AATAC)+CFD*COS(AATAC)
        T3      1.0+GFD*(2.0*R-2.0+S)/S
        TMB     LSW(STOPN,GAMMA*T1/(T2*T3)
        TM      LIM(TMB,0.0,TMB)
*
*
MOTOR DYNAMIC EQUATIONS
-----------------------
        STOPN   FSW(THE1-1.0,TRUE,FALSE,FALSE)
        STOP    NOT(STOPN)
        STAGN   FSW(DTHET1,FALSE,TRUE,FALSE)
        SWIT1   FSW(THETA1-1.0,TRUE,TRUE,FALSE)
        SWIT2   FSW(2DTHET,TRUE,FALSE,FALSE)
        SWIT3   FSW(THETA1-THETBK,FALSE,TRUE,TRUE)
        SWIT4   AND(STOPN,IOR(AND(SWIT1,SWIT2),AND(SWIT3,NOT(SWIT2))))
        THETBK  1.0+BAKL
        KSM     KSH1*X*RESO/FOR
        FRIC    LSW(STAGN,KSM,(DTHET1/ABS(DTHET1)*ABS(KSM)))
        TMF     LSW(STOPN,TM,FRIC)
        TFMA    LIM(TMF,-TFM,TFM)
        2DTHET  ALFA18*TM-ALFA19*X
        2DTHE1  ALFA18*(TM-TFMA)-ALFA19*X
        1DTHE1  LSW(STOPN,INT(2DTHE1*OMEGAL,0.0),0.0)
        THE1    INT(1DTHE1*OMEGAL,OFSAN)
        DTHET1  INT(2DTHE1*OMEGAL,0.0,SWIT4,TNOT)
        THETA1  INT(DTHET1*OMEGAL,OFSAN)
*
TORQUE TRANSDUCER EQUATION
--------------------------
 TNOT   KBEG    (KSH2+KSH3)*KSH1
 TNOT   KEND    KSH2*KSH3
        THETA2  (KBEG*THETA1+KEND*THETA4)/(KBEG+KEND)
        THETA3  (KSH2*THETA2+KSH3*THETA4)/(KSH2+KSH3)
*
LOAD SYSTEM EQUATIONS
---------------------
        ZERVE   FSW(DTHET4,FALSE,TRUE,FALSE)
        BFRIC   LIM(EXP(-ABS(OMEGAL*RESO*DTHET4)*.1545)*BFS,BFD,BFS)
        TLM     6.6666*BFRIC*BFO/FOR
        KSL     KSH3*Y*RESO/FOR
        TLI     LSW(ZERVE,KSL,(DTHET4/ABS(DTHET4)*ABS(KSL)))
        TL      LIM(TLI,-TLM,TLM)
        2DTHE4  ALFA20*Y-ALFA21*TL
```

```
          DTHET4    INT(2DTHE4*OMEGAL,0.0)
          THETA4    INT(DTHET4*OMEGAL,OFSAN)
*
*
PROGRAM SOLUTION ACCURACY DETERMINATION
---------------------------------------
          XY        THETA1-THETA2
          X1        XY*FIXD
          X2        FIX(X1)
          X         X2/FIXD
          ZZ        THETA2-THETA3
          Z1        ZZ*FIXD
          Z2        FIX(Z1)
          Z         Z2/FIXD
          YX        THETA3-THETA4
          Y1        YX*FIXD
          Y2        FIX(Y1)
          Y         Y2/FIXD
          TMES      KSH2*Z*RESQ
          TT        TMES/FOR
*
*
MATHEMATICAL RELATIONS
----------------------
          PNMOV     FSW(RSTD,FALSE,FALSE,TRUE)
          CIRT      FSW(ADIS-CIRC,FALSE,TRUE,TRUE)
          ADIS      THE1*RESQ
          1DADIS    OMEGAL*RESQ*1DTHE1
 STOPN    RAD       RVAR-RQ
          AATAC     LSW(STOPN,ATN(RVAR,RSQD),0.0)
 STOPN    RSD1      (UP*SIN(ADIS)+COS(ADIS))
 STOPN    RSD2      (UP*COS(ADIS)-SIN(ADIS))
 CIRT     EN        EL*COS(RESQ-ADIS)
 CIRT     EM        EL*SIN(RESQ-ADIS)
 CIRT     IY        SQR(CEC*CEE-EL*EL*SIN(RESQ-ADIS)*SIN(RESQ-ADIS))
 CIRT     QU        EL*EL*SIN(2,0*(RESQ-ADIS))/(2.0*IY)
 STOPN    RSQD      LSW(CIRT,EM+QU,SP*RSD1/(RSD2*RSD2))
          RSTD      LSW(STOPN,1DADIS*RSQD,0.0)
*
*
CAM DRIVING PROFILE EQUATION
----------------------------
 STOPN    RVAR      LSW(CIRT,EN+IY,SP/RSD2)
*
*
OUTPUT AND FINISH STATEMENTS
----------------------------
                    FIN(T,.08)
          APIS      THETA1*RESQ
                    PLO(TAH,TT,PEG,THETA1)
                    PLO(T,TMES,PRESS,APIS)
                    END
```

FUNCTION-LANGUAGE PROGRAM GENERATED

IFN	LCV	RESULT	FTN	A	B	C	D	E	F
1			CON	FIXD					
2			CON	PS	TS	PATMN			
3			CON	ALFA1	ALFA2	ALFA3			
4			CON	ALFA4	ALFA5	MVON			
5			CON	TAHV					
6			CON	ALFA6	ALFA7	ALFA8			
7			CON	MLON					
8			CON	ALFA9	ALFA10	ALFA11			
9			CON	MJON					
10			CON	ALFA12	ALFA13	ALFA14			
11			CON	ALFA15	ALFA16	ALFA17			
12			CON	MCON	VOLT	AC			
13			CON	ALFA18	ALFA19	FROD			
14			CON	FROS	FSI	KS			
15			CON	SG	GFO	JM			
16			CON	KSH1	BAKL	TFM			
17			CON	CFO	RD	SP			
18			CON	UP	RESO	OFSAN			
19			CON	CIRC	CEE	EL			
20			CON	ALFA20	ALFA21	JL			
21			CON	KSH2	KSH3	BFS			
22			CON	BFO	KSHE	OMEGAL			
23			PAR	BFO					
24		DTMIN	EQL	.0001					
25		DTMAX	EQL	.001					
26		(089)	MPY	AC	RD				
27		(090)	DIV	(089)	VOLT				
28		VC	ADD	MCON	(090)				
29		FOR	MPY	RD	PS	AC			
30		S	DIV	SG	RD				
31		(124)	ADD	FROD	FSI				
32		(125)	MPY	KS	1.0				
33		(126)	SUB	(124)	(125)				
34		(127)	ADD	FROS	FSI				
35		(128)	SUB	(127)	(125)				
36		THETBK	ADD	1.0	BAKL				
37		(169)	NEG	TFM					
38		(194)	ADD	KSH2	KSH3				
39		ZERVE	FSW	DTHET4	FALSE	TRUE	FALSE		
40		(197)	MPY	DTHET4	OMEGAL	RESO			
41		(198)	ABS	(197)					
42		(199)	NEG	(198)					
43		(200)	MPY	(199)	.1545				
44		(201)	EXP	(200)					
45		(202)	MPY	(201)	BFS				
46		BFRIC	LIM	(202)	BFO	BFS			

```
47                (204)    MPY   BFO      6.6666 BFRIC
48                TLM      DIV   (204)    FOR
49                (208)    ABS   DTHET4
50                (210)    DIV   DTHET4   (208)
51                (213)    NEG   TLM
52                (220)    MPY   DTHET4   OMEGAL
53                THETA4   INT   (220)    OFSAN
54                ADIS     MPY   THE1     RESO
55                         FIN   T        .08
56                APIS     MPY   THETA1   RESO
57                TNOT     FSW   T        FALSE   TRUE    FALSE
58   TNOT         (028)    DIV   KSHE     JL
59   TNOT         TC       SQR   (028)
60                TAW      MPY   T        TC
61                (033)    DIV   T        TAWV
62                AV       LIM   (033)    0.0     1.0
63                PAS      EQL   PA
64                (045)    MPY   ALFA2    AV
65                (052)    MPY   ALFA5    PA
66                TA       DIV   (052)    MV
67                PAB      DIV   PA       PB
68                (056)    SUB   PAB      1.0
69                (068)    MPY   ALFA8    PB
70                TB       DIV   (068)    ML
71                PBC      DIV   PB       PC
72                (072)    SUB   PBC      1.0
73                (084)    MPY   ALFA11   PC
74                TC       DIV   (084)    MJ
75                (086)    SUB   PC       PATMN
76                PRESS    MPY   (086)    PS
77                PCC      DIV   PRESS    PS
78                PCD      DIV   PC       PD
79                (094)    SUB   PCD      1.0
80                (112)    MPY   VC       ALFA17  PD
81                TD       DIV   (112)    MC
82                (114)    SUB   PD       PATMN
83                PRES     MPY   (114)    PS
84                (118)    MPY   PRES     AC
85                (146)    SUB   THE1     1.0
86                STOPN    FSW   (146)    TRUE    FALSE   FALSE
87                STOP     NOT   STOPN
88                STAGN    FSW   DTHET1   FALSE   TRUE    FALSE
89                (150)    SUB   THETA1   1.0
90                SWIT1    FSW   (150)    TRUE    TRUE    FALSE
91                (153)    SUB   THETA1   THETBK
92                SWIT3    FSW   (153)    FALSE   TRUE    TRUE
93                (163)    ABS   DTHET1
94                (165)    DIV   DTHET1   (163)
95                1DTHE1   LSW   STOPN    (178)   0.0
96                (180)    MPY   1DTHE1   OMEGAL
97                THE1     INT   (180)    OFSAN
98                (183)    MPY   DTHET1   OMEGAL
```

```
 99                THETA1    INT    (183)   OFSAN
100    TNOT       (185)     ADD    KSH2    KSH3
101    TNOT       KBEG      MPY    (185)   KSH1
102    TNOT       KEND      MPY    KSH2    KSH3
103               (188)      MPY    KBEG    THETA1
104               (189)      MAD    KEND    THETA4  (188)
105               (190)      ADD    KBEG    KEND
106               THETA2     DIV    (189)   (190)
107               (192)      MPY    KSH2    THETA2
108               (193)      MAD    KSH3    THETA4  (192)
109               THETA3     DIV    (193)   (194)
110               XY         SUB    THETA1  THETA2
111               X1         MPY    XY      FIXD
112               X2         FIX    X1
113               X          DIV    X2      FIXD
114               ZZ         SUB    THETA2  THETA3
115               Z1         MPY    ZZ      FIXD
116               Z2         FIX    Z1
117               Z          DIV    Z2      FIXD
118               YX         SUB    THETA3  THETA4
119               Y1         MPY    YX      FIXD
120               Y2         FIX    Y1
121               Y          DIV    Y2      FIXD
122               TMES       MPY    RESO    KSH2    Z
123               TT         DIV    THE     FOR
124               (237)      SUB    ADIS    CIRC
125               CIRT       FSW    (237)   FALSE   TRUE    TRUE
126               1DADIS     MPY    1DTHE1  OMEGAL  RESO
127    STOPN      (244)      SIN    ADIS
128    STOPN      (245)      COS    ADIS
129    STOPN      RSD1       MAD    (244)   UP      (245)
130    STOPN      (247)      MPY    UP      (245)
131    STOPN      RSD2       SUB    (247)   (244)
132    CIRT       (249)      SUB    RESO    ADIS
133    CIRT       (250)      COS    (249)
134    CIRT       EN         MPY    EL      (250)
135    CIRT       (252)      SIN    (249)
136    CIRT       EM         MPY    EL      (252)
137    CIRT       (254)      MPY    CEE     CEE
138    CIRT       (255)      MPY    (252)   (252)   EL      EL
139    CIRT       (256)      SUB    (254)   (255)
140    CIRT       IY         SQR    (256)
141    CIRT       (258)      MPY    2.0     (249)
142    CIRT       (259)      SIN    (258)
143    CIRT       (260)      MPY    2.0     IY
144    CIRT       (261)      MPY    (259)   EL      EL
145    CIRT       QU         DIV    (261)   (260)
146    STOPN      (263)      MPY    RSD2    RSD2
147    STOPN      (264)      ADD    EM      QU
148    STOPN      (265)      MPY    SP      RSD1
149    STOPN      (266)      DIV    (265)   (263)
150    STOPN      RSQD       LSH    CIRT    (264)   (266)
```

```
151                (268)    MPY    1DADIS  RSQD
152                RSTD     LSW    STOPN   (268)   0.0
153     STOPN      (270)    ADD    EN      IY
154     STOPN      (271)    DIV    SP      RSD2
155     STOPN      RVAR     LSW    CIRT    (270)   (271)
156                DT       LSW    STOPN   .0005   .0001
157                (031)    SUB    0.528   PAS
158                SSUBN    FSW    (031)   TRUE    FALSE   FALSE
159     SSUBN      (036)    LOG    PAS
160     SSUBN      (037)    MPY    .71429  (036)
161     SSUBN      WSAZ1    EXP    (037)
162     SSUBN      (039)    MPY    .28571  (036)
163     SSUBN      (040)    EXP    (039)
164     SSUBN      (041)    SUB    1.0     (040)
165     SSUBN      WSAZ2    SQR    (041)
166     SSUBN      WSAZ     MPY    WSAZ1   WSAZ2
167                (044)    MPY    WSAZ    ALFA3   AV
168                WSA      LSW    SSUBN   (044)   (045)
169                TBA      DIV    TB      TA
170                (057)    MAD    TBA     PAB     1.0
171                (058)    MPY    (056)   (057)
172                (059)    SQR    (058)
173                (060)    SQR    TB
174                (061)    MPY    (059)   ALFA6   PB
175                WAB      DIV    (061)   (060)
176                TCB      DIV    TC      TB
177                (073)    MAD    TCB     PBC     1.0
178                (074)    MPY    (072)   (073)
179                (075)    SQR    (074)
180                (076)    SQR    TC
181                (077)    MPY    (075)   ALFA9   PC
182                WBC      DIV    (077)   (076)
183                TDC      DIV    TD      TC
184                (095)    MAD    TDC     PCD     1.0
185                (096)    MPY    (094)   (095)
186                (097)    SQR    (096)
187                (098)    SQR    TD
188                (099)    MPY    (097)   ALFA12  PD
189                WCD      DIV    (099)   (098)
190                (102)    MPY    TC      WCD
191                (105)    MPY    PD      RSTD
192                (110)    MPY    OMEGAL  ALFA1   WCD
193                MC       INT    (110)   MCDN
194                R        DIV    RVAR    RD
195                (135)    MPY    2.0     R
196                (136)    SUB    (135)   2.0
197                (137)    ADD    (136)   S
198                (138)    MPY    GFD     (137)
199                (139)    DIV    (138)   S
200                T3       ADD    1.0     (139)
201                (161)    MPY    RESO    KSH1    X
202                KSM      DIV    (161)   FOR
```

```
203             (164)   ABS     KSM
204             (166)   MPY     (165)   (164)
205             FRIC    LSW     STAGN   KSM     (166)
206             (172)   MPY     ALFA19  X
207             (206)   MPY     RESO    KSM3    Y
208             KSL     DIV     (206)   FOR
209             (209)   ABS     KSL
210             (211)   MPY     (210)   (209)
211             TLI     LSW     ZERVE   KSL     (211)
212             TL      LIM     TLI     (213)   TLM
213             (215)   MPY     ALFA20  Y
214             (216)   MPY     ALFA21  TL
215             2DTHE4  SUB     (215)   (216)
216             (218)   MPY     2DTHE4  OMEGAL
217             DTHET4  INT     (218)   0.0
218             PNMOV   FSW     RSTD    FALSE   FALSE   TRUE
219     STOPN   RAD     SUB     RVAR    RD
220             (242)   ATN     RVAR    RSQD
221             AATAC   LSW     STOPN   (242)   0.0
222             (047)   SUB     WSA     WAB
223             (048)   MPY     OMEGAL  ALFA4   (047)
224             PA      INT     (048)   PATMN
225             (050)   MPY     OMEGAL  ALFA1   (047)
226             MV      INT     (050)   MVON
227             (063)   SUB     WAB     WBC
228             (064)   MPY     OMEGAL  (063)   ALFA7   TA
229             PB      INT     (064)   PATMN
230             (066)   MPY     OMEGAL  ALFA1   (063)
231             MJ      INT     (066)   MJON
232             (079)   SUB     WBC     WCD
233             (080)   MPY     OMEGAL  (079)   ALFA10  TB
234             PC      INT     (080)   PATMN
235             (082)   MPY     OMEGAL  ALFA1   (079)
236             MJ      INT     (082)   MJON
237             (101)   MAD     ALFA14  RAD     ALFA13
238             DPD1    DIV     (102)   (101)
239             (104)   MAD     ALFA16  RAD     ALFA15
240             DPD2    DIV     (105)   (104)
241             (107)   SUB     DPD1    DPD2
242             (108)   MPY     (107)   OMEGAL
243             PD      INT     (108)   PATMN
244             FC      LSW     PNMOV   (126)   (128)
245             (130)   COS     AATAC
246             (131)   SIN     AATAC
247             (132)   MPY     CFD     (131)
248             T1      SUB     (130)   (132)
249             T2      MAD     CFD     (130)   (131)
250             (141)   MPY     T2      T3
251             (119)   MAD     RVAR    KS      FC
252             (120)   SUB     (118)   (119)
253             (121)   MPY     (120)   R
254             GAMMA   DIV     (121)   FOR
```

```
255             (142)     MPY    GAMMA    T1
256             (143)     DIV    (142)    (141)
257             TMB       LSW    STOPN    (143)
258             TM        LIM    TMB      0.0      TMB
259             TMF       LSW    STOPN    TM       FRIC
260             TFMA      LIM    TMF      (169)    TFM
261             (171)     MPY    ALFA18   TM
262             2DTHET    SUB    (171)    (172)
263             (174)     SUB    TM       TFMA
264             (175)     MPY    ALFA18   (174)
265             2DTHE1    SUB    (175)    (172)
266             (177)     MPY    2DTHE1   OMEGAL
267             (178)     INT    (177)    0.0
268             SWIT2     FSW    2DTHET   TRUE     FALSE    FALSE
269             (155)     AND    SWIT1    SWIT2
270             (156)     NOT    SWIT2
271             (157)     AND    SWIT3    (156)
272             (158)     IOR    (155)    (157)
273             SWIT4     AND    STOP     (158)
274             DTHET1    INT    (177)    0.0      SWIT4    TNOT
275                       PLO    TAW      TT       PCG      THETA1
276                       PLO    T        TMES     PRESS    APIS
277                       END
```

FIXD
1.00000E+12

PS	TS	PATMN
1.14700E+02	5.28000E+02	1.28160E-01

ALFA1	ALFA2	ALFA3
1.47500E-02	1.00000E+00	3.86390E+00

ALFA4	ALFA5	MVON
1.14770E-01	1.79870E-01	2.30500E-02

TAWV
1.10000E-02

ALFA6	ALFA7	ALFA8
4.43700E+00	6.17070E-01	3.34600E-02

MLON
1.29000E-03

ALFA9 3.84260E+00	ALFA10 2.67500E-02	ALFA11 7.71760E-01
MJON 9.89100E-02		
ALFA12 1.39130E+00	ALFA13 7.22290E-01	ALFA14 9.34580E+00
ALFA15 4.38560E+01	ALFA16 5.67510E+02	ALFA17 1.00000E+00
MCCN 1.91000E-03	VOLT 4.07070E+00	AC 7.85400E-01
ALFA18 1.55750E-01	ALFA19 1.02200E+01	FROD 1.50000E+00
FROS 3.00000E+00	FSI 2.00000E+00	KS 1.50000E+01
SG 4.70000E-01	GFD 2.80000E-01	JM 3.50000E-03
KSH1 2.25800E+04	BAKL 3.32300E-02	TFM 6.10500E-02
CFD 2.50000E-01	RD 1.00000E+00	SP 1.28138E+00
UP 1.28138E+00	RESO 2.61800E-01	OFSAN 1.99960E-01
CIRC 2.22570E-01	CEE 6.25000E-02	EL 1.20520E+00
ALFA20 3.24070E+00	ALFA21 1.44820E-01	JL 3.76400E-03

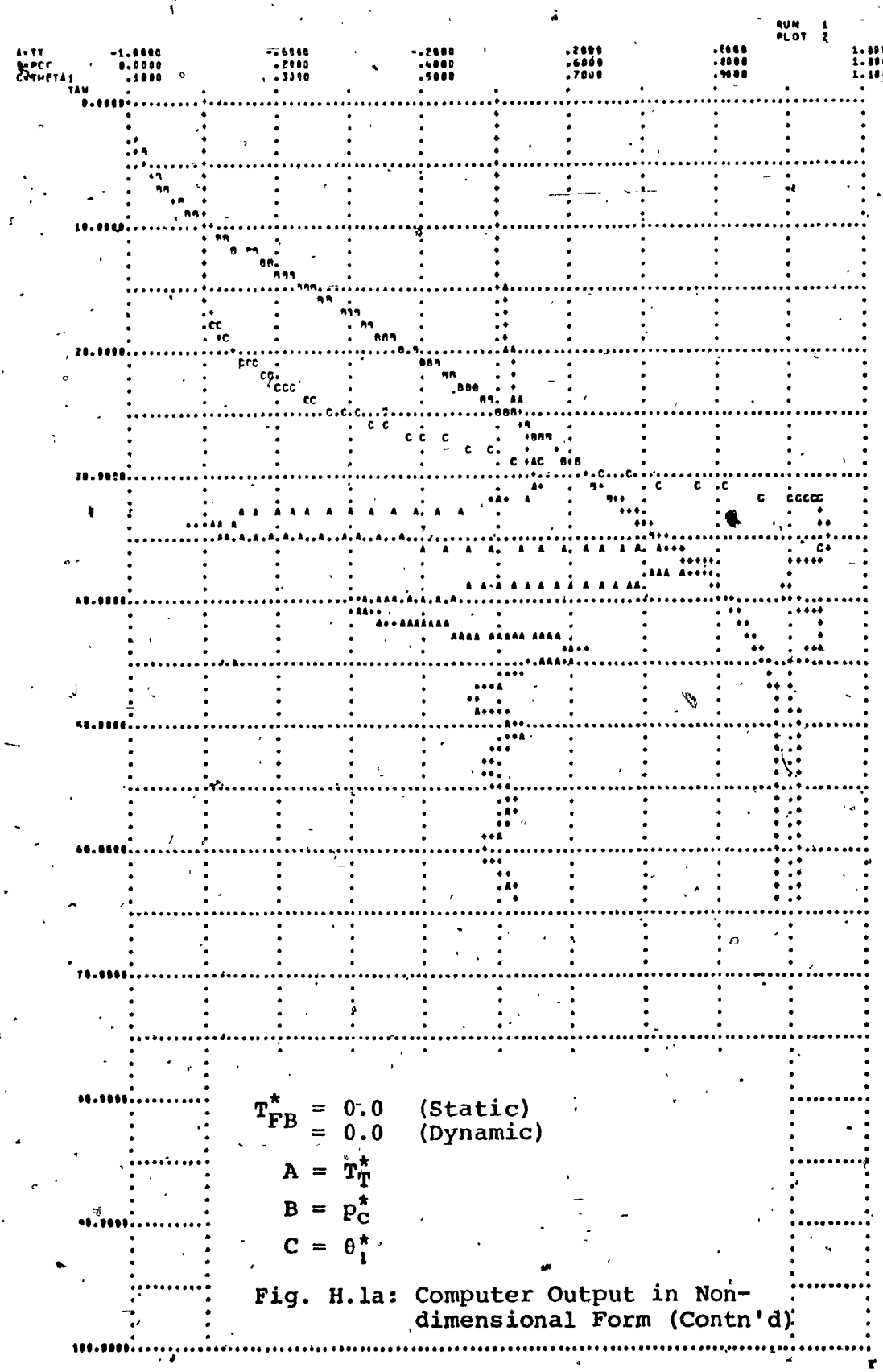

T^*_{FB} = 0.0 (Static)
= 0.0 (Dynamic)

A = T^*_T

B = p^*_C

C = θ^*_1

Fig. H.1a: Computer Output in Non-dimensional Form (Contn'd)

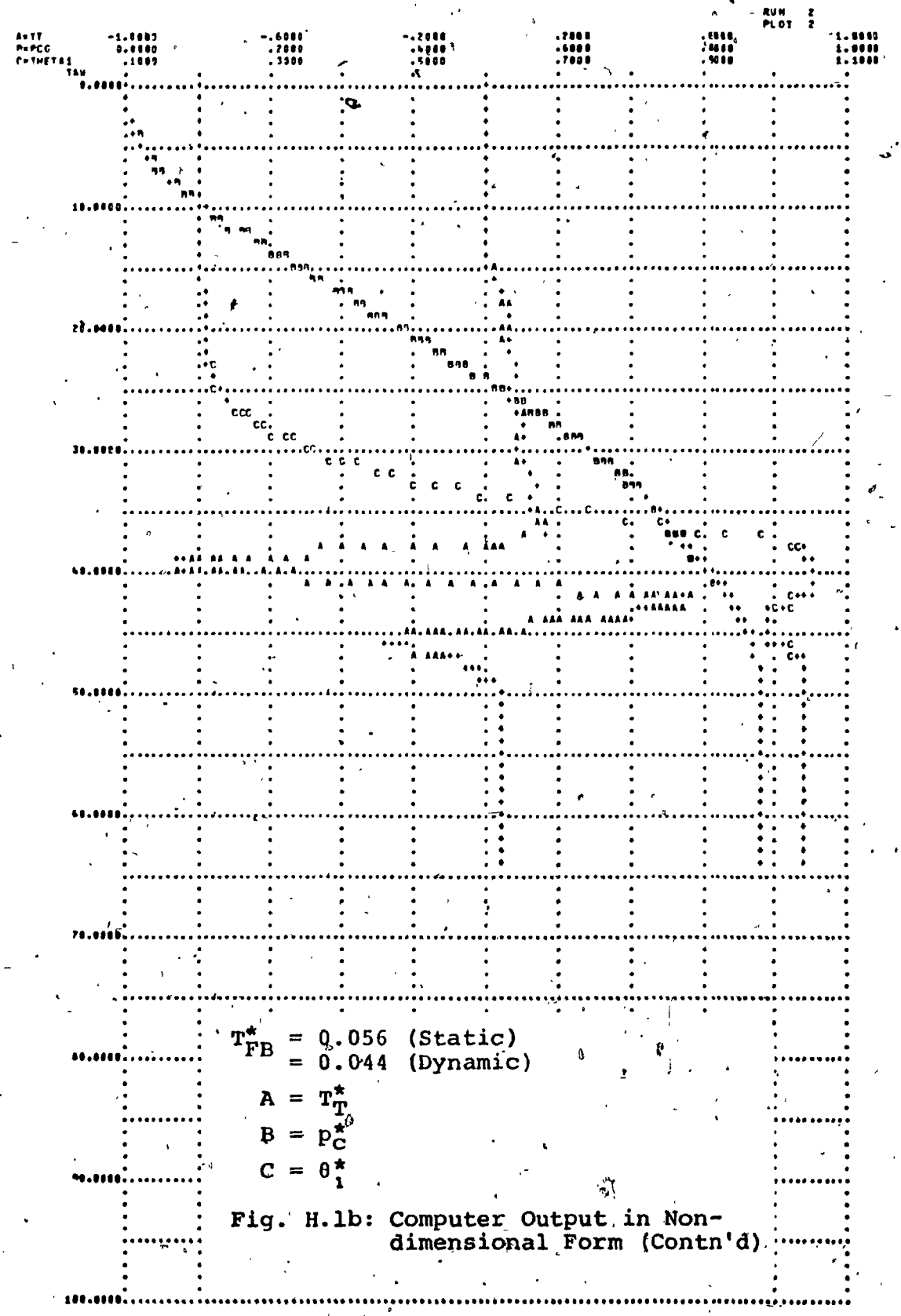

T^*_{FB} = 0.056 (Static)
= 0.044 (Dynamic)

A = T^*_T

B = p^*_C

C = θ^*_1

Fig. H.1b: Computer Output in Non-dimensional Form (Contn'd)

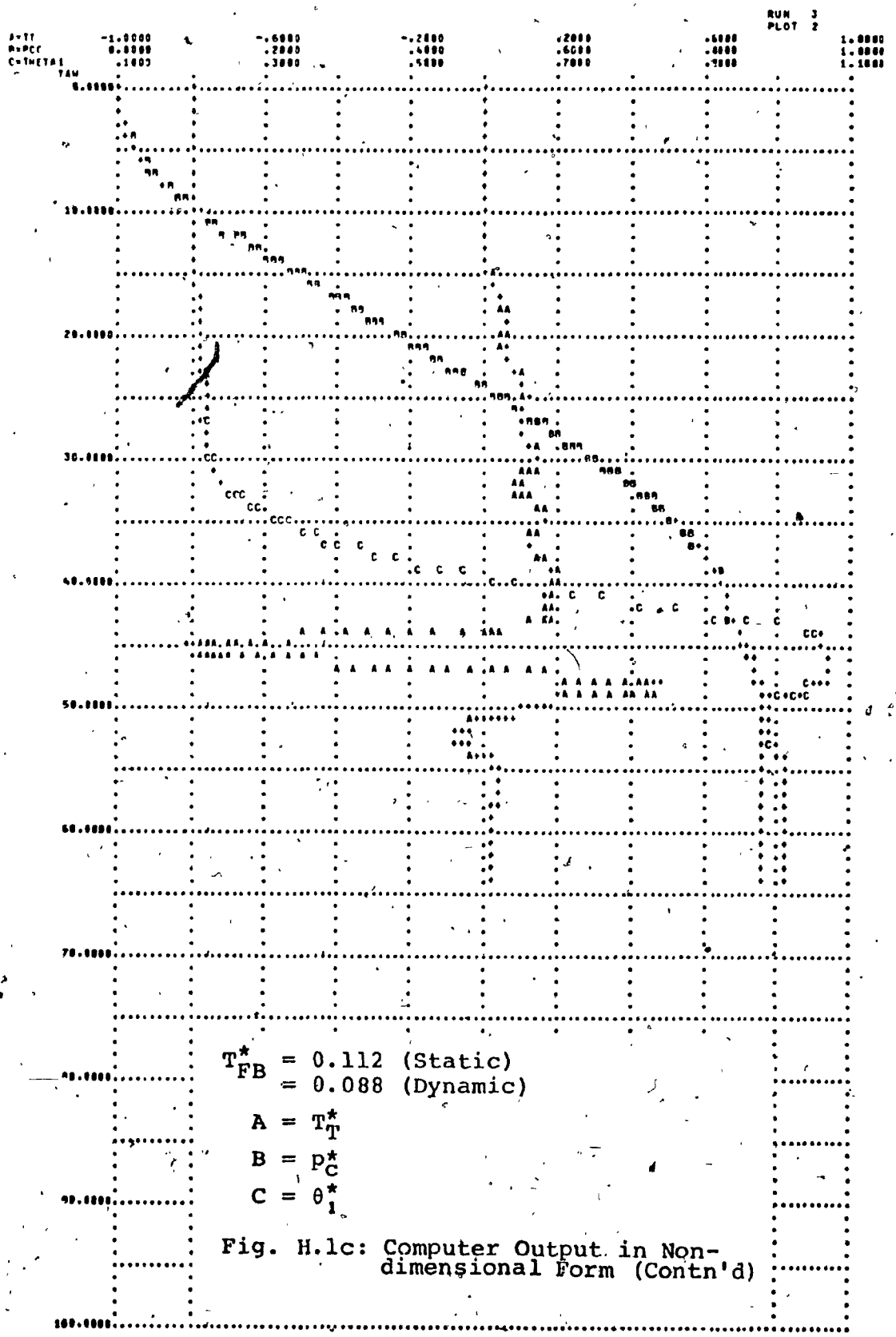

T^*_{FB} = 0.112 (Static)
= 0.088 (Dynamic)

$A = T^*_T$

$B = p^*_C$

$C = \theta^*_1$

Fig. H.1c: Computer Output in Non-dimensional Form (Contn'd)

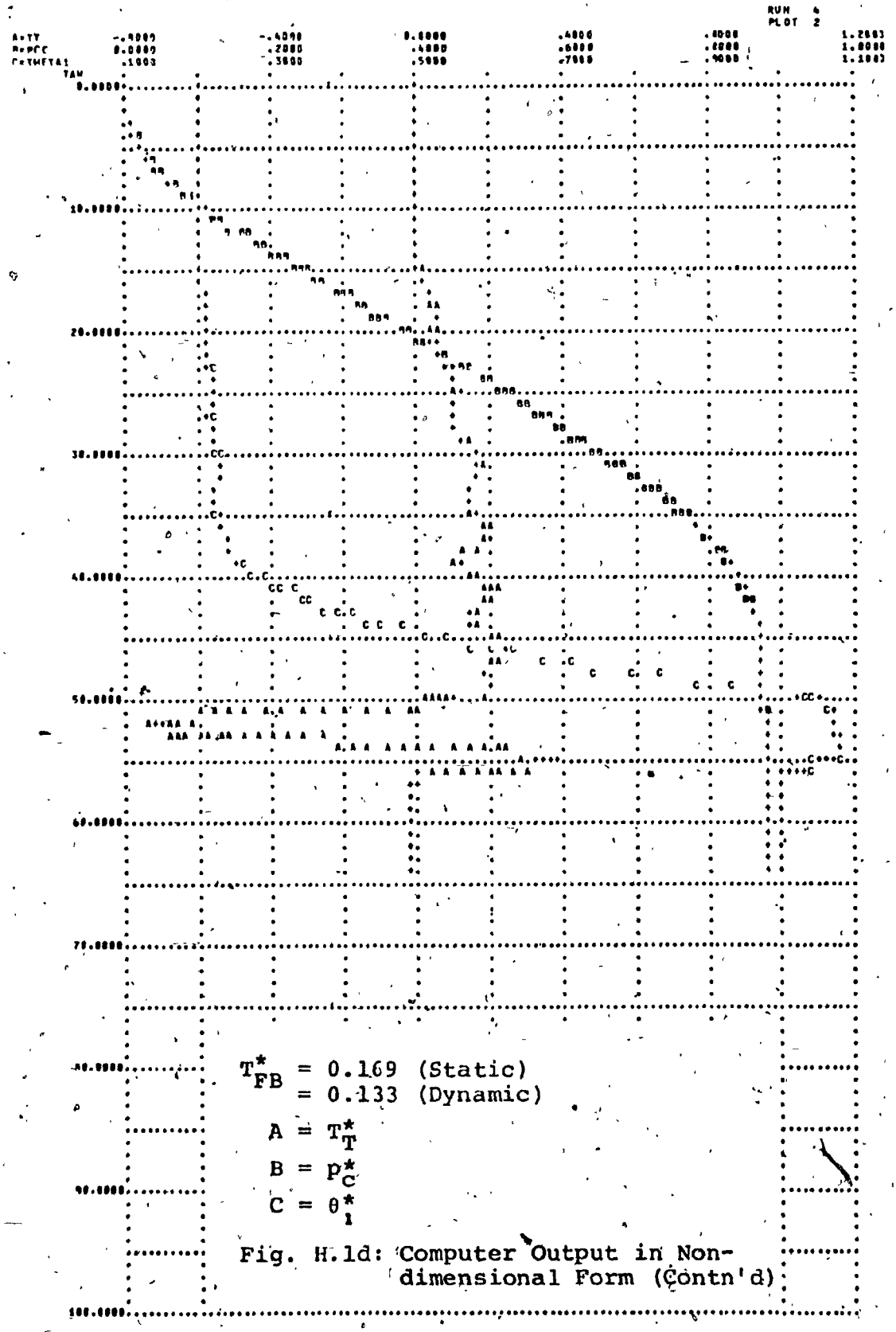

T^*_{FB} = 0.169 (Static)
= 0.133 (Dynamic)

A = T^*_T

B = p^*_C

C = θ^*_1

Fig. H.1d: Computer Output in Non-dimensional Form (Contn'd)

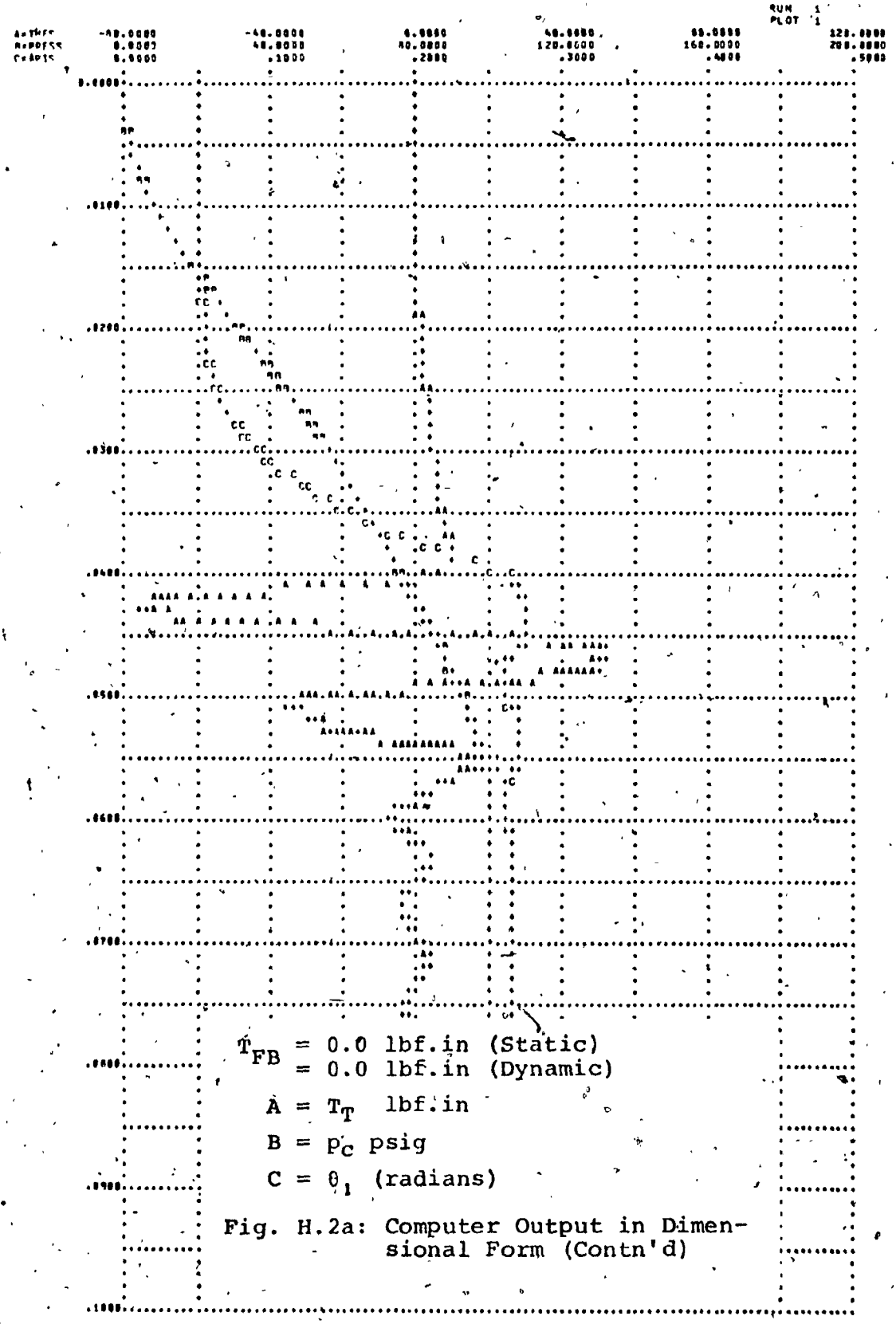

T_{FB} = 0.0 lbf.in (Static)
= 0.0 lbf.in (Dynamic)

A = T_T lbf.in

B = p_c psig

C = θ_1 (radians)

Fig. H.2a: Computer Output in Dimensional Form (Contn'd)

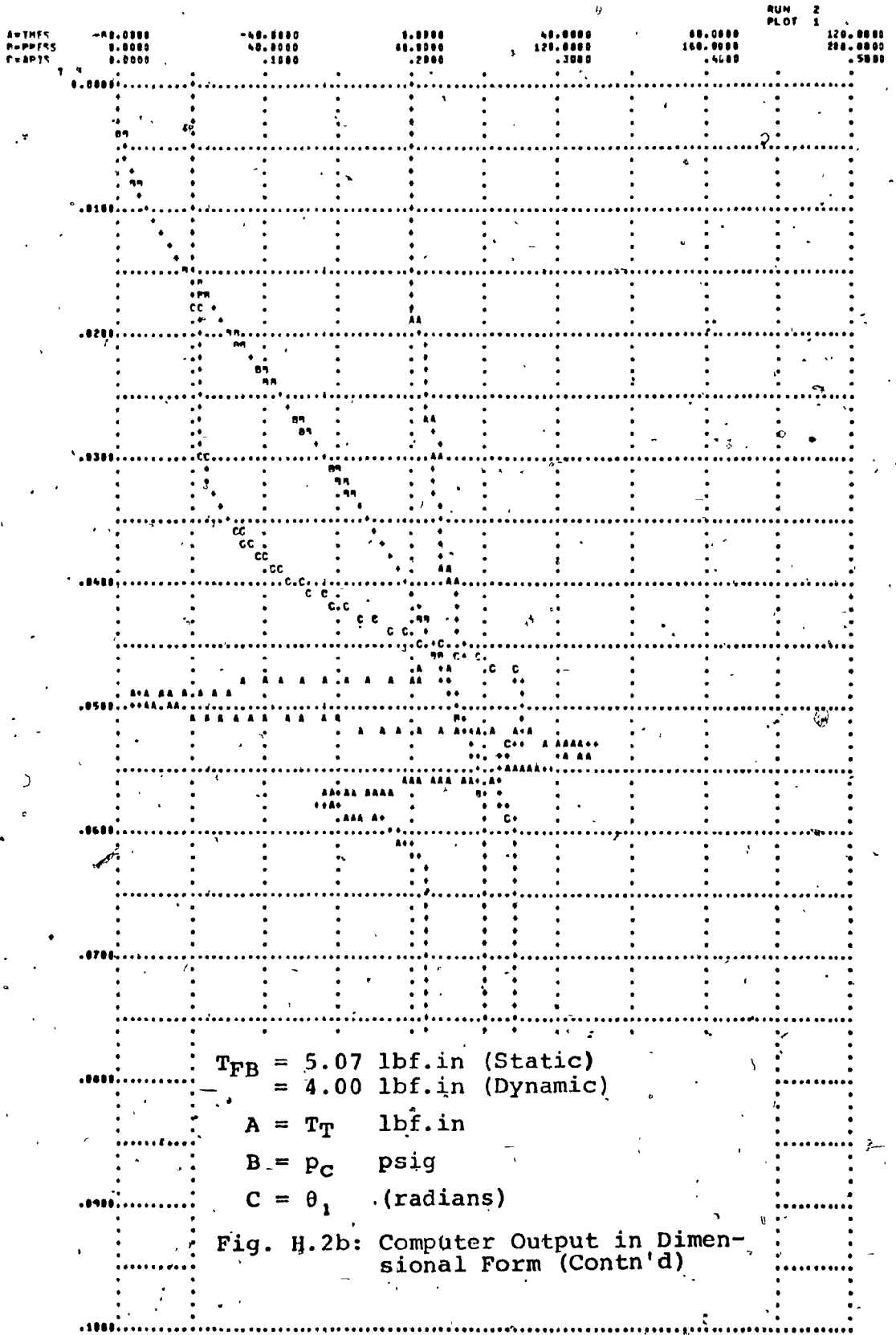

T_{FB} = 5.07 lbf.in (Static)
= 4.00 lbf.in (Dynamic)

A = T_T lbf.in

B = p_c psig

C = θ_1 (radians)

Fig. H.2b: Computer Output in Dimensional Form (Contn'd)

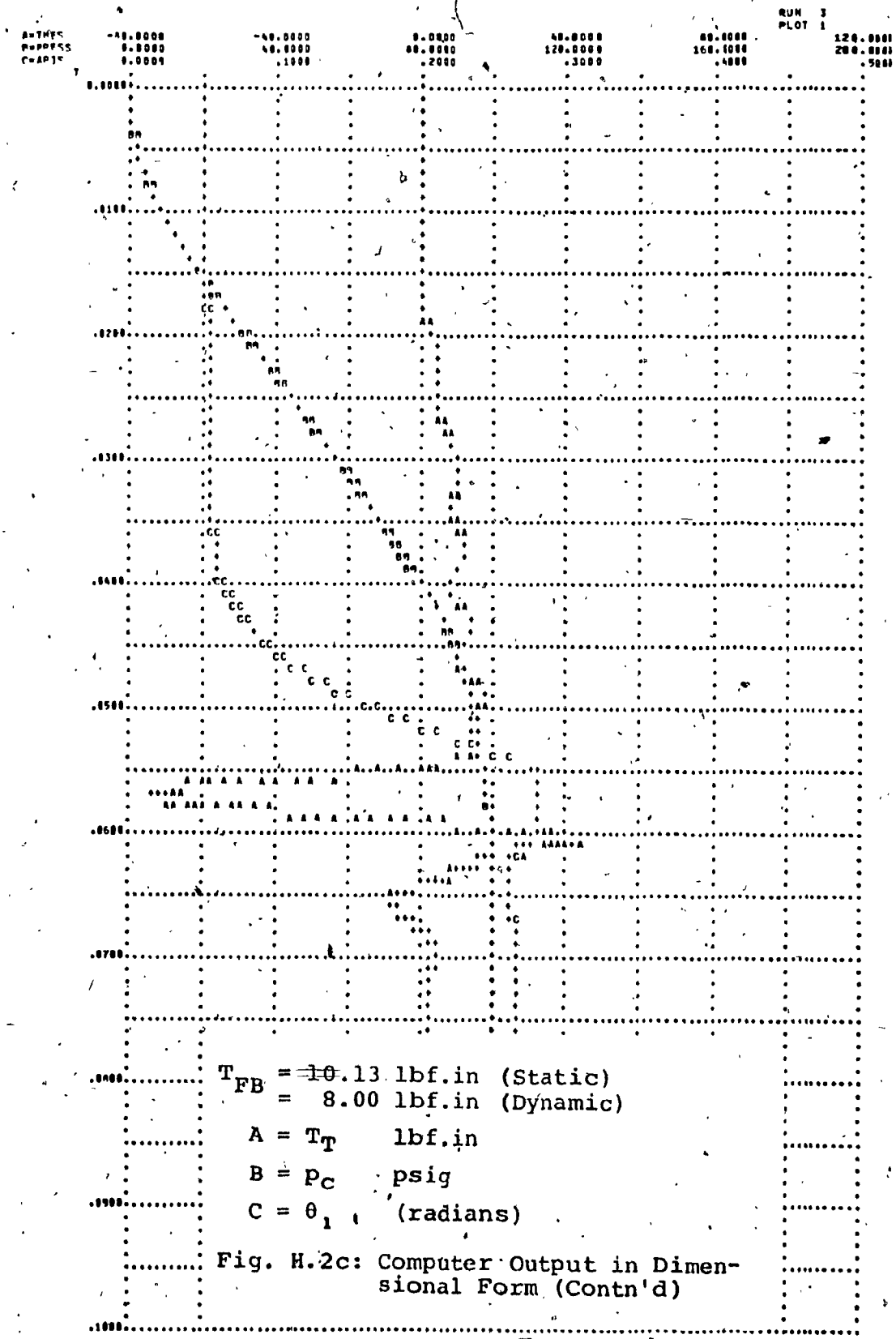

T_{FB} = ~~10~~.13 lbf.in (Static)
= 8.00 lbf.in (Dynamic)

A = T_T lbf.in

B = p_C psig

C = θ_1 (radians)

Fig. H.2c: Computer Output in Dimensional Form (Contn'd)

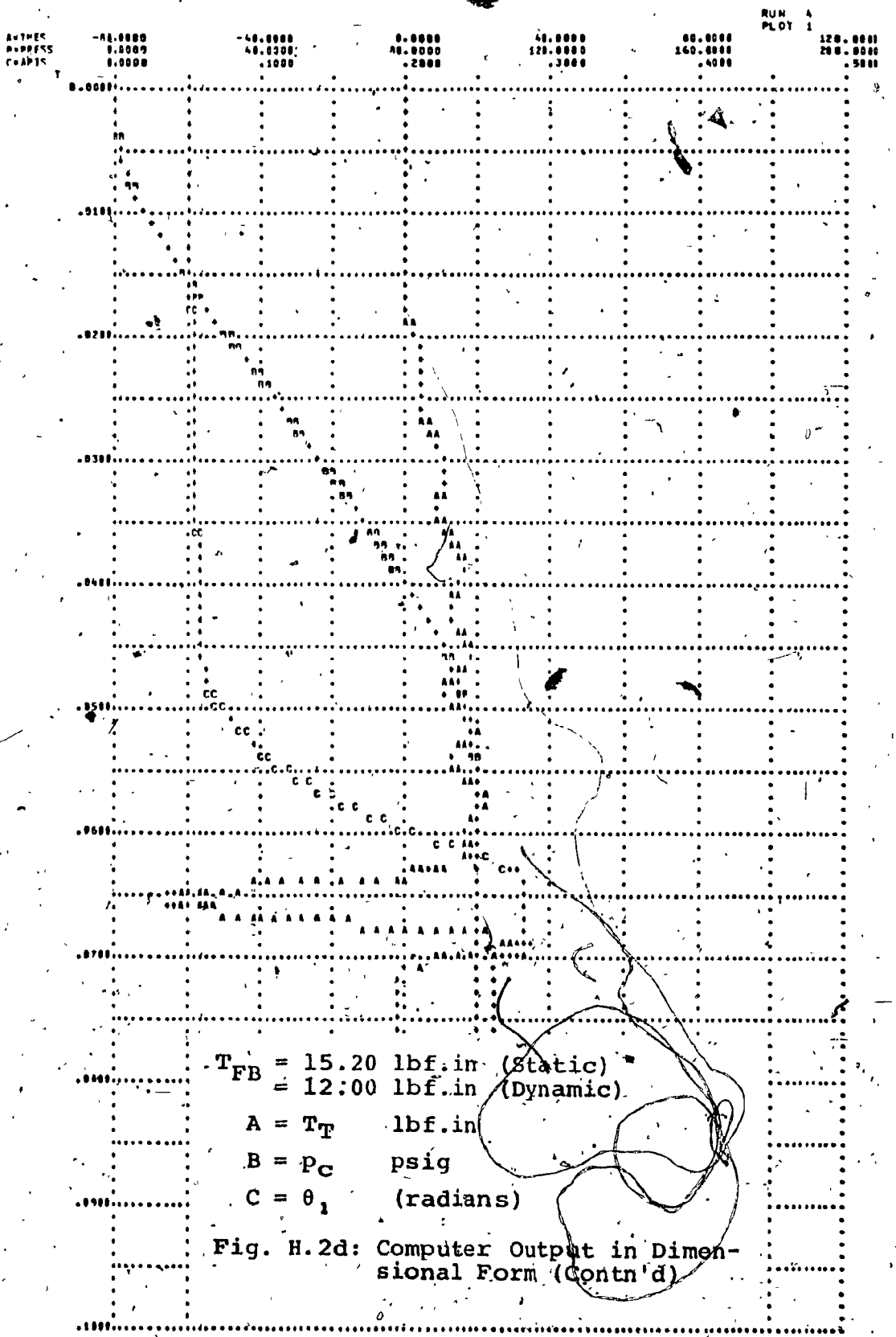

T_{FB} = 15.20 lbf.in (Static)
= 12.00 lbf.in (Dynamic)

A = T_T lbf.in

B = p_c psig

C = θ_1 (radians)

Fig. H.2d: Computer Output in Dimensional Form (Contn'd)

Friction Brake Torque = 0.0 lbf.in (Static)
= 0.0 lbf.in (Dynamic)

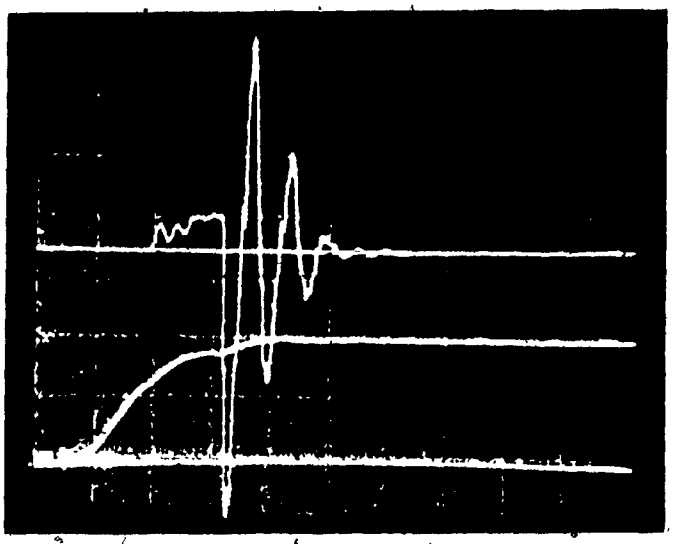

Upper Trace : Torque Transducer Output
(Scale: 14.7 lbf.in/div.)

Lower Trace : Pressure in the Rotary Junction Volume
(Scale: 50 $\frac{lbf}{in^2}$/div.)

Horizontal Axis: Time (Scale: 20 msec/div.)

Fig. H.3a: Oscilloscope Photographs of the Experimental Torque-Time and Pressure-Time Traces (Contn'd).

Friction Brake Torque = 5.07 lbf.in (Static)
= 4.00 lbf.in (Dynamic)

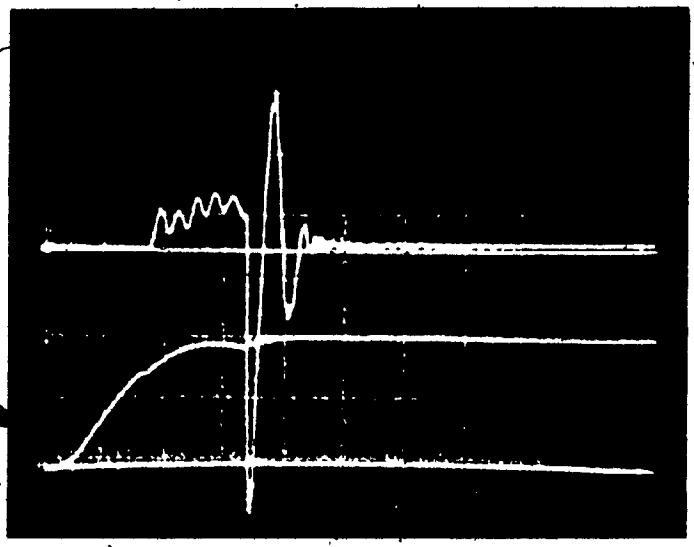

Upper Trace : Torque Transducer Output
(Scale: 14.7 lbf.in/div.)

Lower Trace : Pressure in the Rotary Junction Volume
(Scale: 50 $\frac{lbf}{in^2}$/div.)

Horizontal Axis: Time (Scale: 20 msec/div.)

Fig. H.3b: Oscilloscope Photographs of the Experimental Torque-Time and Pressure-Time Traces (Contn'd).

Friction Brake Torque = 10.13 lbf.in (Static)
= 8.00 lbf.in (Dynamic)

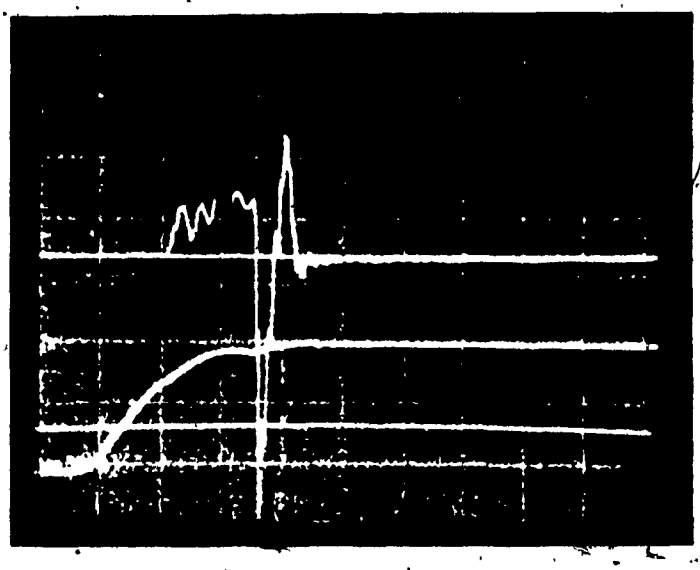

Upper Trace : Torque Transducer Output
(Scale: 14.7 lbf.in/div.)

Lower Trace : Pressure in the Rotary Junction Volume
(Scale: 50 $\frac{\text{lbf}}{\text{in}^2}$/div.)

Horizontal Axis: Time (Scale: 20 msec/div.)

Fig. H.3c: Oscilloscope Photographs of the Experimental Torque-Time and Pressure-Time Traces (Contn'd).

Friction Brake Torque = 15.20 lbf.in (Static)
= 12.00 lbf.in (Dynamic)

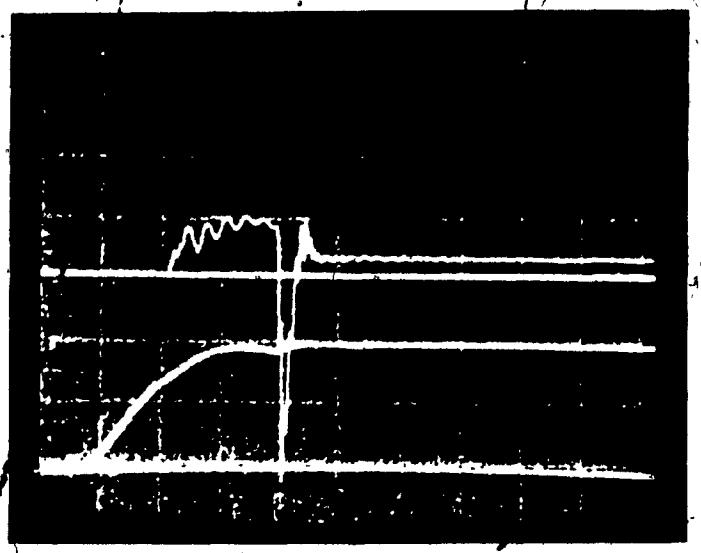

Upper Trace : Torque Transducer Output
(Scale: 14.7 lbf.in/div.)

Lower Trace : Pressure in the Rotary Junction Volume
(Scale: 50 $\frac{lbf}{in^2}$/div.)

Horizontal Axis: Time (Scale: 20 msec/div.)

Fig. H.3d: Oscilloscope Photographs of the Experimental Torque-Time and Pressure-Time Traces (Contn'd).

APPENDIX I

EXAMPLES OF APPLICATIONS OF THE STEPPING MOTOR

The operational features of the new pneumatic stepping motor make it useful in many applications. A description of two typical applications which have already been implemented follows.

a) A Low Cost Pneumatic Programmable Sequential Control Unit [20]

Figure I.1a shows a stepping motor of the configuration [A] driving a programmable disc. The above combination was incorporated in a control unit (Fig. I.1b), which sequentially operated a series of pneumatic cylinder for demonstration purposes. The disc is divided into 18 equal sectors each having 10 radially arranged program points. Eight of these program points are used for output while the other two are used for internal control of the unit. The program points consist of holes in the disc that can be either plugged by rubber balls to indicate a logical "0", or left unplugged to indicate a logical "1". The reading heads consist of 10 interruptible air jet nozzle-receiver type sensors. The disc is driven by the stepping motor which sequentially aligns the disc sections with the reading heads. The load on the motor in this application is almost entirely inertial.

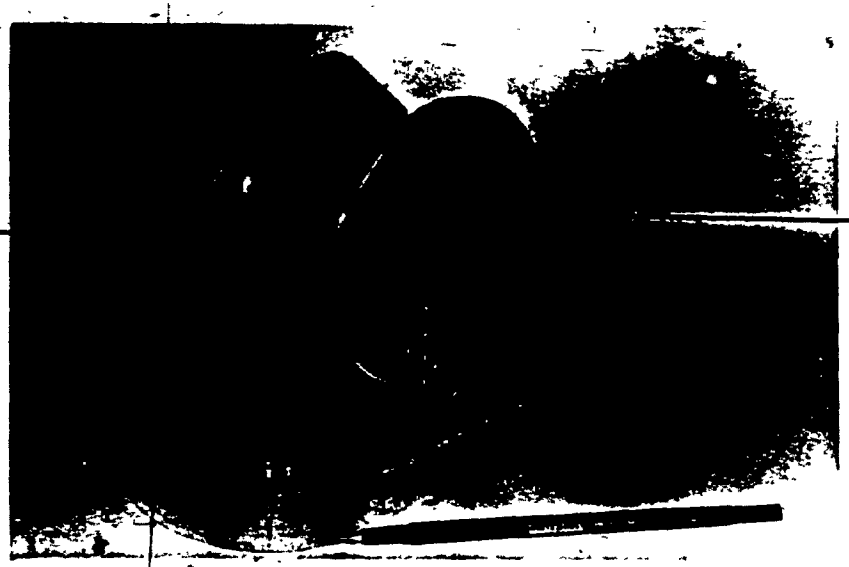

Fig. I.1a: Stepping Motor Driving a Programmable Disc.

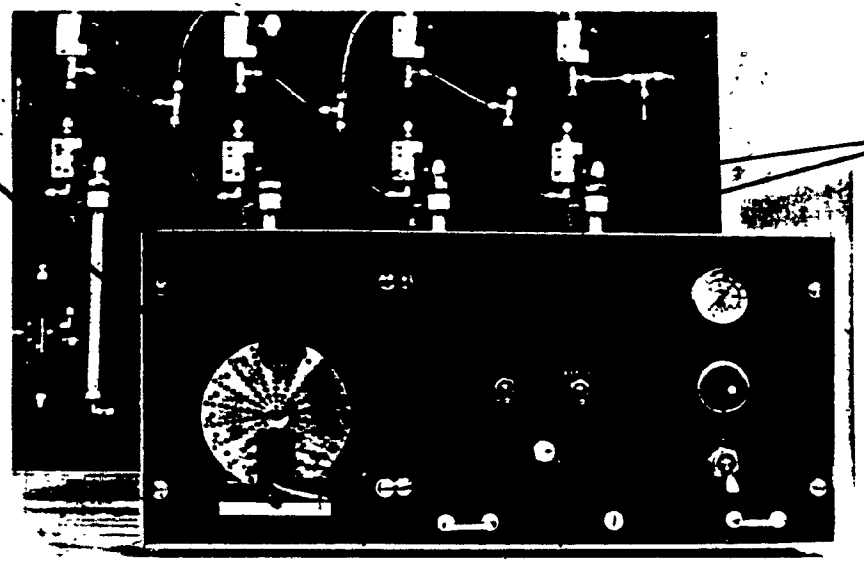

Fig. I.1b: Programmable Sequential Control Unit
Driving Four Cylinders.

b) Precision Liquid Metering System

A photograph of the metering system is shown in Fig. I.2. The system is composed of a motor of the configuration [D] driving a peristatic pump as shown in the figure. Each angle of rotation covered by the pump squeezes out a precise amount of liquid. Thus, a specific amount of liquid can be translated into a corresponding number of steps to be performed by the motor. Similarly, a required rate of output of the liquid can be translated into a corresponding rate of steps of the motor. A digital control unit (e.g. simple controller, or digital computer) can be employed to supply the required signals. The load in this application is a combination of both inertial and resistive.

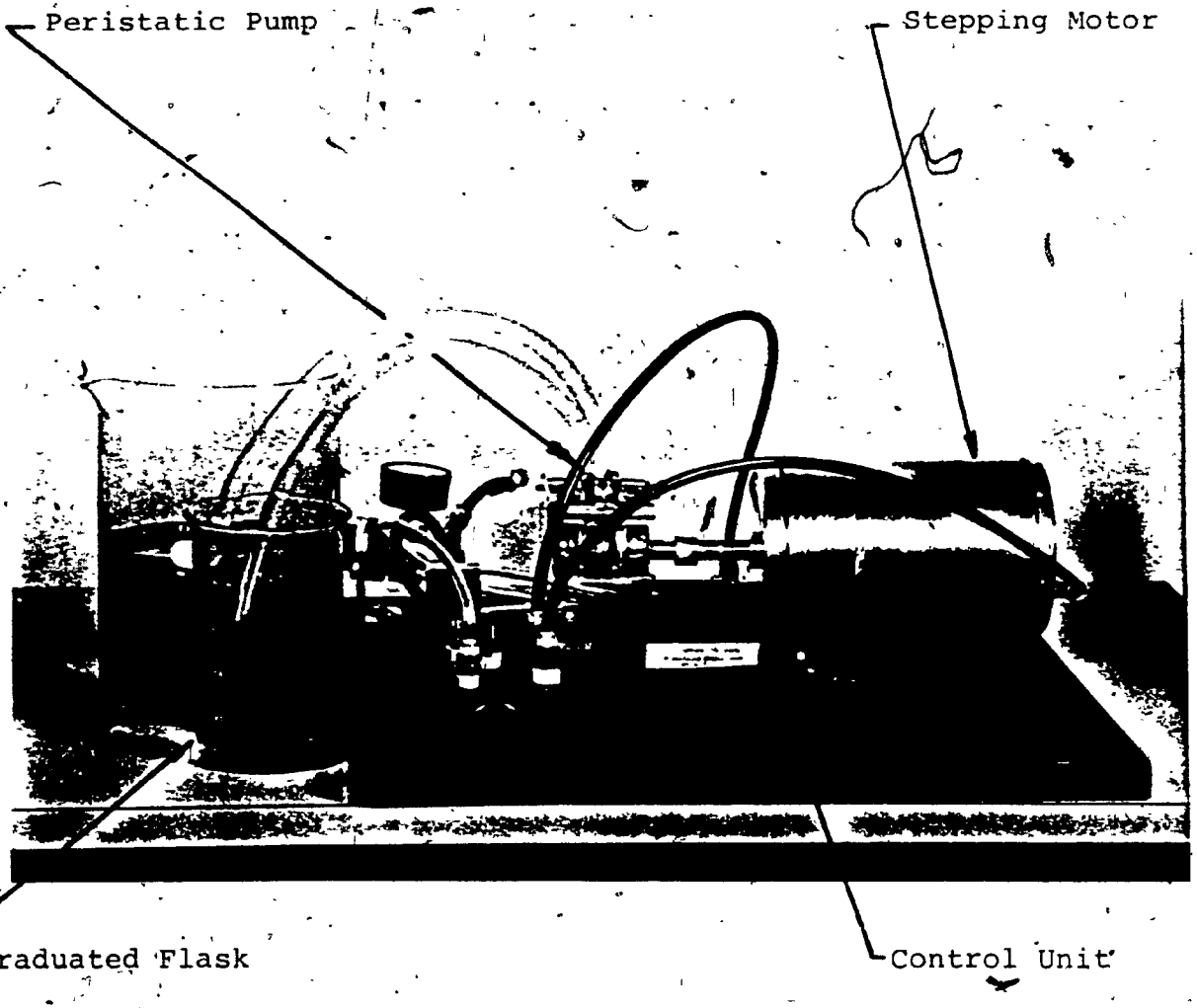

Fig. I.2: Metering Application Utilizing the Stepping Motor.